A study of radiative lepton decays of the Z boson

Andrew Betteridge

Royal Holloway, University of London

This thesis is submitted in part fulfillment
of the requirements for the degree of Ph.D
from the University of London.

April 24, 1996

Abstract

This thesis is devoted to the analysis of the data collected by the ALEPH detector at the large electron-positron (LEP) particle accelerator at CERN which studies the production and decay of the Z boson. The data was collected between 1990 and 1993 and corresponds to the production of about 1,422,000 Z events. Such a large data sample enables a detailed study of $Z \to l^+l^- + n\gamma$ ($n \geq 1$) events to be undertaken, where the aim is to observe physics beyond the standard model which enhances the number of events with an $l^+l^- + n\gamma$ final states, e.g. compositeness.

The thesis focuses on $Z \to \mu^+\mu^- + m\gamma$ ($m = 1$ or 2) and $Z \to \tau^+\tau^-\gamma$ decays. The analysis of the former decay involves comparing the data with a number of electroweak theoretical predictions. Any discrepancies would indicate the presence of physics beyond the standard model. The latter decay is used to obtain a limit for the anomalous magnetic moment of the tau.

The analysis of $Z \to \mu^+\mu^- + m\gamma$ events indicates that the Monte Carlo has some inadequacies; it overpredicts the number of events with either low energy photons or photons close to the muons. The data has a small excess in the region of phase space in which physics beyond the standard model is most likely to be observed. This excess is, however, more likely due to the deficiencies of the Monte Carlo. The other theoretical predictions are generally in good agreement with the data and show the necessity of including initial state radiation and s channel photon exchange when considering final states with a detected photon.

The standard model prediction for the value of the anomalous magnetic moment of the tau, denoted by $F_2^\tau(0)$, is $11\,773(3) \times 10^{-7}$. The current experimental limit of $F_2^\tau(0) < 0.0062$ does not rule out the possibility that the tau is composite. The analysis of $Z \to \tau^+\tau^-\gamma$ events produces the limit $F_2^\tau(0) < 0.051$. Whilst this result is worse than the current limit it is based on simpler theoretical assumptions.

Contents

List of Figures

List of Tables

Acknowledgements

The following people who enabled me to finally finish this thesis all deserve many thanks.

I would like to thank Mike Green for being my supervisor, always rooting out the problems of my analyses and for the proof-reading of this thesis.

I would also like all of the members of the Royal Holloway HEP group, especially Terry and Grahame who, no matter how busy they are, always provide help and advice if asked.

I also owe Steve Todd many thanks for teaching me all of the theory, and a lot of the Buddhism, that I have learnt in the last four years. I must also thank my family for putting up with me over the past four years.

Finally, I would like to thank the PPARC (and formally the SERC) for funding, and all those at CERN, especially in the ALEPH collaboration, who made the work possible.

Preface

The study of Particle Physics involves very large and expensive detectors which require many people to build and operate. Hence the work done in building the ALEPH detector, writing the event reconstruction and detector simulation software and accumulating the data has been the joint work of all members of the ALEPH collaboration. For completeness some of that work is described as background information and the first two chapters of this thesis are in that category. The rest of the work described in this thesis is my own.

Chapter 1

The standard model and the phenomenological effects of radiative corrections

1.1 Introduction

At the end of the last century it was thought that all physical phenomena could be explained using the principles of deterministic mechanics, but the theories of quantum physics and special relativity postulated phenomena that the classical theories did not. The predictions of the new theories were confirmed by experiment, and classical ideas were found to be invalid when dealing with subatomic phenomena or processes which involve velocities approaching the speed of light. Classical equations, however, could still be obtained as approximations of the new theories.

The birth of modern particle physics theory occured when the ideas of quantum mechanics and relativity were combined, and the initial ideas have been developed to produce the minimal standard model of particle physics [1], a self consistent theory which accommodates all experimental results [2]. The model is based on a locally gauge invariant quantum field theory and, at its most basic level, provides a list of physical fields and describes the non-linear interactions that occur between these fields. The phenomenological effects of the interactions between the fields can be calculated, and within the framework of the model all known subatomic processes can be explained if gravitational effects are excluded.

Whilst predictions of the standard model are in good agreement with experimental results there are many philosophical questions which it does not answer (such as why three generations, why is the top mass so large, etc.), and as the theory contains twenty one free parameters which must be experimentally determined, there is some dissatisfaction with the notion that it is the final layer of knowledge about the universe. Therefore it is hoped that some experimental evidence can be found which invalidates the model, and the LHC (Large Hadron Collider) should provide such evidence by illuminating the mechanism by which fields obtain mass. Such a mechanism must be discovered or else unitarity will be violated [3].

In this thesis comparisons are made between data collected by the ALEPH experiment and theoretical predictions made within the framework of the standard model, with the aim of finding indications of new physics beyond the standard model. To achieve this the phenomenological effects induced by radiative corrections are studied as these are similar to the effects of some of the theories that contain physics beyond the standard model. Therefore an explanation of the relevant sections of the standard model and the effect of radiative corrections are given in this chapter.

1.2 The standard model

The fields in the standard model can be classified into three classes - fermionic, vector and scalar. The spin 1/2 fermion fields are used to construct all of the physically observable matter in the universe, whilst the vector fields are introduced into the model when the lagrangian for the free fermionic fields is required to be invariant under local $SU(3)_C \otimes SU(2)_L \otimes U(1)_Y$ transformations. These bosonic fields transmit forces between the fermionic fields. The scalar field is a by-product of the mechanism by which particles acquire a gauge invariant mass term in the lagrangian, a process known as spontaneous symmetry breaking.

The matter in the universe is subjected to four forces - strong, weak, electromagnetic and gravitational. Only the first three are incorporated in the standard model; the latter is not present because a physical quantum theory of gravity has not yet been achieved within the confines of field theory.

In quantum field theory the effect of a force between two matter fields is realised by the exchange of a quantum of a vector, or gauge, field. Each force has an associated gauge field, or fields, and therefore an associated gauge group. Thus a matter field can be subjected to a force only if it couples to the associated gauge field, i.e. if the matter field has a non-zero value of the gauge charge. Table 1.1 makes the link between the three forces and the three gauge groups of the standard model, and lists the parameters of the groups that are required by the theory.

The twelve fermion fields present in the standard model are displayed in table 1.2. These fields have corresponding anti-fields with the same masses and allowed spin states but opposite internal quantum numbers. The fermion fields are subdivided into quarks and leptons: the former coupling to the strong gauge field whilst the latter do not. The quarks and leptons are grouped into three generations of four fields, the only physically observable difference between the generations being the masses attributed to the fields. Each generation consists of an up type quark and a down type quark along with a charged and neutral lepton, the leptons having the same flavour. All the fermions can be in either a left or right handed helicity eigenstate except for the neutral leptons, or neutrinos, which are assumed to be only left handed (only right handed anti-neutrinos). For the neutrinos to have only one helicity eigenstate it is required that they are massless.

An important, and unique, feature of the strong force is that, for separations greater than 10^{-15} m, its strength is linearly proportional to the distance between two coloured objects. Therefore it is energetically favourable for quarks to cluster

Force	Gauge group	Gauge bosons	Gauge charge	Coupling constant
Strong	SU(3)	Gluons	Colour	g_s
Weak	SU(2)	$W^{\pm}, Z^0$	Isospin	$g'/2$
Electromagnetic	U(1)	γ	Electric	g

Table 1.1: The properties of the forces in the standard model.

	QUARKS		LEPTONS	
Generation	Flavour	Electric charge	Flavour	Electric charge
1	u	+2/3	ν_e	0
	d	-1/3	e	-1
2	c	+2/3	ν_μ	0
	s	-1/3	μ	-1
3	t	+2/3	ν_τ	0
	b	-1/3	τ	-1

Table 1.2: The physical properties of the fermionic matter.

	Spin	Colour	Electric charge
Higgs scalar	0	colourless	0

Table 1.3: The physical properties of the Higgs boson.

together to form singlets of $SU(3)_C$ as these are not attracted to other coloured objects. Thus free quarks are never observed. These clusters of quarks are known as hadronic matter and can be either baryons (three quarks) or mesons (a quark and an anti-quark).

The only scalar field predicted by the theory is shown in table 1.3. It is a remnant of the process that is used to provide mass terms for both the gauge bosons and the fermions. It has not yet been experimentally observed and its mass range is 63.1 GeV/c^2 [4] $< M_{Higgs} < \mathcal{O}(1$ TeV/c$^2)$. The upper limit comes from theoretical self-consistency arguments.

There are four accidental $U(1)$ symmetries present in the standard model which introduce an extra four conserved quantum numbers. These are an electron number, a muon number, a tau number and a baryon number. Quanta of lepton fields have a value of +1 for the appropriate flavour quantum number, whilst those of the anti-lepton fields have the value -1.

Non-zero baryon numbers are present only in the quark fields and the values assigned are flavour independent. The quanta of all quark fields have baryon number +1/3 and those of anti-quark fields have the value -1/3. Therefore baryons and anti-baryons have the values +1 and -1 respectively for their baryon quantum number.

Since these symmetries are produced by $U(1)$ groups, the four quantum numbers must be conserved globally. Thus if a quantum of a lepton, or quark, field is created then a quantum of the appropriate flavour anti-lepton field, or any flavour anti-quark field, must also occur. Mesons are not conserved as their baryon number is zero.

1.2.1 Electroweak unification

The idea of unifying the electromagnetic and weak forces into a single framework was proposed by Weinberg, Salam and Glashow [5] [6] [7], and has since been confirmed by experiment. This section will explain the stages of this process which are relevant to this thesis, and show how a model is formed with physical particles and phenomenological predictions which agree with experiment [8].

The first of the four known forces to be explained by a gauge invariant quantum field theory was electromagnetism. The resulting theory is known as quantum electrodynamics, or QED, and is based on a $U(1)$ symmetry. There is one gauge boson, the photon, as the adjoint representation of $U(1)$ only has one element. The group charge is identified to be electric charge, and thus the strength of the coupling between the gauge field and a fermionic field is dependent on the electric charge carried by the latter. QED, after applying Noethers theorem, also predicts the conservation of electric charge. QED successfully predicts all known electromagnetic phenomena and its higher order predictions have been rigorously tested experimentally and no discrepancies have been found [9].

Experimental studies of the weak force suggest that it has an underlying $SU(2)$ symmetry. A major factor which points to this idea is that the three experimentally identified weak bosons, two electrically charged and one neutral, are equivalent to those predicted by the adjoint representation of $SU(2)$. This symmetry, however, must be broken as experiments have determined that the weak bosons are massive, and the inclusion of mass terms for the gauge bosons in the lagrangian breaks the $SU(2)$ symmetry.

The underlying $SU(2)$ of the weak force maximally violates parity as experimental observations have shown that, in their rest frame, the charged weak gauge bosons couple only to left handed particles. This is in contrast with QED where the photon couples equally to left and right handed particles. A problem arises, however, with the experimental observation that the weak neutral boson couples to both left and right handed particles, albeit unequally. A solution to this problem exists if the electromagnetic and weak forces can be combined, as then the neutral weak boson can obtain a non-zero coupling to right handed particles through mixing with the electromagnetic gauge boson.

To combine the electromagnetic and weak forces it is initially necessary to assume the masses of all the field quanta, both fermionic and bosonic, are zero and consider a quantum field theory which is invariant under $SU(2)_L \otimes U(1)_Y$

transformations. It is shown below how such a theory produces the experimentally observed $U(1)_{QED}$ and massive weak bosons.

In this theory the massless fermionic fields are arranged into left handed $SU(2)_L$ doublets and right handed $SU(2)_L$ singlets. The doublets have total weak isospin, I, of +1/2, with the third component of weak isospin, I_3, being +1/2 and -1/2 for the upper and lower components of the doublets respectively. The right handed singlets have both I and I_3 equal to zero. The left handed doublets for each generation of fermions have the following generic structure

$$\begin{pmatrix} \text{up type quark} \\ \text{down type quark} \end{pmatrix}_L \qquad \begin{pmatrix} \text{neutral lepton} \\ \text{charged lepton} \end{pmatrix}_L .$$

All the fermionic field quanta, except those of the neutral lepton fields, exist as right handed singlets.

The weak hypercharge, Y, assigned to the field quanta is given by

$$Y = 2(Q - I_3)$$

where Q is the electric charge, in units of e, of the experimentally observed fermions. The values of I, I_3, Y and Q for all the fermionic fields is shown in table 1.4.

Field quantum	I	I_3	Y	Q
ν_{eL}, $\nu_{\mu L}$, $\nu_{\tau L}$	1/2	1/2	-1	0
e_L, μ_L, τ_L	1/2	-1/2	-1	-1
e_R, μ_R, τ_R	0	0	-2	-1
u_L, c_L, t_L	1/2	1/2	1/3	+2/3
u_R, c_R, t_R	0	0	4/3	+2/3
d_L, s_L, b_L	1/2	-1/2	1/3	-1/3
d_R, s_R, b_R	0	0	-2/3	-1/3

Table 1.4: The $SU(2)_L \otimes U(1)_Y$ charges of the fermionic fields.

The three $SU(2)_L$ gauge bosons, W^i_μ $i = 1, 2, 3$, couple to the fermion fields through weak isospin with coupling constant g, whilst the $U(1)_Y$ gauge boson,

B_μ, couples to the fermion fields through their weak hypercharge with coupling constant $g'/2$. The section of the $SU(2)_L \otimes U(1)_Y$ lagrangian which contains the interactions between gauge bosons and fermions is

$$\mathcal{L}_I = \sum_i \overline{\chi}^i_L \gamma^\mu \left(-g\frac{1}{2}\vec{\tau} \cdot \vec{W}_\mu - g'\frac{Y}{2}B_\mu \right) \chi^i_L - \sum_j \overline{\phi}^j_R \gamma^\mu g' \frac{Y}{2} B_\mu \phi^j_R$$

where χ_L and ϕ_R are a left handed $SU(2)_L$ doublet and a right handed $SU(2)_L$ singlet of the fermionic fields respectively, and τ_i, $i = 1, 2, 3$, are the Pauli spin matrices.

Table 1.4 shows that left and right handed particles have different values of Y, although the same values of Q. This means that the $U(1)_Y$ gauge boson does not have chirally symmetric couplings, and thus $U(1)_Y$ is different from the gauge group of electromagnetism. How the $U(1)_{QED}$ symmetry is obtained will be explained.

It is possible to split $\mathcal{L}_I$ into a charged current contribution, $\mathcal{L}_{CC}$, where the incoming and outgoing fermions differ by one unit of electric charge, and a neutral current contribution, $\mathcal{L}_{NC}$, where the incoming and outgoing fermions have the same electric charge.

For the charged current it is convenient to construct two electrically charged weak gauge bosons from W^1_μ and W^2_μ which are defined as

$$W^\pm_\mu = W^1_\mu \pm iW^2_\mu.$$

The new gauge bosons raise or lower by one unit the third component of weak isospin of one of the elements of an $SU(2)_L$ doublet, and so they couple the $I_3 = +1/2$ element of an $SU(2)_L$ doublet to the $I_3 = -1/2$ element. The form of the charged current lagrangian is

$$\mathcal{L}_{CC} = -\frac{g}{2\sqrt{2}} \sum_i \left\{ \overline{\chi}^i_L \gamma^\mu \tau_+ \chi^i_L W^+_\mu + \overline{\chi}^i_L \gamma^\mu \tau_- \chi^i_L W^-_\mu \right\}$$

with

$$\tau_\pm = \tau_1 \pm i\tau_2$$

Thus the theory has predicted particles with the same interactions as the experimentally observed charged weak bosons, although the theoretical particles are still massless.

It is known from experiment that there is a neutral current which couples equally to left and right handed particles. Neither the W_μ^3 or B_μ have chirally symmetric couplings and it is therefore necessary to mix these two fields to obtain two new fields, A_μ and Z_μ, the first of which will be the QED gauge field. A free parameter, θ_W, is introduced to quantify the mixing between the W_μ^3 and B_μ fields, and the new fields are defined by requiring that

$$
\begin{aligned}
W_\mu^3 &= \cos\theta_W Z_\mu + \sin\theta_W A_\mu \\
B_\mu &= -\sin\theta_W Z_\mu + \cos\theta_W A_\mu .
\end{aligned}
\tag{1.1}
$$

Thus the neutral current lagrangian has the form

$$
\begin{aligned}
\mathcal{L}_{NC} &= \left[\sum_i \overline{\chi}_L^i \gamma^\mu \left(-g\sin\theta_W \frac{\tau_3}{2} - g'\cos\theta_W \frac{Y}{2}\right)\chi_L^i - \sum_j \overline{\phi}_R^j \gamma^\mu g' \cos\theta_W \frac{Y}{2}\phi_R^j\right] A_\mu \\
&+ \left[\sum_i \overline{\chi}_L^i \gamma^\mu \left(-g\cos\theta_W \frac{\tau_3}{2} + g'\sin\theta_W \frac{Y}{2}\right)\chi_L^i + \sum_j \overline{\phi}_R^j \gamma^\mu g' \sin\theta_W \frac{Y}{2}\phi_R^j\right] Z_\mu
\end{aligned}
$$

where electric charge is given by $e = g\sin\theta_W = g'\cos\theta_W$.

The introduction of θ_W has not increased the total degrees of freedom of the theory as equation 1.1 provides a link between the coupling constants of the two gauge groups, i.e. $g' = g\tan\theta_W$. It is because this link between the gauge couplings is established that the combining of the electromagnetic and weak forces is known as electroweak unification, even though the weak and electromagnetic theories are not embedded in a larger gauge group.

The non-abelian nature of the product group $SU(2)_L \otimes U(1)_Y$ means that the kinetic terms of the gauge bosons present in the electroweak lagrangian contain expressions that allow the four derived gauge bosons, that is the $W_\mu^\pm$, Z_μ and A_μ, to couple amongst themselves.

The $SU(2)_L \otimes U(1)_Y$ theory constructed above has many facets in common with experimental knowledge of the electroweak sector - the same number of matter fields with the correct quantum numbers, two electrically charged weak bosons and two neutral bosons, where one of the latter has equal left and right handed couplings allowing the $U(1)_{QED}$ symmetry to be introduced. However, any mass terms for either the gauge bosons or the fermions breaks the gauge invariance. Thus the Higgs mechanism is introduced to spontaneously break the gauge symmetry and allow the theory to contain massive particles.

The Higgs mechanism introduces a scalar field into the $SU(2)_L \otimes U(1)_Y$ lagrangian which has non-trivial gauge transformation properties. A scalar is used so that Lorentz invariance is not violated. The term introduced into the lagrangian is

$$\mathcal{L}_{Higgs} = \left|\left(\partial_\mu + ig\frac{1}{2}\vec{\tau}\cdot\vec{W}_\mu + ig'\frac{Y}{2}B_\mu\right)\phi\right|^2 \tag{1.2}$$

$$-\mu^2\left(\phi^\dagger\phi\right) - \lambda\left(\phi^\dagger\phi\right)^2 \tag{1.3}$$

where 1.2 is the gauge invariant kinetic term of the scalar field and 1.3 is the potential term. Higher order $\phi^\dagger\phi$ terms are not included as their dimensionality would make the lagrangian unrenormalisable. The field ϕ is a complex scalar doublet of $SU(2)_L$ and has the form

$$\phi = \begin{pmatrix} \phi_\alpha \\ \phi_\beta \end{pmatrix} = \frac{1}{\sqrt{2}}\begin{pmatrix} \phi_1 + i\phi_2 \\ \phi_3 + i\phi_4 \end{pmatrix}$$

where the ϕ_i, $i = 1,2,3,4$, all have $Y = 1$, which leads to one component of the doublet being electrically neutral. Thus the $U(1)_{QED}$ can be preserved after spontaneous symmetry breaking.

The potential part of $\mathcal{L}_{Higgs}$ gives the vacuum a structure which has a local minimum when

$$\phi^\dagger\phi \equiv \frac{1}{2}\left(\phi_1^2 + \phi_2^2 + \phi_3^2 + \phi_4^2\right) = -\frac{\mu^2}{2\lambda}.$$

It is required that $\phi^\dagger\phi$ is positive, and therefore either $\mu^2 > 0$ and $\lambda < 0$ or $\mu^2 < 0$ and $\lambda > 0$. The former describes the case where four scalar particles interact with massless gauge bosons, and is therefore irrelevant. The latter case, however, produces the required spontaneous breaking of the $SU(2)_L \otimes U(1)_Y$ symmetry and leads to a local minimum that has only one degree of freedom, and thus three components of ϕ become Goldstone bosons.

By choosing the unitary gauge, where unphysical particles do not appear, ϕ is transformed to ϕ_0, with

$$\phi_0 = \begin{pmatrix} 0 \\ v + H \end{pmatrix}$$

where v $(= -\mu^2/\lambda)$ is the vacuum expectation value, and H is the observable scalar field that is a relic of the Higgs process, and is interpreted as quantum fluctuations perpendicular to the rotational degree of freedom of the vacuum. The three Goldstone bosons provide the $W_\mu^\pm$ and Z_μ fields with longitudinal polarisation vectors. It is these polarisation states which enable the gauge fields to have a non-zero mass. The observable Higgs field is electrically neutral and therefore does not couple to the photon, thus the QED gauge boson is a mass eigenstate with eigenvalue zero, as required. Therefore the $SU(2)_L$ and $U(1)_Y$ symmetries have been spontaneously broken (this is where the lagrangian remains gauge invariant but the vacuum does not), whilst the derived $U(1)_{QED}$ symmetry remains.

The masses for the gauge bosons following spontaneous symmetry breaking are

$$\begin{aligned} M_W &= \frac{vg}{2} \\ M_Z &= \frac{1}{2} v \sqrt{g^2 + g'^2} \\ M_\gamma &= 0 \end{aligned}$$

and the mass of the physical Higgs scalar is

$$M_H^2 = 2v^2\lambda.$$

Thus for the gauge bosons to become massive two additional degrees of freedom have been introduced - the vacuum expectation value and the mass of the physical Higgs field.

Finally, mass terms for the fermions are obtained by introducing gauge invariant Yukawa-type couplings between the fermionic fields and the Higgs field. For the leptons the term

$$-\sum_{i=e,\mu,\tau}\frac{G_i}{\sqrt{2}}\left(\overline{\chi}_L^i\phi_0\phi_R^i+\overline{\phi}_R^i\phi_0\chi_L^i\right) \tag{1.4}$$

provides the electron, muon and tau with masses $G_i v/\sqrt{2}$, $i=e,\mu,\tau$, where the G_i are free parameters. The neutrinos are assumed to be massless and are not given such Yukawa-type couplings.

In the quark sector the down type quarks acquire masses using a term identical to 1.4, but the sum is over $j=u,c,t$. Thus three further degrees of freedom, the G_j, have to be introduced. The up type quarks obtain mass terms by coupling to the conjugate Higgs field, ϕ_C, where

$$\phi_C = i\tau_2\phi.$$

In the unitary gauge

$$\phi_{C0}=\frac{1}{\sqrt{2}}\begin{pmatrix} v+H \\ 0 \end{pmatrix}$$

and the expression providing mass terms for the up type fields is

$$-\sum_{j=b,s,d}\frac{G_j}{\sqrt{2}}\left(\overline{\chi}_L^j\phi_{C0}\phi_R^j+\overline{\phi}_R^j\phi_{C0}\chi_L^j\right).$$

A problem arises in the quark sector because the mass eigenstates are not equal to the weak eigenstates. This is solved by introducing mixing between the three generations of down type quarks through the CKM matrix [10].

Therefore, by starting off with a field theory invariant under $SU(2)_L\otimes U(1)_Y$ transformations it is possible to obtain a model of electroweak interactions which provides predictions that are in good agreement with experimental observations. The final electroweak lagrangian, after spontaneous symmetry breaking, is

$$\mathcal{L} = -\frac{1}{4}\vec{W}_{\mu\nu}\cdot\vec{W}^{\mu\nu}-\frac{1}{4}B_{\mu\nu}B^{\mu\nu} \tag{1.5}$$

$$+\sum_i\overline{\chi}_L^i\gamma^\mu\left(i\partial_\mu-g\frac{1}{2}\vec{\tau}\cdot\vec{W}_\mu-g'\frac{Y}{2}B_\mu\right)\chi_L^i$$
$$+\sum_j\overline{\phi}_R^j\gamma^\mu\left(i\partial_\mu-g'\frac{Y}{2}B_\mu\right)\phi_R^j \tag{1.6}$$

$$+\left|\left(i\partial_\mu - g\frac{1}{2}\vec{\tau}\cdot\vec{W}_\mu - g'\frac{Y}{2}B_\mu\right)\phi\right|^2 - \mu^2\left(\phi^\dagger\phi\right) - \lambda\left(\phi^\dagger\phi\right)^2 \tag{1.7}$$

$$\begin{aligned}&-\sum_i G_i\left(\overline{\chi}_L^i\phi\phi_R^i + \overline{\phi}_R^i\phi\chi_L^i\right)\\ &-\sum_j G_j\left(\overline{\chi}_L^j\phi_C\phi_R^j + \overline{\phi}_R^j\phi_C\chi_L^j\right)\end{aligned} \tag{1.8}$$

where

- 1.5 contains the kinetic energies and self interactions of the electroweak gauge bosons;
- 1.6 contains the fermionic kinetic energies and their interactions with the electroweak gauge bosons;
- 1.7 provides the terms which allow the gauge bosons and the physical Higgs scalar to be massive, and also describes the interactions between the gauge bosons and the physical Higgs boson;
- 1.8 provides the terms which define the masses of the fermions and details how the fermions couple to the physical Higgs boson.

1.2.2 Quantum chromodynamics

In the standard model the quarks are the only matter fields which couple to the mediators of the strong force. It is the effect of this force which produces the clusters of quarks that are detected by experiment; a free particle with a fractional charge has never been experimentally observed, implying that free quarks are not found in nature. The residual effects of this force hold the constituents of nuclei together, and this was the first phenomenological effect of the strong force to be experimentally observed. The true nature of the strong force was discovered when deep inelastic scattering experiments implied that nucleons had substructure, and thus the quark was discovered [11].

Following this discovery, it was shown that there exists a class of gauge invariant quantum field theories that are both renormalisable and which produce a mechanism to explain quark confinement, i.e. a force that is small in magnitude for distances less than 10^{-15}m but whose strength increases dramatically as this limit is exceeded. This is known as asymptotic freedom. The member of this class of field theories with properties that match experimental observations has the gauge group $SU(3)$.

The charge of the strong gauge group $SU(3)_C$ is colour, and can take one of three values - red, green or blue. Thus one of these three charges is assigned to each quark, whilst the anti-quarks are either anti-red, anti-green or anti-blue. Therefore, for calculations involving effects of the strong force the quarks are placed in triplet representations of $SU(3)_C$.

The nature of the strong gauge bosons, or gluons, is determined by the algebra of the adjoint representation of $SU(3)_C$, which has eight elements. Due to the non-abelian nature of the gauge group, the gauge bosons are coloured and therefore self-couple. It is this facet of the theory which gives rise to asymptotic freedom.

If a quark, or cluster of quarks, is not a colour singlet of $SU(3)_C$ then more quarks will be attracted until a cluster is produced which is a colour singlet. The two $SU(3)_C$ representations of quarks which produce the colour singlets that are physically observed are either clusters of three quarks (or three anti-quarks) or a quark coupled to an anti-quark. The former are known as baryons, the latter as mesons, and together are collectively refered to as hadrons. The large spectrum of observed hadrons arises because they are composite objects, and therefore two hadrons with the same constituent quarks can have different masses. This is because the constituent quarks of the hadron with the larger mass occupy excited energy states with larger energy eigenvalues than those inhabited by the quarks of the less massive hadron.

1.3 Beyond the standard model

Despite good agreement between the predictions of the standard model and experimental results, the standard model is not thought to be the final explanation of how forces interact with matter, but rather a low energy approximation of either a grand unified theory or a theory of everything. This is because the standard model is based on a gauge field theory, and such theories never predict the values of the couplings between the fields and the masses of the fields, although they can occasionally predict ratios between some of these values, e.g. the grand unified theory based on $SU(5)$ predicts the value of $\sin^2\theta_W$ [1]. This leads to the standard model having 21 free parameters which must be determined experimentally. Another problem with the standard model is that some of the procedures used in its formulation are employed simply because they provide the correct answer, e.g. the Higgs mechanism.

If there is physics beyond the standard model then some experimental observations may not exactly match the predictions of the standard model. For example, the theory of compositeness [12] enhances certain regions of the standard model prediction for the photon energy spectrum obtained by considering the process of a lepton radiating a photon. Thus, if compositeness is a valid theory, the energy spectrum of photons radiated from leptons obtained by experiment will be different from that predicted by the standard model.

As compositeness produces phenomenological effects which are similar to those being studied in this thesis, a brief outline of the relevant ideas of compositeness follows.

In compositeness some (or maybe all, depending on the model) of the fermionic and bosonic fields of the standard model are constructed from preonic fields. It is possible for a composite object to have a series of energy levels which means that it can have a variety of mass eigenstates. The standard model fields are taken to be the lowest energy configuration of preons, and excited states are obtained through the absorbtion of a photon. Therefore an excited state returns to the ground state through the emission of a photon. Thus if, for example, a lepton is composite it will radiate more photons than it would if it were not composite. The photons emitted by a preon tend to have higher energies and a greater angular separation from the fermion than is the case for photons radiated by the fermion through standard model processes.

1.4 Higher order effects

The previous section on the standard model explained how a lagrangian could be constructed which contains physical particles identical to those observed by experiment. In order to carry out experimental tests of this model it is necessary to construct the S matrix [13]. An element of this matrix, S_{ij}, is a measure of the probability that state i at time $t = -\infty$ will develop into state j at time $t = +\infty$. If conservation of probability is required then the S matrix must be unitary, i.e. $S^\dagger S = 1$. Thus if any of the elements of the S matrix are extremely large then unitarity, and hence the conservation of probability, are violated.

Calculation of an element of the S matrix in the framework of quantum field theory involves the use of functional integrals [14]. In the case of the standard model these integrals can not be solved exactly but an asymptotic answer can be obtained if the machinery of perturbation theory is employed, where the coupling constants between the fields are chosen to be the expansion parameters.

The results provided by the perturbation expansion are asymptotic rather than approximate because all S matrix elements contain effects which can not be calculated using perturbation theory. However, for virtually all of the matrix elements the non-perturbative effects are negligible and the perturbation expansion provides an accurate approximation of the functional integral. Though there are some cases, e.g. low energy QCD calculations, where perturbation theory breaks down and can not be used to produce a value for the result of the functional integral.

The method of calculating the functional integrals using perturbation theory is complex. Therefore it is usual to adopt the method of calculating S matrix elements which was introduced by Feynman. In this method a perturbation expansion is represented by a set of diagrams, and application of the Feynman rules converts these diagrams into a matrix element. This approach, where field quanta are replaced by point like particles, is adopted for the rest of this thesis.

The nature of perturbation theory means that an exact prediction of perturbative effects can only be obtained if the expansion is done to infinite order. In practice this is impossible, and thus all elements of the S matrix that are obtained using perturbation theory are approximations. It is therefore important that truncating the expansion does not significantly affect the result, i.e. that as the order of the term in the expansion increases its contribution to the sum over all orders decreases. For the standard model, however, this is not true, and higher order terms produce infinite contributions to the perturbation expansion. This situation is rectified by a process known as renormalisation. This process is briefly summarised in the next section.

The last two sections of this chapter are concerned with the effects associated with the introduction of higher order photonic corrections. The first of these sections includes an explanation of the phenomenological effects of corrections involving real photons, whilst the second shows how a sub-class of virtual photonic corrections gives the fermions an anomalous magnetic moment within the standard model.

1.4.1 Renormalisation

When calculating the matrix element S_{ij} for a given i and j there are a finite number of Feynman diagrams representing the lowest order of the perturbation expansion. These are known as the Born level diagrams. If higher order contributions are to be included in the calculation of S_{ij} then new Feynman diagrams must be added to the Born diagrams, but as i and j do not change then the additional particles in the new diagrams have to create internal closed loops. As an illustrative example consider a photon propagating between two points.

The Born diagram for a photon propagating between the points A and B is shown in fig. 1.1 (a). If the Feynman rules are employed to convert this diagram into the S matrix element where both the i and j states are a photon then the answer obtained does not violate unitarity. A possible higher order correction to the S matrix element is shown in fig. 1.1 (b). Here, whilst between A and B, the photon decays to an electron-positron pair which then recombine back into a photon. This is known as vacuum polarisation.

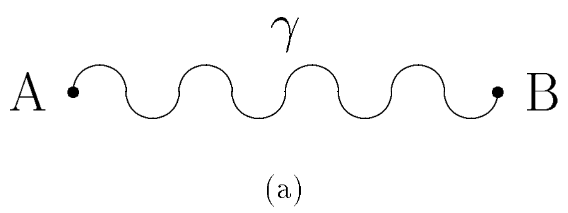

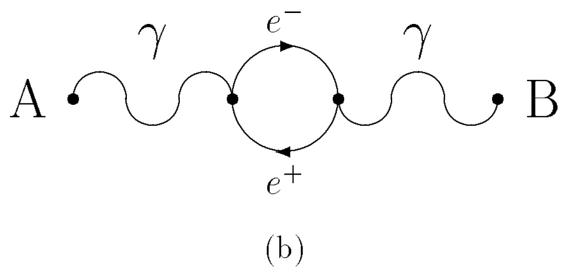

Figure 1.1: The Born term (a) and a vacuum polarisation term (b) which contribute to the S matrix element for a photon propagating between A and B.

Whilst the momenta of the external photons in fig. 1.1 (b) are fixed, the momenta of the particles in the internal loop can take any value up to, and including, infinity. This is possible as in Feynman diagrams conservation of momentum is only applied at the vertices. The contribution of this vacuum polarisation diagram to the S matrix element is proportional to an integral which tends to infinity as the upper limit of the momenta of the particles in the internal loop tends to infinity. Thus this correction makes an infinite contribution to the matrix element. This is an example of ultraviolet divergence, i.e. when the unconstrained upper limit of the momenta of particles in an internal loop results in an infinite S matrix element. Thus unitarity is violated and the model does not appear to be a physical theory.

The method used to remove such ultraviolet divergences is known as renormalisation. Following the application of this procedure, if the theory is renormalisable, all elements of the S matrix calculated using perturbation theory are finite and the S matrix is unitary.

The removal of an ultraviolet divergence involves a three stage process. In the first stage, dimensional regularisation is used to make the term containing the ultraviolet divergence finite. This is achieved by reducing the dimensionality of the manifold to $4 - \varepsilon$ ($|\varepsilon| \ll 1$). Following this, counterterms which cancel the ultraviolet divergence are added to the lagrangian. Finally, the manifold is restored to four dimensions by letting ε tend to zero. Thus the perturbation expansion involving the ultraviolet divergence now produces a finite S matrix element.

The above technique is valid only if the ultraviolet divergence is logarithmic. Theories where all ultraviolet divergencies are logarithmic are called renormalisable, or physical, theories. The standard model is such a theory and thus has a unitary S matrix.

The counterterms which are added to the lagrangian are used to define the renormalised charges and masses of the particles. The redefinition of these quantities is required because when comparing theory with data it is only the renormalised charges and masses which have any physical meaning. The original, or bare, charges and masses which appear in the lagrangian can take any value, including infinity, as they are not physically observable. This is because the charges and masses in the lagrangian have values equivalent to a Born level calculation, whilst the values of physical quantities are obtained from calculations involving an infinite perturbation expansion.

1.4.2 The phenomenology resulting from photonic corrections

There are three ways of adding photons to the external fermion lines of Born level Feynman diagrams. As an illustrative example consider the different ways that one photon can be added to the muon lines of the Born diagram for $Z \to \mu^+\mu^-$, shown in fig. 1.2 (a).

The two diagrams of fig. 1.2 (b) are created by adding a real photon to each of the muon lines of (a). The other two possibilities of adding a photon to the Born diagram involve virtual photons and produce a total of three diagrams. Allowing either of the muons to emit and reabsorb a photon produces two diagrams (fig. 1.2 (c)), and the last diagram arises when the photon is emitted by one muon and

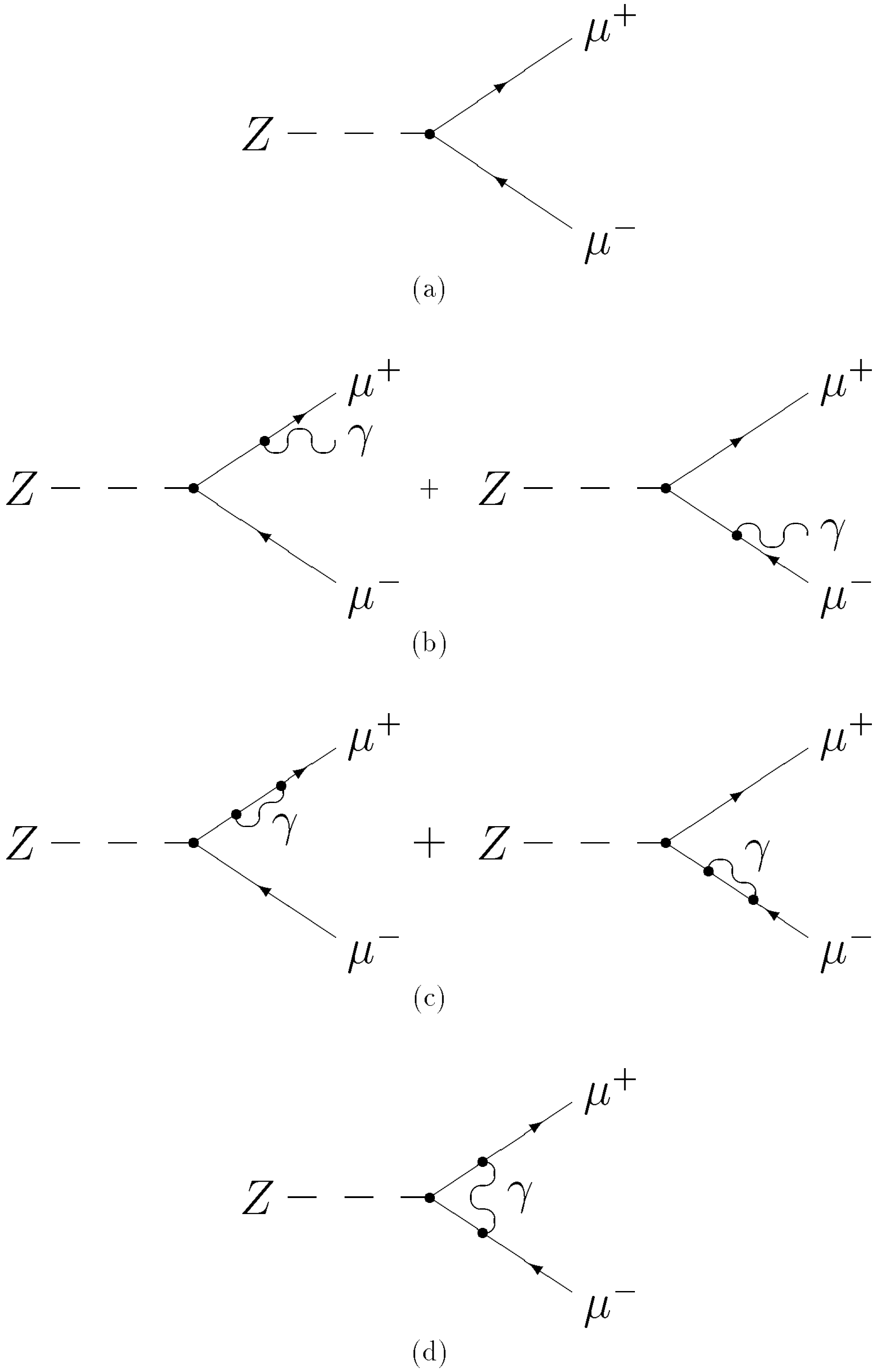

Figure 1.2: This figure shows (a) the Born diagram for $Z \to \mu^+\mu^-$ and in (b) (c) and (d) the diagrams resulting from adding a photon to a fermion line.

reabsorbed by the other (fig. 1.2 (d)).

This section will describe how these photonic corrections affect the S matrix element for $Z \to \mu^+\mu^-$, and also will outline the phenomenology of the new process $Z \to \mu^+\mu^-\gamma$ which is created by these corrections. Before these explanations, it is shown how the final state particles of the diagrams in fig 1.2 (b) can have two different topological configurations when they are detected by an experiment.

The calorimeters used to identify photons in particle physics experiments have a threshold energy for detecting an incident particle. This means that very low energy photons are not detected. Thus the decay $Z \to \mu^+\mu^-\gamma$ can be experimentally detected as either two muons, if the photon energy is lower than the detection threshold, or two muons and a photon. The total detected energy in the former case will still be approximately the centre of mass energy as the photon energy is small, and thus it will be interpreted as coming from a $Z \to \mu^+\mu^-$ decay. The splitting of the decay $Z \to \mu^+\mu^-\gamma$ into two different final state topologies by the process of experimental detection is required for cancellation of infrared divergences, as explained below.

One effect of the Feynman diagrams in figs. 1.2 (c) and (d) is to change the renormalised charge of the muon. This creates a problem because the magnitude of this change is dependent on the mass of the muon, and thus such corrections suggest that leptons have different renormalised charges. The Ward identities, however, show that the effect on the muon charge of the diagrams of fig. 1.2 (c) is equal and opposite to the effect of the diagram of fig. 1.2 (d). Thus the net change to the renormalised charge of the muon is zero. Therefore the physically observed electric charge of the leptons, and also that of the quarks, is unaffected by photonic corrections to the fermionic legs of Feynman diagrams. Thus the renormalisation of electric charge is entirely due to vacuum polarisation of the propagator, a process independent of the masses of the external fermions.

The virtual photon corrections of fig. 1.2 introduce negative infinities, called infrared divergences, into the perturbation expansion. The addition of counterterms to the lagrangian is not required in this instance as the corrections involving real photons give rise to positive infinities which cancel the negative infrared divergences. This appears to be a cancellation between different final state topologies but, as the divergences due to real photon corrections occur as the photon energy tends to zero, the cancellation occurs for photon energies lower than the experimental detection threshold. It was shown above that events with such low energy photons are experimentally designated to be $Z \to \mu^+\mu^-$ decays. Thus, from an experimental viewpoint, the cancellation is between decays with the same final state topologies.

The diagram of fig. 1.2 (d) also alters the structure of the $Z\mu^+\mu^-$ vertex. This effect is explained in the next section.

Consider the phenomenology produced by the diagrams of fig. 1.2 (b) when the photon energy is larger than the experimental detection threshold, which means that there is a $\mu^+\mu^-\gamma$ final state. Firstly consider the spectra of the photon energy and the angle between the photon and the radiating muon. The contribution to the S matrix element from both Feynman diagrams contains a factor which arises from the muon propagator which has the form

$$\frac{1}{(p_\mu + p_\gamma)^2 - M_\mu^2} = \frac{1}{2E_\gamma \left(E_\mu - \sqrt{E_\mu^2 - M_\mu^2} \cos\theta \right)} \tag{1.9}$$

where p_μ $(= (E_\mu, \vec{p}_\mu))$ and p_γ $(= (E_\gamma, \vec{p}_\gamma))$ are the four-momenta of the radiating muon and the photon respectively, and θ is the angle between these two particles. Equation 1.9 is inversely proportional to the photon energy, which means that the contribution to the matrix element increases as the photon energy decreases. This also illustrates how infrared divergences arise as the photon energy tends to zero. It is also possible to observe that as $\cos\theta$ tends to one, or θ tends to zero, the contribution to the matrix element will increase. Thus it is more likely for a photon to have a small energy and/or be collinear with a muon than to have a large energy and be well separated from both muons.

Now consider the phenomenology of the process $e^+e^- \to Z/\gamma \to \mu^+\mu^-\gamma$, where again the photon energy is above the detection threshold. When the photon is radiated from a muon then the phenomenology of the detected particles is generally identical to that described above for the decay $Z \to \mu^+\mu^-\gamma$, allowing for the effect of interference between the Z and photon s channel propagators. However, if the photon is radiated from either the electron or the positron then there are two important effects which affect the phenomenology of the final state particles.

The first effect is that for photons from initial state particles the distribution of the smaller of the two angles between the photon and muons will tend to be flatter, which is due to the fact that a photon is more likely to have a large angular separation from the muons if it has been radiated by an initial state particle. This is because the direction of a photon radiated by an initial state particle is not strongly correlated to the directions of either of the final state muons. This is due to the fermion propagator now being an initial state particle, and thus the θ of equation 1.9 is between an initial state particle and the photon. Therefore the photon tends to be close to one of the initial state particles. The direction of the final state particles is random, within the confines of the differential cross-section, and thus there is little correlation between the direction of the photon and the muons. There is, however, some correlation due to the conservation of momentum, which means that a high energy photon from an initial state particle severely reduces the phase space available to the muons.

Another phenomenological effect of radiation from the initial state particles is most significant when the centre of mass energy for the collision equals M_Z. In this case, when the radiation of photons from initial state particles is ignored, the cross-section for Z exchange is several orders of magnitude larger than that for photon exchange. The effect of including initial state radiation is that the cross-section for Z exchange is reduced by approximately thirty percent, whilst the cross-section for photon exchange is not significantly affected. This is because the probability of an electron-positron annihilation producing a Z has the form of a Breit-Wigner resonance, with the peak being when the centre of mass energy equals M_Z, whilst the probability of an electron-positron annihilation producing a photon is almost flat for centre of mass energies close to M_Z. Initial state radiation lowers the centre of mass energy available for the annihilation and thus lowers the probability that a Z boson will be produced. Conversely initial state radiation increases the probability that an s channel photon will be produced.

Thus, for a centre of mass energy equal to M_Z, initial state radiation lowers the S matrix element where i is an electron and a positron and j is two muons and n photons ($n \geq 0$) by approximately thirty percent.

As explained in the previous section, when an S matrix element is calculated using a perturbation expansion then, following renormalisation, the contribution of a term to the total decreases as the order of the term increases. If this property were not present in the theory then some predictions could not be made as they require the explicit calculation of an infinite perturbation expansion. This is impossible in practice as only a finite number of explicit terms of an expansion series can actually be calculated, and the fact that the contribution of the higher order terms decreases implies that the loss of the higher order terms will not significantly affect the result of the calculation. However, this truncation introduces a theoretical uncertainty on the result of the calculation.

When a theoretical prediction is compared with an experimental result it is important that the theoretical uncertainty is lower than the experimental error. Thus, as an experiment achieves more accurate results it is necessary to reduce the theoretical uncertainty by including higher orders of the perturbation expansion in the calculation of the matrix element. This can create a problem as the inclusion of higher order terms increases the number of Feynman diagrams non-linearly, and thus approximations of higher order effects are used. For higher order photonic corrections two commonly used approximation techniques are exponentiation and the leading logarithm approximation [15]. The former estimates infinite order corrections for the radiation of low energy photons, whilst the latter is employed so that only the significant parts of the higher order photonic terms need to be calculated explicitly.

1.5 Magnetic moments of the fermions within the standard model

The aim of the analysis detailed in chapter 5 is to constrain the anomalous magnetic moment of the tau. Therefore this section will outline how the Dirac equation implies that the fermions have a magnetic moment, and explain the mechanism by which the fermions acquire an anomalous magnetic moment within the framework of the standard model.

The Dirac equation for a free fermion is

$$(\gamma_\mu p^\mu - M_f)\,\psi_f = 0$$

where p^μ, M_f and ψ_f are the four-momentum, mass and wavefunction of the fermion respectively. Now consider the interaction between a fermion of charge eQ_f and an electromagnetic field A^μ $\left(= (A^0, \vec{A})\right)$. To find the effect of the electromagnetic field on the wavefunction of the fermion it is necessary for the substitution $p^\mu \to p^\mu - eQ_f A^\mu$ to be made in the Dirac equation for the free fermion. In the non-relativistic limit, this substitution leads to the Schrödinger-Pauli equation

$$\left(\frac{1}{2M_f}(\vec{p} - eQ_f\vec{A})^2 - \frac{eQ_f}{2M_f}\vec{\sigma}\cdot\vec{B} + eQ_f A^0\right)\psi_f = E_{\rm NR}\psi_f \tag{1.10}$$

where $\vec{B}$ $(= {\rm curl}\vec{A})$ is the magnetic component of A^μ, $\vec{\sigma}$ are the Pauli matrices and $E_{\rm NR}$ $(= E_f - M_f)$ is the non-relativistic energy of the fermion.

Equation 1.10 contains the interaction between the fermion and the electromagnetic field which is due to the electric charge of the fermion, and also includes an interaction which can be interpreted as a coupling between the fermion and the electromagnetic field due to the fermion having a magnetic moment [16]. Thus the fermions have an intrinsic (or spin) magnetic moment $\vec{\mu}_f$, which is defined as

$$\vec{\mu}_f = -\frac{eQ_f}{2M_f}\vec{\sigma} \equiv -g_f\frac{eQ_f}{2M_f}\vec{S} \tag{1.11}$$

where g_f is the gyromagnetic ratio of the fermion and $\vec{S}$ $(= \vec{\sigma}/2)$ is the spin angular momentum operator. Thus, in the non-relativistic limit, g_f has the value two.

The matrix element describing the general relativistic Born level interaction between a fermion and a photon is obtained through Gordon decomposition of the current [17], and has the form

$$\begin{aligned}\langle p_2|J^\mu_{em}(k^2)|p_1\rangle &= -eQ_f\bar{u}(p_2)\left(F^f_1(k^2)\gamma^\mu + \frac{i}{2M_f}F^f_2(k^2)\sigma^{\mu\nu}k_\nu\right)u(p_1) \\ &\quad + e\bar{u}(p_2)F^f_3(k^2)\gamma^5\sigma^{\mu\nu}k_\nu u(p_1)\end{aligned} \tag{1.12}$$

where

$$\sigma^{\mu\nu} = \frac{i}{2}\left(\gamma^\mu\gamma^\nu - \gamma^\nu\gamma^\mu\right)$$

and p^μ_1, p^μ_2 and k^μ $(= p^\mu_2 - p^\mu_1)$ are the four-momenta of the incoming fermion, outgoing fermion and photon respectively. The three Pauli form factors $F^f_1(k^2)$, $F^f_2(k^2)$ and $F^f_3(k^2)$ represent the proportion of the coupling between the fermion and the photon that is due to the electric charge, anomalous magnetic moment and anomalous electric dipole moment of the fermion respectively. To ensure that the conservation of probability is not violated it is required that

$$F^f_1(k^2 = 0) + F^f_2(k^2 = 0) + F^f_3(k^2 = 0) = 1.$$

The factor $F^f_2(k^2)$ is related to the gyromagnetic ratio of the fermion by the relationship

$$F^f_2(0) = \frac{g_f - 2}{2}.$$

Thus the magnetic moment for the fermion obtained using equation 1.10 implies that $F^f_2(0)$ is zero, which means that there is no anomalous contribution in the non-relativistic limit. It is only by considering higher order photonic vertex corrections, e.g. fig. 1.3, that $F^f_2(0)$ obtains a non-zero value.

If the matrix element $\langle p_2|J^\mu_{em}(k^2)|p_1\rangle$ is calculated for the Feynman diagram of fig. 1.3 it is found that an additional contribution is made to the magnetic moment of the fermion predicted by equation 1.10, and now

$$\vec{\mu}_f = -\frac{eQ_f}{2M_f}\left(1 + \frac{\alpha}{2\pi}\right)\vec{\sigma}$$

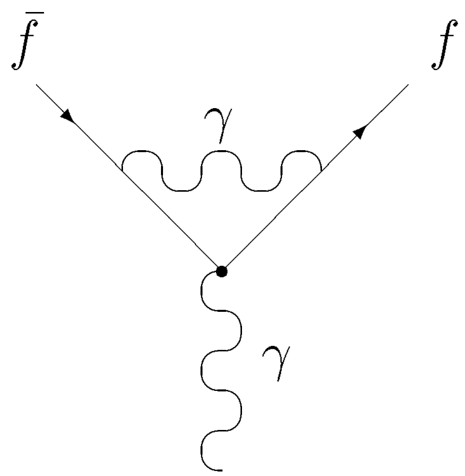

Figure 1.3: The lowest order vertex correction term.

where $\alpha = e^2/4\pi$. Thus the fermions have gained an anomalous magnetic moment within the standard model, and the gyromagnetic ratio is now

$$g_f = 2 + \frac{\alpha}{\pi}.$$

Thus $F_2^f(0)$ has a non-zero value.

The Feynman diagram of fig. 1.3 produces the lowest order vertex correction term. There are infinite number of higher order vertex correction terms, and these lead to the gyromagnetic ratio being given by

$$g_f = 2 + \sum_{n=1}^{\infty} a_n^f \left(\frac{\alpha}{\pi}\right)^n$$

where the coefficients a_n^f are obtained by explicitly calculating the vertex corrections, and $a_n^f \to 0$ as $n \to \infty$.

Thus all the fermions gain an anomalous magnetic moment during the process of applying photonic radiative corrections. The value of $F_2^f(0)$ is different for each fermion as the anomalies are dependent on the mass of the relevant fermion. However, the magnitude of the anomalous magnetic moment is very small for all of the fermions when compared with the non-relativistic prediction of $g_f = 2$. This is illustrated by the results of the calculations of the anomalous magnetic moments of the fermions [18], where it has been found that

$$F_2^e(0) = 115\,965\,214\,0(28) \times 10^{-12}$$

$$F_2^{\mu}(0) = 116\,591\,902(77) \times 10^{-11}$$

$$F_2^{\tau}(0) = 117\,73(3) \times 10^{-7}.$$

Chapter 2

The ALEPH detector

2.1 Introduction

ALEPH is one of four detectors which utilise the LEP storage ring at CERN. The data collected by ALEPH is primarily used to further knowledge about the standard model of particle physics, with the most accurate results coming from the electroweak sector. This involves both rigorous testing of the theory's predictions and constraining some of the 21 free parameters existing in the standard model. This large number of free parameters is an unattractive feature of the model and therefore the data is also used to check consistency of the standard model and search for physics beyond the standard model, both of which are the aims of the analyses in this thesis.

2.2 LEP

The experimental discovery of the neutral weak current in the early seventies verified the theoretical postulate of electroweak unification. In order to study the physics contained in this theoretical framework more precisely the LEP (Large Electron Positron) collider was proposed, with its design parameters being more clearly defined after the discovery of the W and Z bosons by UA2 in 1983 [19] [20]. LEP requires two phases if it is to cover most aspects of electroweak physics. In the first phase, which is in progress, the electron-positron annihilation occurs at energies around the Z pole, whereas in the second phase the annihilations will have enough energy to pair produce on-shell W's.

During normal running LEP acts as a storage ring. Originally there were 4 bunches of electrons and 4 bunches of positrons in circulation, but this was upgraded to eight bunches on eight bunches in 1992, and finally running with bunch trains was adopted in 1995. The bunches are brought into collision at the four experiments and electrostatic separators are used to keep them apart at the other points where a bunch crossing occurs.

Dipole magnets, used to bend the bunches into circular orbits, produces undesirable bremsstrahlung radiation from the beams, the power of which is inversely proportional to the radius of curvature of LEP. This is the main reason for the large 8486 m diameter of LEP. The energy loss due to this radiation is compensated by RF cavities, which are also used to accelerate the beams from 20 GeV to about 45 GeV after injection.

2.3 Overview of ALEPH

ALEPH (Apparatus for LEP pHysics) is a large detector, about 1000 m^3, and was designed to cover all branches of physics available in the LEP environment. ALEPH covers a large proportion of the solid angle in order to maximise the information obtained about each event. This is essential, given the low rate of events at both phases of LEP, if accurate measurements of electroweak parameters are to be made.

ALEPH consists of a barrel region which is closed by two endcaps. An artist's impression of a cut away view of ALEPH is shown in figure 2.1. There are three tracking detectors, all contained in the barrel, with a shell of calorimetry detectors surrounding them.

Moving radially out from the middle of ALEPH, which is the nominal interaction point during a bunch crossing, the tracking subdetectors are encountered

Figure 2.1: The ALEPH detector

first. The first of these is the silicon strip microvertex detector. This is a small detector close to the beam pipe which improves the accuracy of track reconstruction close to the interaction point. Outside this is the inner tracking chamber. This is a conventional cylindrical drift chamber, and is the only tracking chamber used in the first level of triggering. It also provides up to eight accurate rϕ coordinates for track reconstruction. The outermost shell of tracking is provided by the time projection chamber which provides three dimensional track coordinates.

Enclosing the tracking chambers are two levels of calorimetry, separated in the barrel region by a superconducting solenoid. The first level is the electromagnetic calorimeter which, due to high granularity, has good photon and electron identification capability. The outer layer of calorimetry is for particles that penetrate through the first layer, mainly hadrons and muons. Outside the calorimetry is a double layer of streamer tubes covering 92% of the solid angle, which are used in the identification of muons.

The detectors used to monitor luminosity are all close to the beam pipe in order to make use of Bhabha scattering. The primary luminosity measurement is done by a highly segmented silicon/tungsten calorimeter.

This chapter contains only a brief account of the principal components of ALEPH and more complete and detailed descriptions exist [21] [22] [23].

2.4 The micro vertex detector

The micro vertex detector [24], or VDET, encircles the beam pipe and provides tracking points close to the interaction region. It consists of two concentric cylinders coaxial with the beams which are constructed from double sided silicon wafers. The cylinders are approximately 200 mm long and have radii of 63 and 110 mm.

A total of 96 wafers are used in VDET, 40 in the first layer and 56 in the second layer. The silicon wafers have dimensions $51.2 \times 51.2 \times 0.3$ mm. Readout is instrumented on both sides of the wafers, one side giving coordinates parallel to the beam direction (rϕ), and the other giving coordinates perpendicular (rz). On both sides the readout strip is 100 μm across. Interpolation using capacitive charge division is used to find the track impact point between readout strips.

The relative positions of the wafers is found using data and involves no other tracking detectors. A 5% active overlap region of neighbouring wafers in ϕ is used to constrain the relative position of the wafers in ϕ and the average radius of the circle of wafers, whilst $Z \to \mu^+\mu^-$ events constrain the relative position of wafers in different layers and on opposite sides of the detector. This procedure gives point resolution $\sigma_{\mathrm{r}\phi} \approx 12\mu$m and $\sigma_{\mathrm{Z}} \approx 10\mu$m.

The hits from VDET are implemented in track reconstruction during the extrapolation of tracks found in the outer tracking chambers. VDET hits are included by averaging the charge weighted positions of adjacent strips that have at least three times the mean noise charge.

2.5 The inner tracking chamber

The inner tracking chamber [25], or ITC, is a cylindrical multiwire drift chamber with inner and outer radii of 128 and 285 mm and length of 2 m. The ITC has two main purposes - it provides up to eight accurate rϕ coordinates (eight coordinates for tracks with $|\cos\theta| < 0.97$) and it is the only tracking chamber used by the first level trigger as its fast readout allows a trigger decision to be reached within 2-3 μs.

The wires in the ITC run parallel to the beam, or z, axis which means that rϕ coordinates are obtained by measuring the drift time of the ions produced by a charged particle travelling through the ITC. An accuracy of about 150 μm is obtained in rϕ (averaged over the drift cell). It is also possible, by measuring the time difference that an induced pulse takes to reach both ends of the sense wire, to obtain the z coordinate. This can achieve an accuracy of about 70 mm when averaged over z and all layers.

The ITC has 960 sense wires strung between two aluminium end plates which are configured into eight concentric layers, with 96 wires in each of the four inner layers and 144 wires in the outer four layers. Each sense wire is at the centre of a drift cell, being surrounded by six field shaping wires to give the cell hexagonal geometry. This means that four of the field wires are shared with neighbouring cells on the same layer. Only five of the field wires are earthed, the other is insulated from earth and pulses are injected along it during calibration. Combining the need for a fast level 1 decision with the finite drift speed of the gas enables an upper limit for the cell size to be obtained, and the size of cell adopted is less than this maximum. The cells are "close packed", meaning that cells in adjacent layers are shifted sideways by half a cell, resolving the left-right ambiguity which would otherwise be present in track reconstruction.

The gas used in the ITC is Ar(80%) + CO_2(20%) at atmospheric pressure, with the sense wire operating voltage for this mixture between 1.85 and 2.05 kV.

The information for the trigger decision is provided by special fast trigger processors which provide both rϕ and rϕz information. The rϕ trigger decision is delivered in approximately 500 ns whilst the rϕz trigger decision is reached within about 2 μs.

The alignment of the ITC relative to the other tracking chambers is done using $Z \rightarrow \mu^+\mu^-$ and $Z \rightarrow q\overline{q}$ events where the tracks are extrapolated from the TPC into the ITC, and a comparison is made between the predicted and actual hits.

2.6 The time projection chamber

The largest tracking chamber in ALEPH is the time projection chamber [26], or TPC (fig. 2.2). It is of cylindrical geometry, having inner radius of 310 mm, outer radius of 1800 mm and length of 4.7 m. The magnetic and electric fields contained in the TPC are parallel with each other and the beam axis. A central membrane divides the TPC into two halves and creates an electric drift field such that ionisation electrons drift to the endplates where there is a plane of wire chambers. This enables three dimensional coordinates to be obtained, and means the TPC can measure momentum and emission angle of charged tracks with high accuracy. The ionisation density, dE/dx, can also be determined.

Figure 2.2: The ALEPH time projection chamber.

The TPC consists structurally of inner and outer field cages and two endplates. The field cages are coaxial with the beam axis and use copper electrodes to ensure that the electric drift field in the volume between them is constant and parallel to the beam axis. The central membrane is mylar coated on both sides with conducting graphite paint and is held at -27 kV whilst the endplates are connected to ground, giving rise to a electric drift field of 115 V/cm. The gas used in the TPC is Ar(91%) + CH_4(9%) with a drift velocity of 5.2 cm/μs.

The large diameter of the TPC is necessary to measure track momenta precisely and the resultant large endplate area means each endplate has 18 wire chambers, called sectors. The geometry of the cracks between adjacent sectors has been designed to minimise the loss in track momentum resolution (fig. 2.3). Each wire chamber has three layers of wires which act as the gating grid, cathode plane and sense wire plane respectively. Field shaping wires permeate through all three planes. When a negative ion reaches the sense wire it causes an ionisation avalanche which induces a signal on the cathode pad that is 4 mm behind the sense wire. There are 41004 pads in the TPC, each having dimensions $6.2\,\mathrm{mm} \times 30\,\mathrm{mm}$ ($\delta(\mathrm{r}\phi) \times \delta\mathrm{r}$). The signal on the pad is read out for coordinate measurement and the pulses on the wires are used for measuring dE/dx. The second level trigger uses the TPC and there are 32 trigger pads per sector, which are located between the rows of cathode pads.

Figure 2.3: The sectors of the ALEPH time projection chamber.

The gating grid is required to stop positive ions produced in avalanches near the sense wires reentering the drift region, as these ions can change the drift field and cause track distortions. The gating grid is either open, where the passage of charged particles is not impeded, or closed, where a dipole field is created that is opaque to charged particles. The gate is normally closed and is only opened for a bunch crossing.

The rϕ coordinate of a drift electron is obtained by interpolating the signals induced on the cathode pads, whose positions are well known. The r coordinate is found by knowing the radial position of the pad involved, and the z coordinate can be calculated if the drift velocity field is known and the drift time of electron is measured. The TPC can measure 21 three dimensional points for charged particles crossing both inner and outer field cages. The resolution is dependent on the angles which the charged track makes with both the sense wires and the cathode pads. The rϕ spatial resolution for a track with 0^0 pad crossing angle is 180 μm. The z coordinate can be obtained from either the pads or the wires if there are no other tracks crossing the sector. The z spatial resolution for the wires is 1.2 mm (with a slight z dependence), and 0.8 mm (for $\theta = 90^0$) for the pads.

Due to the solenoidal magnetic field all charged particles follow a helical path. The projection of this three dimensional object onto the two dimensional endplate produces an arc of a circle. Using the sagitta of this arc it is possible to find the radius of curvature of the charged particle, which is proportional to the modulus of the track momentum component perpendicular to the magnetic field. The resolution of the transverse momentum p_t (GeV/c), Δp_t, is proportional to the resolution in the measurement of the sagitta, Δs (mm), i.e.,

$$\frac{\Delta p_t}{p_t} = 0.027 p_t \frac{\Delta s}{l^2 B},$$

where B is the modulus of the magnetic field and l (m) is the length of the projected trajectory. The relative error on the measured momentum of a track arises from the error on the transverse momentum as the error on the measurement of the polar angle, θ, is small. The momentum resolution, Δp/p^2, for a 45 GeV track traversing the full TPC radius is 1.2×10^{-3} (GeV/c)$^{-1}$ for the TPC only, 0.8×10^{-3} (GeV/c)$^{-1}$ for ITC + TPC and 0.6×10^{-3} (GeV/c)$^{-1}$ for ITC + TPC + VDET. The error on p_t has a θ dependence because if a track has a large $|\cos\theta|$ then there are fewer measured coordinates and a shorter projected trajectory.

This effect can be expressed as a function of $\cos\theta$.

The calibration of the field in the TPC is carried out using a laser system which produces straight 'tracks'. The measured curvature of these tracks is used to correct sagitta measurements whilst the drift velocity is determined from reconstructed polar angles.

2.7 The electromagnetic calorimeter

The electromagnetic calorimeter, or ECAL, is the inner layer of a double shell of calorimeters. Its purpose is to stop and identify electrons and photons. ECAL is a lead/wire chamber sampling device which is highly granular and hermitic, covering 3.9 π sr with 73728 readout channels. It is situated inside the solenoid to reduce the number of radiation lengths that preceed it, thus reducing preshowering.

Figure 2.4: The electromagnetic calorimeter of ALEPH.

The ECAL surrounds the tracking chambers and consists of a barrel of length 4.77 m and radii 1.85 and 2.25 m, closed at either end by endcaps which have active inner and outer radii of 0.568 and 2.275 m and depth 411 mm. The endcaps and barrel are subdivided into 12 modules, each subtending 30^0 in azimuth. The cracks between the modules, where no readout is possible, constitute 2% of the barrel surface and 6% of the endcap surface. To ensure that the cracks in the endcaps and the barrel are not coincident the endcap modules are rotated through 15^0 in azimuth. Further, to ensure that the cracks in ECAL and the hadron calorimeter are not aligned, the whole of ECAL is rotated by -1.875^0 in azimuth with respect to the hadron calorimeter (fig. 2.4). The mechanics and electronics for the endcap and barrel modules are as identical as possible.

The total energy of electromagnetic showers is measured in the ECAL using approximately 30×30 mm^2 cathode pads. These pads are connected together to give towers which point towards the interaction point and are read out in three sections, called storeys. A module consists of 45 layers of lead and proportional wire chambers, with the first storey ten layers thick (2 mm layers of lead giving 4 radiation lengths total), the second storey 23 layers (2 mm layers of lead giving 9 radiation lengths total) and the third storey 12 layers (4 mm layers of lead giving 9 radiation lengths total). Each tower has a granularity in $\Delta\theta \times \Delta\phi \sin\theta$ of between 17 mrad $\times$ 17 mrad at 90^0 in the barrel, to 10 mrad $\times$ 10 mrad for $36^0 < \theta < 42^0$ in the endcaps. The construction methods used result in a tower to tower uniformity of response within 1.6% (r.m.s.).

The wire chambers are built using an open sided aluminium extrusion. Anode wires sit inside channels on the open face of the extrusion and run parallel to the z axis. Below the extrusion is the cathode plane, which consists of the pads and readout lines. This ensemble is placed behind a highly resistive graphite coated mylar sheet and the resulting wire chamber is placed between two layers of lead sheet (fig. 2.5). Thus an electromagnetic shower, created by a particle travelling through the lead, will cause ionisation avalanches around the anode wires. This ionisation capacitively induces a signal on the cathode pads which is read out. The signals on each plane of wires are summed and also read out.

The gas used in the ECAL is Xe(80%)+CO_2(20%) and is about 60 mbar above atmospheric pressure. Calibration of the gain of the gas system was initially done by including radioactive ^{83}Kr in the gas mixture. The short term drift of the gas gain is done in each module by a dedicated single small wire chamber which contains a ^{55}Fe source. This produces 6 KeV X-rays which induce charge on the

Figure 2.5: The composition of a layer of the electromagnetic calorimeter.

wire.

The ECAL has an energy resolution of $\sigma_E/E = 0.18\ \mathrm{GeV}^{1/2}/\sqrt{E}$, and position resolution $\sigma_x = \sigma_y = 6.8\ \mathrm{mm}\ \mathrm{GeV}^{1/2}/\sqrt{E}$.

2.8 The superconducting solenoid

The magnetic field, vital for obtaining track momenta, is provided by a superconducting solenoid which produces a field of 1.5 T at 5000 A. It is 7 m long with inner and outer radii of 2.48 and 2.92 m. The iron return yolk of the solenoid is fully instrumented as the hadron calorimeter.

The magnetic field produced is parallel to the LEP beam and has homogeneity $\Delta B_z/B_z < 0.2\%$, radial component $B_r/B_z < 0.4\%$ and azimuth component $B_\phi/B_z < 0.04\%$. The non-uniformity of the magnetic field produces sagitta distortions of only 0.2 mm in the TPC.

2.9 The hadronic calorimeter

The Hadronic Calorimeter, or HCAL, is the outer shell of calorimetry and provides information about particles that pass through ECAL, i.e. most hadrons and muons. The iron structure providing the passive part of the calorimetry is also the main structural support for ALEPH and the return yolk for the magnetic field. The polar angle coverage is $6^0 < \theta < 174^0$. As in the case of the electromagnetic calorimeter the hadronic calorimeter has a barrel region which is closed at both ends by endcaps.

The barrel is divided into twelve modules and thus has dodecagonal geometry, with each module split down the middle for construction purposes. The iron of each module is split into twenty two iron slabs, with spacers between each slab to allow insertion of limited streamer tubes to act as the active, or readout, part of the calorimeter. The spacers reduce the azimuithal coverage available to the streamer tubes by 3.4%. The total iron thickness is 1200 mm at $\theta = 90^0$, which corresponds to 7.16 interaction lengths. The first layer of streamer tubes is in front of the first iron slab and is held in place by a 5 mm thick aluminium sheet.

The streamer tubes are made from extruded plastic (PVC) shaped into a base sheet perpendicular to which there are nine fins. This means that there are eight long cells which have internal dimension 9×9 mm^2, and are about 7 m long. The inner surfaces of the the cells are painted with graphite and a 100 μm thick wire runs along the axis of the cell and operates at 4 kV. Opposite the open side of the cell are copper pads. The pads from different layers are summed to form projective towers which subtend 3.7^0 in azimuth at the interaction point and have been designed so each tower has the same width in polar angle. The pattern of towers matches the pattern in the electromagnetic calorimeter, with about fourteen ECAL towers to one HCAL tower. On the opposite side of the cells to the pads is an aluminium strip which runs the length of the cell parallel to the wire. These provide a standard logic signal whenever an avalanche is induced on the wire and are used to obtain a two dimensional picture of hadronic showers and aid in muon identification. Thus there are three types of signal from HCAL - those from the pads which are to measure the energy deposited in the calorimeter, those from the aluminium strips which provide the pattern of fired tubes in an event, and those from the wires which give the energy deposited in a single planes and are used for triggering.

The endcaps are divided into six modules each and are constructed in a similar way to the barrel. The main difference is that 2.1 m radially from the centre the endcaps have only 15 layers to enable them to fit into the barrel.

There are 2688 projective towers fully in the barrel, 2032 fully within the endcaps and 768 which are shared between the barrel and the endcaps.

The gas used in the streamer tubes is Ar + CO_2 + Isobutane in the ratios 12.5% : 56.5% : 30%. To record changes in the gas composition or ambient temperature and pressure, and thus variations in the calibration factor, control tubes are installed in the gas line of each module.

The hadronic calorimeter has energy resolution σ_E/E of $84\%/\sqrt{E}$.

Figure 2.6: The configuration of the x and y strip electrodes in the muon chambers.

2.10 The muon chambers

Outside of the hadron calorimeter are two double layers of streamer tubes which cover 92% of the solid angle. They are used as tracking chambers and do not give information about the hadronic shower energy. They provide two dimensional coordinates by having strip electrodes both parallel and perpendicular to the wire in each cell of the tubes (fig. 2.6).

The tubes follow the geometry of the hadron calorimeter except in the region of overlap between the endcap and barrel, i.e. the outer edges of the endcap modules, where there are additional middle angle chambers. The distance of separation between the double layers is 0.5 m for the barrel region and 0.4 m for the endcaps, which allows track directions for a particle travelling through both layers to be measured with an accuracy of about 10-15 mrad.

2.11 Luminosity detectors

It is essential for accurate physics results that there is a small error on the measurement of integrated luminosity received by ALEPH. Thus low angle elastic (Bhabha) scattering is used to measure the integrated luminosity as it is almost a pure QED process with very little interference from the weak sector, and has a well known cross section.

The luminosity monitors are designed so that their systematic uncertainties are smaller than the statistical error of the measured integrated luminosity. For this precision to be attained it is necessary to detect both the scattered electron and positron in coincidence on both sides of the interaction region. It is also very important to measure accurately the polar angle of both particles as the Bhabha cross section is proportional to one over the fourth power of θ. For particle identification purposes, and thus background rejection, good energy determination is required from these detectors.

Since 1992 the luminosity in ALEPH has been measured using a silicon tungsten calorimeter, SICAL [27]. This consists of two cylindrical calorimeters installed about 2.5 m on either side of the interaction region. The active inner and outer radii on both are 61 and 144 mm which corresponds to θ_{min} and θ_{max} of 24.3 and 57.7 mrad respectively. Both calorimeters are made in two halves and enclose the beam pipe. The detectors are constructed from 12 layers of tungsten sheets between which there are silicon layers, each with 512 readout pads instrumented. There are sixteen 5.2 mm radial pad-rows, each with a ϕ interval of 11.25^0. Consecutive layers of silicon are rotated through 3.75^0 in ϕ to eliminate azimuthal cracks. The energy resolution of SICAL is $\sigma_E/E = 23\%/\sqrt{E}$. The SICAL was designed to produce a systematic uncertainty in the integrated luminosity measurement of less than 0.1%, and this has been improved to about 0.05% during operational running.

Before the installation of SICAL the luminosity calorimeter, or LCAL, measured luminosity. This is a sampling calorimeter based on the design of ECAL with 38 layers of lead sheets and wire chambers. It is made from four semi-cylindrical modules placed around the beam pipe 2.625 m from the interaction point. The systematic uncertainty in the integrated luminosity measurement due to LCAL was designed to be less than 2%, and during running an uncertainty of 0.4% was achieved.

Instantaneous luminosity is provided by the very small angle luminosity monitor, or BCAL. This consists of two pairs of detectors placed at ± 7.7 m from the interaction point and has twenty times more Bhabha events than SICAL due to lower polar angle detection.

2.12 Triggering

ALEPH employs a three level triggering system in order to separate all genuine e^+e^- interactions from background, to reduce the frequency of accepted events to a rate which can be written to tape, i.e. about 1-2 Hz, and to reduce the dead time of the detector. The background events are mainly from three sources - beam-gas interactions arising from a non-perfect vacuum in the beam pipe, off-momentum particles from the beam hitting either the collimators or the vacuum pipe close to ALEPH, and cosmic rays. The luminosity received by ALEPH is low enough for there to be no need to select areas of physics on which to trigger once backgrounds have been eliminated. The trigger has been designed to be sensitive to single particles or single jets.

The maximum output acceptable from the level 1 trigger is a few hundred Hz in order to keep dead time in the data acquisition to a minimum and to ensure there are no TPC gating problems. To enable the trigger to cover all areas of physics it uses information from HCAL, ECAL, LCAL and the ITC. After a bunch crossing there is a level 1 yes if:

- there are track candidates in the ITC;
- there is energy in a ‘trigger region’ of ECAL or HCAL;
- the total energy in the barrel, either endcap or entire detector is larger than given thresholds;
- there is a Bhabha event in SICAL.

Level 1 uses specially built hardware to enable a decision to be reached in 5 μs, and as there is 11 μs between bunch crossing it means that the detector does not miss a bunch crossing if there is a level 1 no. It is common for events to cause more than one trigger and it is therefore possible to measure the fiducial efficiencies of different event types. Level 1 has 100% fiducial efficiency for hadronic Z decays, approximately 100% for leptonic Z decays and $99.7 \pm 0.2\%$ for Bhabha events.

The second level trigger uses only the TPC, and extends the level 1 track information. Again it is based on hard-wired processors. A search is made for tracks straight in the rz plane, as all tracks accepted by level 1 have transverse momentum greater than 1 GeV/c. If level 2 decides to reject an event then the data acquisition is reset by the fifth bunch crossing following the initial level 1 trigger, this being a 58 μs gap and the level 2 decision time being about 50 μs. Level 2 removes approximately 75% of level 1 track only triggers.

The level 3 trigger is applied after readout and is based on software analysis. It is done within the data acquisition system before events are written to tape. Level 3 reconstructs all events which reach it and studies the regions of the detector which triggered the first two levels. The event is accepted and written to tape if this reconstruction validates the trigger decision. This reduces the output frequency to the desired 1-2 Hz.

2.13 Event reconstruction

Event reconstruction is the process where the digital signals from the subdetectors in ALEPH are turned into objects which can be used in physics studies. The two types of objects that are found are tracks, using the three tracking chambers, and calorimeter clusters. This is done off-line by a dedicated facility coupled to the main data acquisition computer.

The method to find tracks starts by using TPC information. Neighbouring hits in the TPC are connected together to form track segments. These segments are joined together if the result is consistent with a helical track hypothesis. The resulting tracks are extrapolated inwards to the other two tracking chambers where appropriate hits are assigned to the tracks. The resulting preliminary tracks are used as inputs to an accurate track fitting procedure, which uses the errors determined from the preliminary track parameters and takes into account multiple scattering.

Clusters are found in both ECAL and HCAL by the following method. All storeys which have an energy deposition greater than 30 MeV and are connected by a minimum of a storey edge or corner are collected together and called clusters. In the electromagnetic calorimeter corrections are made to a clusters energy to allow for storey threshold effects, ionisation losses for charged particles in the tracking detectors, leakage of electromagnetic showers which punch through ECAL and penetrate HCAL, and the non-linearity of calorimeter response which was found in test beam results.

2.14 Particle identification

The high granularity of both ECAL and HCAL are important for the identification of muons and photons, both of which are used in the analyses in this thesis.

2.14.1 Muon identification

The identification of muons has a high efficiency and purity since they have an unusual signature. The identification procedure makes use of the digital readout of the HCAL, which acts as a tracking detector, to see if a particle traverses the whole of HCAL.

All tracks with momentum greater than 1.5 GeV/c are checked against a muon hypothesis. This is done by extrapolating each track through HCAL as though it were a muon, making allowances for the accurate magnetic field map and estimated energy losses. A road through HCAL around the extrapolated track is created with a width three times the multiple scattering uncertainty resulting from the extrapolation. HCAL planes which are within the road are expected to have fired. A hit is included in the identification procedure only if no more than three adjacent tubes have fired. Only tracks with momentum greater than 3 GeV/c are considered muon candidates. This increases the efficiency of detection if the track is a muon because it guarantees it will completely traverse the calorimeter. Hits from the muon chambers are attributed to the extrapolated track if the distance between the two is less than four times the estimated standard deviation due to multiple scattering. After the above procedure, a track is considered a muon if the number of planes fired in total is greater than 9, out of the last ten planes more than four fired, a non zero number of the last three planes fired, or the number of hits in the muon chambers is greater than zero.

Therefore due to the muon's extremely long interaction length it has an easily identifiable signature. Monte Carlo studies have shown that for a 95% fiducial efficiency of identifying a 5 GeV muon the probability of mistaking a π for a μ is 0.7% and a K for a μ is 1.6%.

2.14.2 Photon identification

The three dimensional segmentation of ECAL ensures good photon resolution is possible up to the highest LEP energies available. A photon identification package is required because the clustering algorithm in the event reconstruction builds clusters which are too large and contain more than one photon. The photon package starts by considering the clusters found in the event reconstruction but uses the assumptions that electromagnetic showers tend to begin in the first segment in depth of ECAL and that photon clusters are very compact.

The method used to identify candidate photons starts by looping over, in decreasing energy, the ECAL clusters found by the reconstruction algorithm. Firstly the inner layer of the towers is searched for all possible photon cluster seeds, i.e. a storey without a more energetic neighbour. Following this the other storeys are added to the appropriate seeds to make clusters; the outer layers being added sequentially. This method takes advantage of the compactness of electromagnetic clusters and the good projective geometry of ECAL. Finally, a new cluster is declared a photon candidate if its energy is greater than 0.25 GeV and no charged track is within 20 mm of the energy weighted mean centre of the cluster.

The position of the photon impact point is given by correcting the cluster barycentre to allow for the finite size of the calorimeter cells. The photon energy calculation uses the four central towers of the cluster and the expected value of the fraction of energy in the four towers, F_4. This fraction has been obtained by parametrising the shower shape for a single photon in ECAL. The effects of the calorimeter pad area, the distance between the photon impact and nearest tower corner and the variation with energy of F_4 are all included in the photon energy calculation.

The spatial resolution obtained is $\sigma_{\theta\phi} = (2.5/\sqrt{E/\mathrm{GeV}} + 0.25)$ mrad and the energy resolution $\sigma_E/E = 0.25/\sqrt{E}$. The energy resolution is worse than the expected $0.18/\sqrt{E}$ since only the four central towers of the cluster are used.

2.15 Energy flow

The energy resolution of an event can be improved by using an energy flow algorithm. This method links charged tracks to calorimeter objects and uses the redundency in energy measurements that results to assign neutral particle energy. It also uses particle identification methods.

The method begins by considering all charged tracks found in the reconstruction. It produces a subset of good tracks which require at least four TPC hits (if the track has momentum greater than 15 GeV/c then it requires at least 8 TPC hits and 1 ITC hit) and which must originate from a cylinder of length 200 mm and radius 20 mm which is coaxial with the beams and centered on the interaction point. This will exclude all V0 candidates so these are searched for and reinstated. When dealing with the calorimeter known noisy channels are masked out from the cluster finding and the readout redundency in both calorimeters is made use of to smooth occasional noise.

The next stage is to associate good charged tracks with calorimeter objects. All good charged tracks are called charged energy and they are assumed to be pions unless they have already been identified. Electrons, muons, photons and π^0's which have been identified are removed from the lists taking the appropriate energy from the associated calorimeter object. This should leave only charged and neutral hadrons. Lastly the energy of the tracks is subtracted from the calorimeter objects, and if the remainder is larger than 500 MeV it is attributed to neutral hadrons.

This algorithm enables a relative energy resolution of less than 9% to be obtained regardless of the energies involved.

2.16 Detector simulation by Monte Carlo

Most analyses require the use of complicated cuts which mean that Monte Carlo methods are favoured over semi-analytical ones. A Monte Carlo program will generate individual events which can be given the same structure as real data and thus the same analysis can be applied transparently to both sets of data. To generate Monte Carlo is a two stage process, initially simulating the physics under study and then simulating the detector.

The differential cross section for a given physics process can be expressed in terms of phase space variables. By using a random number generator it is possible to obtain values for these variables and thus calculate the differential cross section for these given values. It is relatively simple to convert phase space variables to the four momenta of the particles, thus events can be created and a differential cross section used to measure the likely occurence of this event geometry. Therefore the first stage of generation involves obtaining four momenta and calculating the probability for this particular configuration to have occured.

The second stage is to simulate the passage of the generated particles through the detector, taking into account particle lifetimes and decays. The method used is based on the GEANT/GHEISHA approach [28], producing an output which has the same structure as the data. After this stage the Monte Carlo undergoes the same procedures as data.

Chapter 3

A study of radiative muon events at LEP

3.1 Introduction

The ensemble of LEP and its detectors provides a platform which can be used to probe the electroweak sector of the standard model with a high degree of accuracy, enabling a definitive study of radiative corrections to be undertaken. Such a study is required to check the self consistency of the theory and to understand the phenomenological implications of these corrections.

If the standard model is a physical theory then all calculations done in its framework using perturbation theory must be self consistent to all orders of the expansion. The implications of this constraint mean that all terms in the expansion must be finite and that as the order of a term increases its contribution to the sum over all orders decreases. For the standard model to be a self consistent theory the application of a process known as renormalisation is required. This process involves redefining the physically observable parameters of the theory so that infinities produced by higher order corrections have no effect on the physical predictions of the theory.

If the predictions of the renormalised standard model are not compatible with experimental results then either there is a fundamental flaw in the theoretical understanding of renormalisation or else there is physics beyond the standard model which produces phenomenological effects at the energy scale of the experiment.

Theoretical models containing physics beyond the standard model often predict, at the electroweak energy scale, a larger number of energetic photons isolated from tracks than the standard model does. An example of such a theory is compositeness [12]. Therefore, in order to find an indication of new physics, the analysis detailed in this chapter involves using ALEPH data collected between 1990 and 1993 to study the reaction $e^+e^- \to Z \to \mu^+\mu^- + n\gamma$ $(n \geq 1)$, and comparing the results obtained with theoretical predictions made in the framework of the standard model.

3.2 Phenomenology

It is possible that some of the photons created by the decay $Z \to \mu^+\mu^- + n\gamma$ will not be detected by ALEPH. This is because if the energy of a photon is below a certain threshold then the signal from the electromagnetic calorimeter caused by the photon is indistinguishable from electronic noise. Therefore the detected topology of an event is not always the same as the topology created by the decay. Such a change in topology can not be identified using the missing mass of the event because the energy of the undetected photon is extremely small.

The change in event topology which occurs because of the experimental inability to detect very low energy photons is necessary for the standard model to remain renormalisable. This is because the infinities produced by attaching virtual photons to the external fermion lines of a specific event topology are cancelled by the divergences resulting from the addition of extremely low energy real photons. Such cancellations can only occur if both corrections have the same topology following experimental detection. This is true in this case as the energies of the real photons required to produce the divergences are lower than the detection threshold (section 1.4.2).

Experimental problems are also encountered if a photon is collinear with a track. Here misidentification of either one or both particles can result, or the measurement of their four-momenta is inaccurate.

Events containing photons with either of the above properties (i.e. low energy or collinear with a track) create problems for theorists because the cross-section calculations including such regions of phase space are complex. Therefore it is both experimentally and theoretically advantageous to only consider those photons in an event which have a non-negligible energy (for example 5% of the centre of mass energy) and are well separated from all charged tracks. Events containing such photons are also a signal for new physics and a method is therefore required for this analysis to distinguish between energetic isolated photons and soft and/or collinear photons. Thus when a $\mu^+\mu^- + n\gamma$ ($n \geq 1$) final state is searched for only the former type of photons will be counted.

The dimensionless parameter y_{cut} is used to classify the photons in an event into those which are isolated and energetic and those which are collinear and/or soft. This parameter is defined by requiring that

$$\begin{aligned} (p_{\mu^-} + k_i)^2 &> y_{cut} M_Z^2 \\ (p_{\mu^+} + k_i)^2 &> y_{cut} M_Z^2 \end{aligned} \tag{3.1}$$

where k_i^ν, $p_{\mu^-}^\nu$ and $p_{\mu^+}^\nu$ are the four-momenta of the i^{th} photon, the muon and the antimuon respectively. From this definition it is possible to conclude that y_{cut} is dependent on both the angles between the muons and the photons and the energies of these particles. This means that the same range of y_{cut} values for which the inequalities 3.1 are satisfied can apply to different final state geometries of the same topology. As an example consider the $\mu^+\mu^-\gamma$ topology, where it is possible for an event with an energetic photon collinear with a muon to have the same range of y_{cut} values as an event with a low energy photon which is well separated from both muons. Thus as y_{cut} increases the soft and/or collinear photons in an event will be excluded, leaving only the energetic photons which have a large angular separation from the muons. Therefore, as photons from new physics tend to be energetic and well separated from tracks [29], only large values of y_{cut} are considered in this analysis.

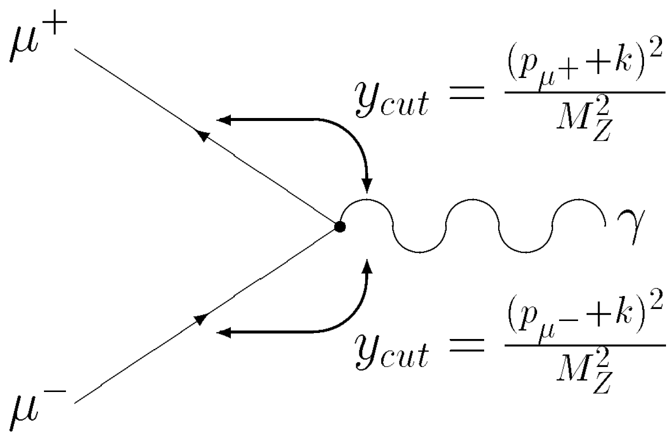

Figure 3.1: An example of obtaining the maximum y_{cut}.

If the muons are assumed to be massless then the maximum y_{cut} of an event which will satisfy the inequalities 3.1 becomes a function of the energies of the photons and the muons and the angles between the photons and the muons. An event with n photons has 2n candidates for the maximum y_{cut} allowed by the inequalities 3.1, and the value adopted for the maximum is obviously the lowest of these candidates. Fig. 3.1 shows an example for the decay $Z \to \mu^+\mu^-\gamma$. Here there are two values of y_{cut} due to the topology, but the geometry of the event dictates which one is the lowest and hence for what range of y_{cut} the inequalities 3.1 are valid.

By considering the inequalities 3.1 it is possible to derive two important phenomenological relationships. Firstly, there is a y_{cut} dependent lower limit imposed on the energy of the photons in an event, which is

$$E_\gamma^{min} = y_{cut}\sqrt{s}. \tag{3.2}$$

The second relationship determines the maximum y_{cut} that can be obtained by an event of a given topology, and is

$$y_{cut}^{max}(n) = \frac{1}{2n} \tag{3.3}$$

where n is the number of photons in the event topology.

The final results of this analysis will be expressed in the form adopted by Stirling [29], i.e. to produce the ratio $R_n(y_{cut})$ where

$$R_n(y_{cut}) = \frac{\Gamma(Z \to \mu^+\mu^- + n\gamma)}{\Gamma(Z \to \mu^+\mu^-)}. \tag{3.4}$$

This ratio is a function of y_{cut} because, as shown above, each event has a value of y_{cut} which cannot be exceeded if the inequalities 3.1 are to remain valid. Therefore as y_{cut} is increased some $\mu^+\mu^- + n\gamma$ will no longer be included in the width $\Gamma(Z \to \mu^+\mu^- + n\gamma)$, and thus the value of R_n is dependent on y_{cut}.

Expressing the final result in the form of $R_n(y_{cut})$ has both experimental and theoretical advantages. The main experimental advantage is that $R_n(y_{cut})$ is independent of the experiment and therefore it is possible to compare the result with theoretical predictions. An important theoretical advantage is that if $\sqrt{s} = M_Z$ then the equation relating the width and cross-section for a final state X is

$$\sigma(e^+e^- \to Z \to X)|_{\sqrt{s}=M_Z} = \frac{12\pi}{M_Z^2}\frac{\Gamma_{e^+e^-}\Gamma_X}{\Gamma_Z^2} \tag{3.5}$$

which leads to

$$\frac{\Gamma(Z \to \mu^+\mu^- + n\gamma)}{\Gamma(Z \to \mu^+\mu^-)} = \frac{\sigma(e^+e^- \to Z \to \mu^+\mu^- + n\gamma)}{\sigma(e^+e^- \to Z \to \mu^+\mu^-)}. \tag{3.6}$$

Therefore whilst the final result can be quoted in terms of partial widths, which are experimentally easier to obtain than cross-sections, the theoretical values for $R_n(y_{cut})$ can be obtained using cross-sections. The importance of this is that cross-sections include correlations between initial and final state particles, such as the forward-backward lepton asymmetry, whereas widths do not. Another theoretical consideration is that the value of the peak cross-section is very sensitive to electroweak corrections, but by forming $R_n(y_{cut})$ many of these corrections cancel and are no longer significant.

3.3 Data analysis

A large fraction of the events which trigger the ALEPH detector are Z boson decays. The remaining events come from interactions such as t-channel Bhabha scattering, cosmic showers, off-momentum beam particles and instances where there is a photon exchanged in the s-channel rather than a Z. The purpose of this analysis is to distil from these events the subset which can be used to construct $R_n(y_{cut})$.

The analysis has two stages - firstly to extract the events with the correct topology, and then to purify this subset so that it contains events mainly from the interaction $e^+e^- \to Z \to \mu^+\mu^- + n\gamma$. The cuts used in these two stages are explained below.

Only data which has been collected at the peak is used for this analysis as some of the theoretical results considered include calculations only valid for this centre of mass energy. Data collected in 1990, 1991, 1992 and 1993 was used to build a sample with a total integrated luminosity of 47.4 pb^{-1}.

3.3.1 The Monte Carlo generators required

When carrying out an analysis it is necessary to use Monte Carlo events which have undergone detector simulation (section 2.16) in order to develop cuts which remove events arising from processes not under study (background) whilst keeping most of the events from the process under study (signal). This is impossible using only data as the reaction which produced a detected event is never known.

To ensure that virtually all of the processes that produce events which occur in the data were considered the following Monte Carlo generators were used:

- BABAMC [30] [31] [32] generates $e^+e^- \to e^+e^-(\gamma)$ events. It includes full $\mathcal{O}(\alpha)$ electroweak corrections, but does not include full exponentiation, higher order corrections to the Z width and the energy dependence of the Z width;

- KORALZ [33] [34] [35] generates $e^+e^- \to \mu^+\mu^-$ and $e^+e^- \to \tau^+\tau^-$ events. It contains second order initial state radiation with full exponentiation, but there is only first order final state radiation;

- HVFL generates $e^+e^- \to q\overline{q'}$ events within the JETSET73 [36] framework;

- PHOPHO [37] generates $e^+e^- \to e^+e^-X$ events, where X is created by gamma-gamma annihilation and can be either a multihadronic state via the VDM process, a pair of leptons produced through QED or a single resonance;

- GGMJET [38] is an implementation of the multijet QCD processes in gamma-gamma collisions, where two primary high p_T jets are produced along with one or two beam pipe jets from the photon.

It is necessary to normalise the output of all of the Monte Carlo generators before any comparisons can be made between their combined results and those of experimental data. The method used to normalise the Monte Carlo output in this analysis is to scale the Monte Carlo results by the ratio of the integrated luminosities of the data and the generated Monte Carlo events.

The integrated luminosity of the data, $\mathcal{L}_{\mathrm{DATA}}$, is obtained using

$$\mathcal{L}_{\mathrm{DATA}} = \frac{n_{Z\to\mathrm{had}}}{\sigma_{Z\to\mathrm{had}}}$$

where $n_{Z\to\mathrm{had}}$ and $\sigma_{Z\to\mathrm{had}}$ are the number of $Z \to$ hadron decays and the cross-section for $e^+e^- \to Z \to$ hadron measured by ALEPH respectively [39].

When a Monte Carlo generator is run it calculates the cross-section for the events generated, and thus

$$\mathcal{L}_{\mathrm{MC}} = \frac{n_{\mathrm{generated}}}{\sigma_{\mathrm{calculated}}}.$$

Therefore the normalisation factor for a set of Monte Carlo generated events is $\mathcal{L}_{\mathrm{DATA}}/\mathcal{L}_{\mathrm{MC}}$.

The processes simulated by Monte Carlo generators which are used in this analysis are shown in table 3.1 along with the normalisation factors that are required for the generated events. It should be noted that the process with a normalisation factor greater than one does not make a significant contribution to the final result.

Process	Normalisation factor
$e^+e^- \to e^+e^-$	0.545
$e^+e^- \to \mu^+\mu^-$	0.183
$e^+e^- \to \tau^+\tau^-$	0.0988
$e^+e^- \to q\bar{q}'$	0.323
$\gamma\gamma \to e^+e^-$	0.648
$\gamma\gamma \to \mu^+\mu^-$	0.614
$\gamma\gamma \to \tau^+\tau^-$	0.588
$\gamma\gamma \to q\bar{q}'$	1.65

Table 3.1: The Monte Carlo simulated processes required for this analysis and the normalisation factors for the generated events used.

3.3.2 Topological selection

The event topology that is required is two good tracks along with at least one photon. Good tracks are found by placing additional constraints on the subset of charged tracks produced by energy flow (section 2.15). The energy flow subset of charged tracks is obtained by applying the following cuts to the tracks found during event reconstruction:

- the number of TPC hits ≥ 4 (if the track has momentum ≥ 15 GeV/c then there must be at least 8 TPC hits and 1 ITC hit);
- the radial distance of closest approach to the beam axis < 2 cm;
- the z coordinate of the closest approach of to the beam axis < 10 cm.

The additional constraints required of a good track are that:

- the angle between the charged track and the beam axis $> 18.2°$;
- the z coordinate of the closest approach of the charged track to the beam axis < 7.5 cm.

The former ensures that the track travels through the tracking subdetectors and is therefore well measured whilst the latter is a slight tightening of the energy flow constraint. If two such tracks are found in an event then two further cuts are applied to reject events which are unlikely to have arisen from a Z decay. Firstly, it is required that the sum of the track charges is zero, and secondly that the total transverse momentum of the tracks is greater than 1 GeV/c.

Photons are found using a method similar to that employed for tracks. Objects which energy flow has designated as electromagnetic calorimeter objects with no associated track are considered to be photons for the purpose of this analysis. This is valid as complex photon identification (section 2.14.2) is required only where there is the possibility of misidentifying another particle as a photon. This is possible, for example, in the decays $Z \to q\overline{q'}+n\gamma$ or $Z \to \tau^+\tau^-+n\gamma$ where there can be other neutral particles. In the decay $Z \to \mu^+\mu^- + n\gamma$ it is unlikely that there are photon candidates which are not photons. The reason for not imposing harsh cuts before a candidate is declared a photon is that a higher efficiency of identification is obtained.

To obtain well defined photons for this analysis the following cuts were made on the energy flow photons:

- the angle between the photon and the beam axis $> 18.2°$;
- photon energy > 3 GeV.

The former is to make sure that the barycentre of the photon is not in the lower region of the electromagnetic calorimeter, where photon energy is not well measured, and the latter is imposed because equation 3.2 shows that low energy photons can never have an associated y_{cut} which is large enough to be relevant for this analysis.

The number of data and Monte Carlo events which survive the topological selection cuts are 80015 and 84385 respectively (table 3.2). The Monte Carlo total is 14.0 standard deviations higher than the data if the errors on both the data and the Monte Carlo are taken into account. Tables 3.3 and 3.4 show the contributions of the individual Monte Carlo generators, where the number of events has been rounded following normalisation.

Cut	Data	MC sum	$\frac{\text{MC}-\text{data}}{\sqrt{\sigma^2_{\text{data}}+\sigma^2_{\text{MC}}}}$
None	ALL	2141861	
Topological selection	80015	84385	14.0
Muon identification cut	10888	11165	2.6
Visible energy cut	5352	5775	5.7

Table 3.2: Effect of the cuts on data and summed Monte Carlo.

	$e^+e^- \to e^+e^-$	$e^+e^- \to \mu^+\mu^-$	$e^+e^- \to \tau^+\tau^-$
Number of events generated	280000	390953	710000
Normalised number of events generated	147728	67733	67691
Topological selection	54031	5964	23296
Muon identification cut	0	5840	5299
Visible energy cut	0	5704	69

Table 3.3: Breakdown of numbers for electroweak Monte Carlo generators.

	$e^+e^- \to q\overline{q'}$	$\gamma\gamma \to X$
Number of events generated	4384159	430780
Normalised number of events generated	1371803	486906
Topological selection	425	670
Muon identification cut	2	23
Visible energy cut	1	1

Table 3.4: Breakdown of numbers for non-electroweak Monte Carlo generators.

Only events containing exactly two good tracks and at least one good photon survive the topological selection cuts. The plots of fig. 3.2 show that virtually all of the 14.0 standard deviation difference between the data (80015 events) and the Monte Carlo (84385 events) is due to events where there are either one or two good photons; there is good agreement for events containing between three and eight good photons. This suggests that there is not an overall systematic effect causing the 14.0 difference, but rather that the Monte Carlo produces too many events with one or two photons.

Consider the case when the final state topology is two tracks and one good photon. Fig. 3.2 (b) shows that the Monte Carlo is approximately 12 standard deviations larger than the data for this topology. The plots in fig. 3.3 show the distributions of the photon energy versus the cosine of the isolation angle of the photon (the isolation angle being defined as the smaller of the two angles between the photon and the tracks and is denoted by $\theta_{\mu\gamma}$) for the data and Monte Carlo. It is possible to conclude from these plots that there is good general agreement between data and Monte Carlo, but fig. 3.4, which shows the number of standard deviations between data and Monte Carlo for each of the channels of fig. 3.3, illustrates that under close scrutiny there are significant differences. It can be deduced that the Monte Carlo predicts too many events with either a low energy photon or a photon close to a track whilst not predicting enough events containing a high energy photon which is well separated from both tracks.

The major contribution to the Monte Carlo total following the topological selection comes from the Bhabha generator BABAMC, and fig. 3.5 shows that it makes at least fifty percent of the contribution to the channels of fig. 3.4 where the Monte Carlo is very much larger than the data. Therefore it is possible to conclude that the main reason for the Monte Carlo total being significantly larger than the data is because of the contribution from the BABAMC generator. The reasons why this conclusion were reached are outlined below.

The cross-section obtained when BABAMC is run is slightly too large because the generator does not include higher order corrections to the Z width and the energy dependence of the width. This means that the normalisation factor for

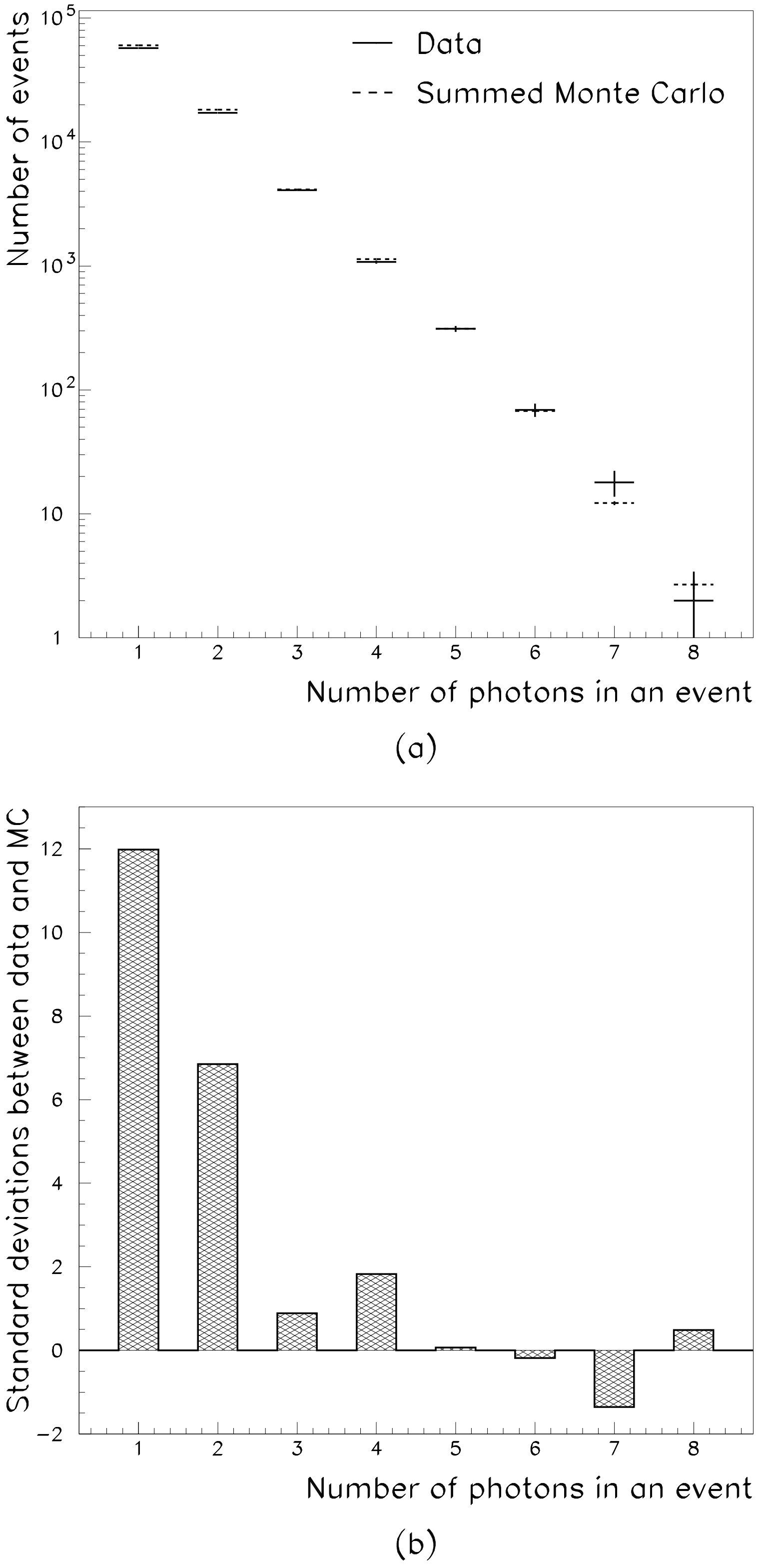

Figure 3.2: Plots showing (a) the number of photons per event in data and Monte Carlo after topological cuts, and (b) the number of standard deviations between data and Monte Carlo in (a).

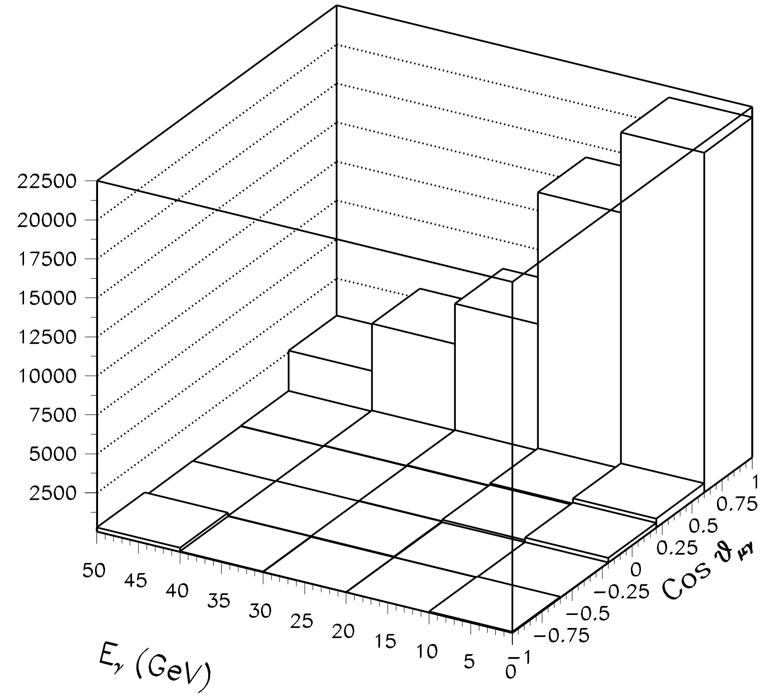

(a)

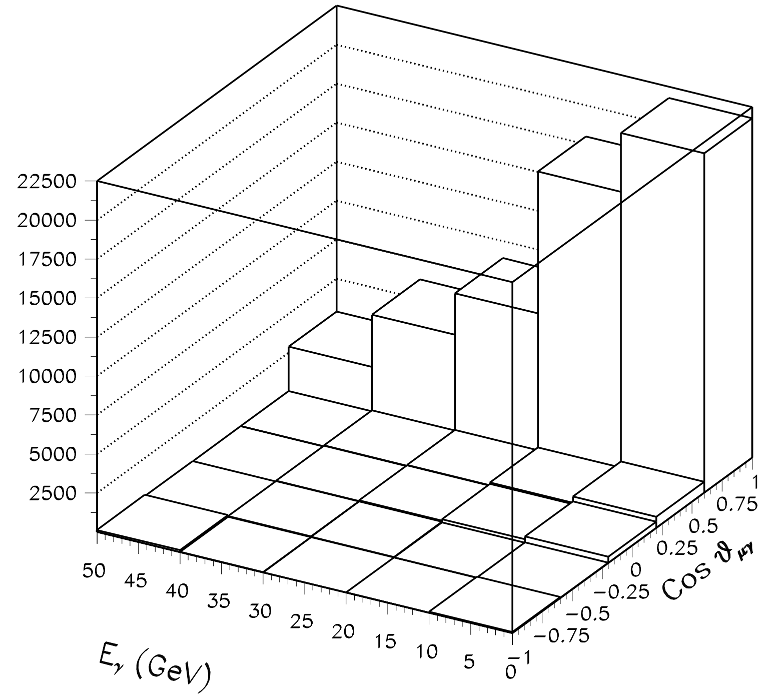

(b)

Figure 3.3: The photon energy versus the cosine of the photon's isolation angle for $\mu^+\mu^-\gamma$ final states in (a) the data and (b) the Monte Carlo after the topological cuts have been applied.

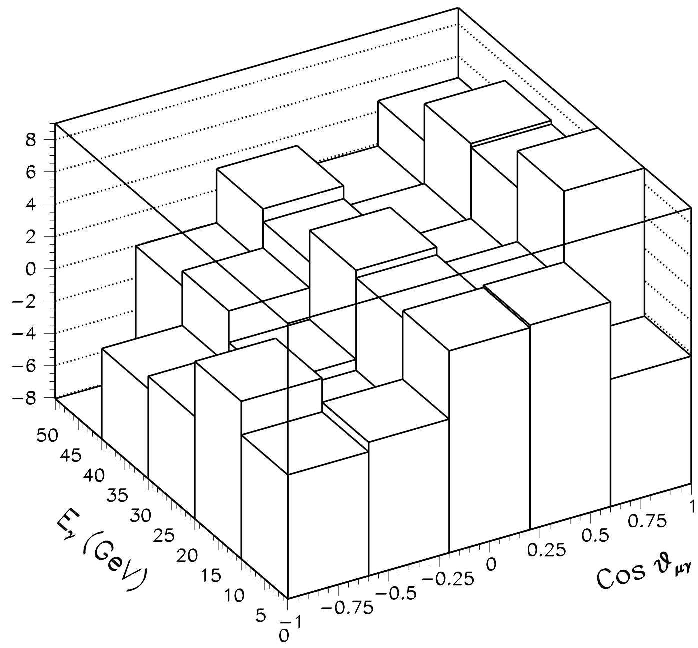

Figure 3.4: The number of standard deviations between the data and the Monte Carlo following the topological cuts.

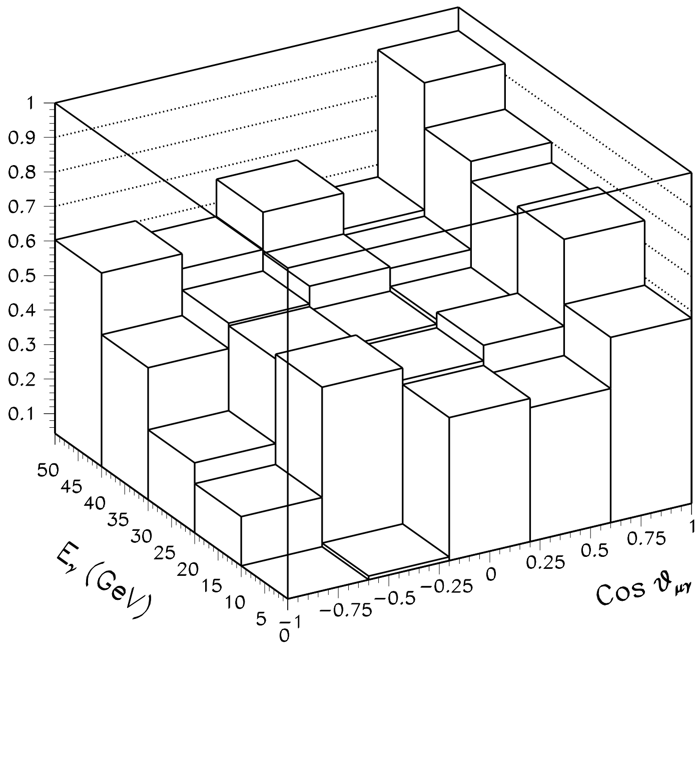

Figure 3.5: A plot showing the fractional contribution of the Bhabha Monte Carlo to the Monte Carlo total following topological cuts.

BABAMC is slightly larger than it should be, and thus there are too many Bhabha events predicted. Another problem arises because BABAMC was mainly designed to predict the low angle scattering events which are used to monitor and measure the integrated luminosity received by ALEPH. Therefore the distributions for large energy photons and photons well separated from tracks are not correctly implemented. These arguments may suggest that another Monte Carlo generator should have been used to simulate $e^+e^- \to e^+e^-$ events. BABAMC is, however, the most reliable Bhabha Monte Carlo generator available for this analysis.

The predicted number of tau Monte Carlo events is much larger than that of the muon Monte Carlo because of the additional photons created during tau decays, both directly and through π^0 decays.

3.3.3 Background rejection

Following the topological cuts the aim of the analysis is to isolate a sample mainly consisting of events from the process $e^+e^- \to Z \to \mu^+\mu^- + n\gamma$ ($n \geq 1$). The level of purity of the sample affects the efficiency of the selection process, and therefore some contamination from other processes is inevitable if the efficiency is to be maintained at a reasonable level.

The first stage of the process of isolating the sample with which the results can be obtained makes use of the high efficiency with which ALEPH identifies muons (section 2.14.1).

The ALEPH muon identification program either rejects a candidate track or, depending on which subdetectors have been triggered, provides a muon identification number. This number can have one the following values:

- = 1 if flagged a muon by only the hadronic calorimeter;
- = 2 if flagged a muon by only the muon chambers;
- = 3 if flagged a muon by both the hadronic calorimeter and the muon chambers;

- $= 10$ if the track produced one hit in each layer of the muon chambers but the tight matching to the muon hypothesis fails;
- $= 11$ if the track produced a good pattern in the hadronic calorimeter;
- $= 12$ if the track produces one and only one good hit in the muon chambers;
- $= 13$ if the track produced a good pattern in the hadronic calorimeter and one and only one good hit in the muon chambers;
- $= 14$ if the track produced a good pattern in the hadronic calorimeter and one hit in each layer of the muon chambers;
- $= 15$ if the track produced one hit in each layer of the muon chambers which passes the tight matching to a muon hypothesis.

If the candidate is rejected as a muon then the identification program returns zero.

If the identifications attributed to the tracks in data and Monte Carlo are compared the agreement is superficially good, as the plots in fig. 3.6 illustrate. However, if the muon identifications of the Monte Carlo plot are divided by those of the data it is possible to observe that for certain muon identifications there is a poor match (fig. 3.7). This arises because the Monte Carlo detector simulation of ALEPH has been optimised to facilitate faster running, which means that not all of the subdetectors are fully simulated. In order that muons are still found with the same efficiency in data and Monte Carlo the identification program was tuned, but only the muon identification numbers 3, 13 and 14 were used. Thus only this subset of the identified muons produce the same results in data and Monte Carlo [23].

The large rise at the origin in fig. 3.7 is because the Bhabha Monte Carlo overestimates the normalised number of events, as explained in the previous section.

In order to reduce the systematic error introduced by muon identification it is only required that at least one of the candidate tracks returns a value of 3, 13

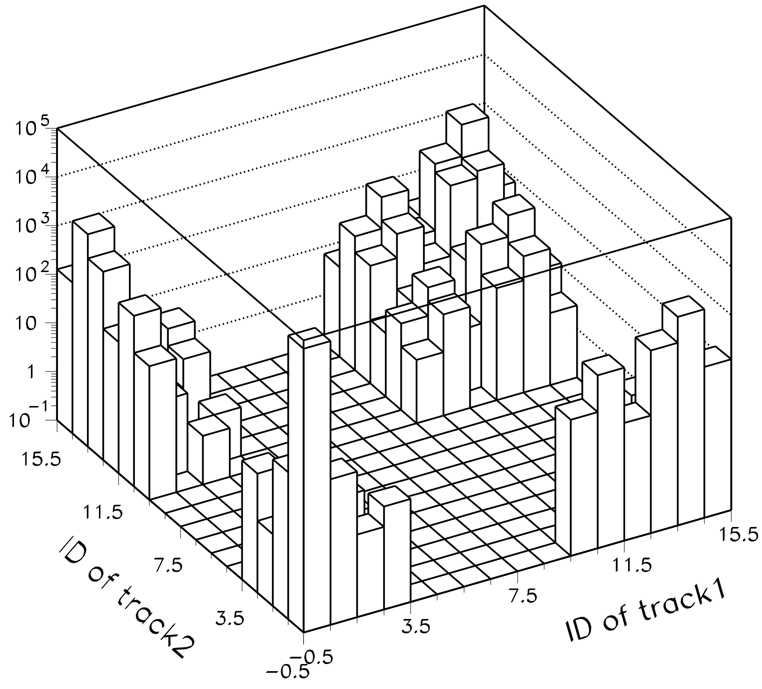

(a)

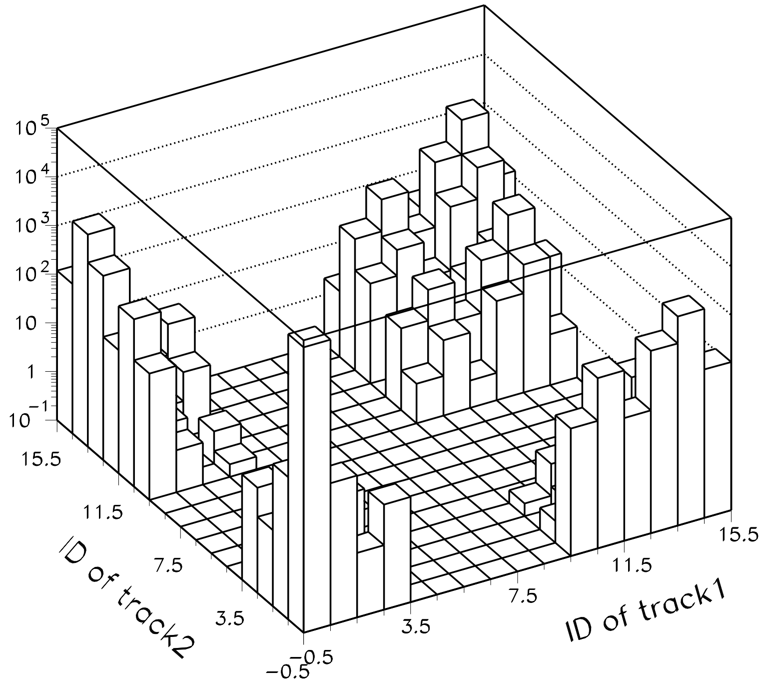

(b)

Figure 3.6: A plot showing the muon identifications of track 1 versus track 2 for (a) data and (b) Monte Carlo.

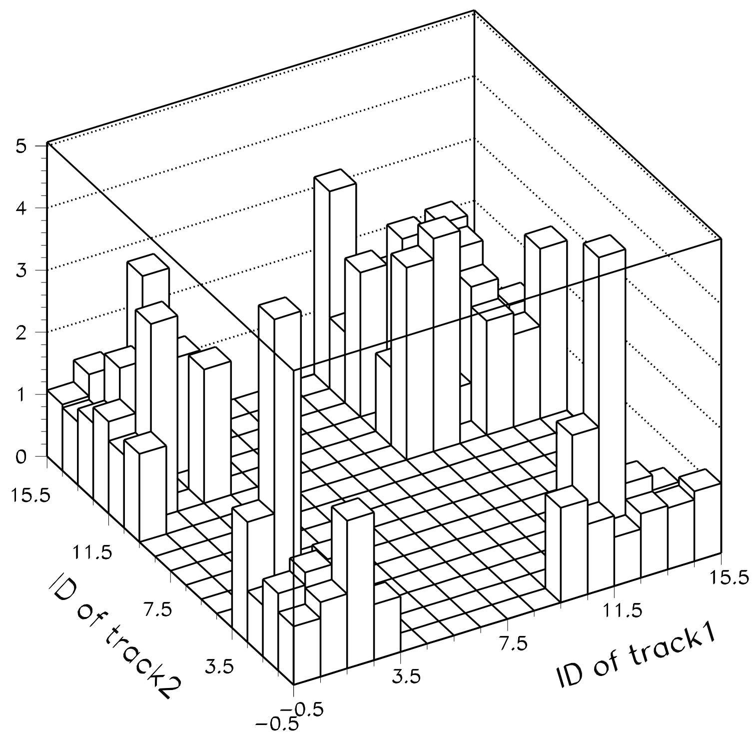

Figure 3.7: The result of dividing the muon identifications of Monte Carlo by those of the data.

or 14. This creates a problem as $Z \to \tau^+\tau^-$ events where only one tau decays to a muon can be accepted, therefore increasing the contamination, but this is rectified later with a cut to reduce the tau background.

The results of the muon identification cut are contained in tables 3.2, 3.3 and 3.4. Table 3.2 shows that the Monte Carlo and data totals are now 11165 and 10888 respectively, a difference of 2.6 standard deviations.

The cut on muon identification has reduced the Bhabha contribution to zero, and the number of standard deviations between data and Monte Carlo has also decreased from 14.0 to 2.6. Thus the conclusion reached in the last section that the BABAMC Monte Carlo was the cause of the 14.0 standard deviation difference between data and Monte Carlo appears to be valid.

The remaining background consists almost wholly of events arising from the decay $Z \to \tau^+\tau^-$. Taus decay within a couple of centimetres of the production

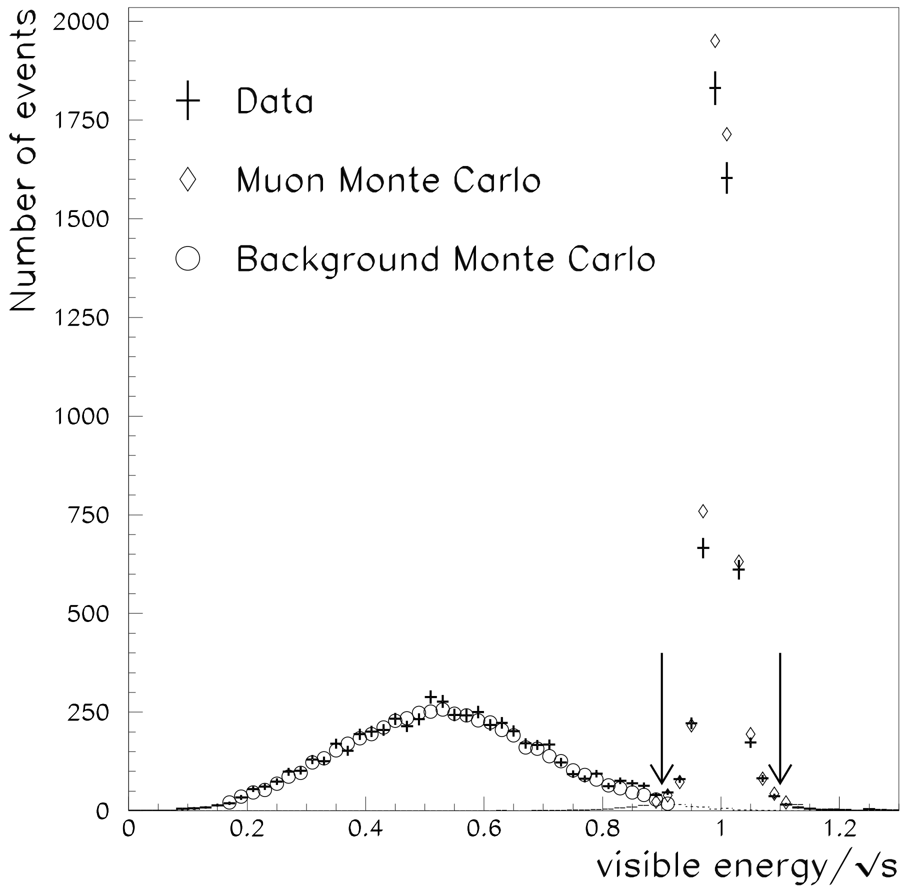

Figure 3.8: A plot of the total visible energy in the event for data and Monte Carlo.

point with at least one neutrino associated with each decay. Thus some of the energy of the event escapes detection. Therefore a reduction in this background will result from a cut on the total energy carried by the detected particles.

The total detected energy, or visible energy, in the event was found by summing all of the energy flow objects. The resulting plot of visible energy/$\sqrt{s}$ for all events is shown in fig. 3.8. From this plot it can be seen that if the region for which $0.9 <$ visible energy/$\sqrt{s}$ < 1.1 is considered the muon Monte Carlo purity is greatly enhanced (the two arrows on the plot indicate these two limits). For this region the Monte Carlo is 5.7 standard deviations above the data (tables 3.2, 3.3 and 3.4).

An upper limit was imposed because the tails of distributions are not always simulated properly by both Monte Carlo generators and detector simulation, and it is therefore safer to avoid these regions.

Therefore the generic topologies for $Z \to \mu^+\mu^- + n\gamma$ have been isolated from the initial samples leaving 5352 data events and 5775 Monte Carlo events, a difference of 5.7 standard deviations. The plots of fig. 3.9 show that the reason for this discrepancy is that the number of $\mu^+\mu^-\gamma$ final states predicted by Monte Carlo is over eight standard deviations larger than the data. It is interesting to note that the Monte Carlo prediction for the number of $\mu^+\mu^-\gamma\gamma$ final states is approximately twelve standard deviations lower than the data, suggesting that there is not a systematic problem with the method used to normalise the Monte Carlo to the data.

The deficiency of the Monte Carlo for $\mu^+\mu^-\gamma\gamma$ events is created by an absence of a smaller number of events than the number of additional events overpredicted for the $\mu^+\mu^-\gamma$ final state. This means that if the $\mu^+\mu^-\gamma$ and $\mu^+\mu^-\gamma\gamma$ events are combined then the Monte Carlo is still 5.4 standard deviations larger than the data. The difference between the Monte Carlo predictions for $\mu^+\mu^- + k\gamma$ $(k \geq 2)$ and the data are all less than two standard deviations, although the low number of events in these cases means that any systematic effects would be swamped by the statistical errors.

That the number of $\mu^+\mu^-\gamma$ events is larger in the Monte Carlo than the data and yet the number of $\mu^+\mu^-\gamma\gamma$ events lower illustrates the inadequacies of the generator used to simulate $Z \to \mu^+\mu^- + n\gamma$ $(n \geq 1)$ events. For this analysis these events are simulated by KORALZ, which is not fully second order in α; whilst there can be either two initial state photons or an initial and final state photon in an event, it is not possible for there to be two final state photons. This explains why the number of $\mu^+\mu^-\gamma\gamma$ events is lower in Monte Carlo than data, and such a deficiency enhances the number of $\mu^+\mu^-\gamma$ events. This is because some of the $\mu^+\mu^-\gamma$ events should be $\mu^+\mu^-\gamma\gamma$ events, partially explaining why the Monte Carlo is high for $\mu^+\mu^-\gamma$ events. However, as mentioned above, adding the $\mu^+\mu^-\gamma$ and $\mu^+\mu^-\gamma\gamma$ events still leaves the Monte Carlo higher than the data. Therefore it appears that KORALZ predicts too many events with a $\mu^+\mu^-\gamma$ final state even after correcting for the fact that it is not fully second order in α.

The plots in fig. 3.10 show that the Monte Carlo and data distributions of photon energy versus the cosine of the photon's isolation angle for $\mu^+\mu^-\gamma$ events are similar in form, but fig. 3.11 illustrates some subtle differences between the data and Monte Carlo distributions. The Monte Carlo predicts too many events where the photon has an isolation angle of less than 90°, in particular there are many more events where the photon is collinear with a muon. The data, however, has more events with a high energy isolated photon than the Monte Carlo predicts, but the overprediction of Monte Carlo events with a collinear photon far outweighs this small excess in data.

Therefore the reason why the Monte Carlo is 5.7 standard deviations higher than the data is because of the excessive number of $\mu^+\mu^-\gamma$ events predicted by the Monte Carlo where the photon is collinear with a muon.

The topological selection and background rejection procedures have produced samples of Monte Carlo and data with a high purity of $Z \to \mu^+\mu^-\gamma$ events, and it is now possible to construct $R_1(y_{cut})$ and $R_2(y_{cut})$ so that comparisons can be made with theoretical predictions.

3.4 The results for $R_1(y_{cut})$ and $R_2(y_{cut})$

It is possible to show, using equations 3.4, 3.5 and 3.6 along with $n = \sigma \mathcal{L}$ (where n is the number of events produced by a given process with cross-section σ for integrated luminosity $\mathcal{L}$), that for the data and Monte Carlo samples $R_n(y_{cut})$ is given by

$$R_n(y_{cut}) = \frac{\text{Number of } \mu^+\mu^- + n\gamma \text{ events}}{\text{Number of } \mu^+\mu^- \text{ events}}. \tag{3.7}$$

The selection procedures outlined in the previous section provide data and Monte Carlo samples which can be used to produce the numerator of equation 3.7. To obtain the denominator it is assumed that a $\mu^+\mu^-$ event can contain two muons and m photons ($m \geq 0$) in the final state. This definition of a $\mu^+\mu^-$ event is adopted as a complicated set of cuts would have to be devised to determine

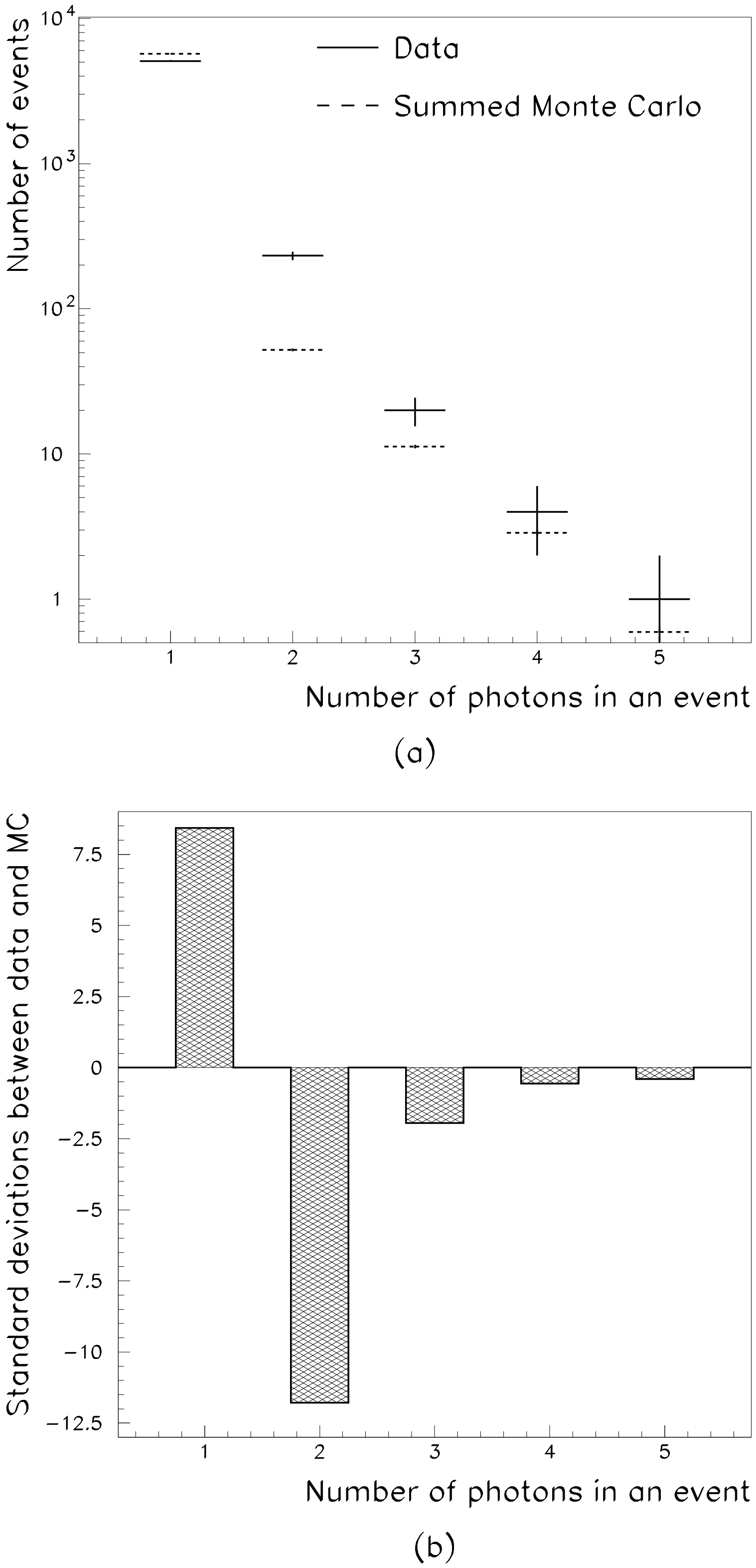

Figure 3.9: Plots showing (a) the number of photons per event in data and Monte Carlo after topological and background rejection cuts, and (b) the number of standard deviations between data and Monte Carlo in (a).

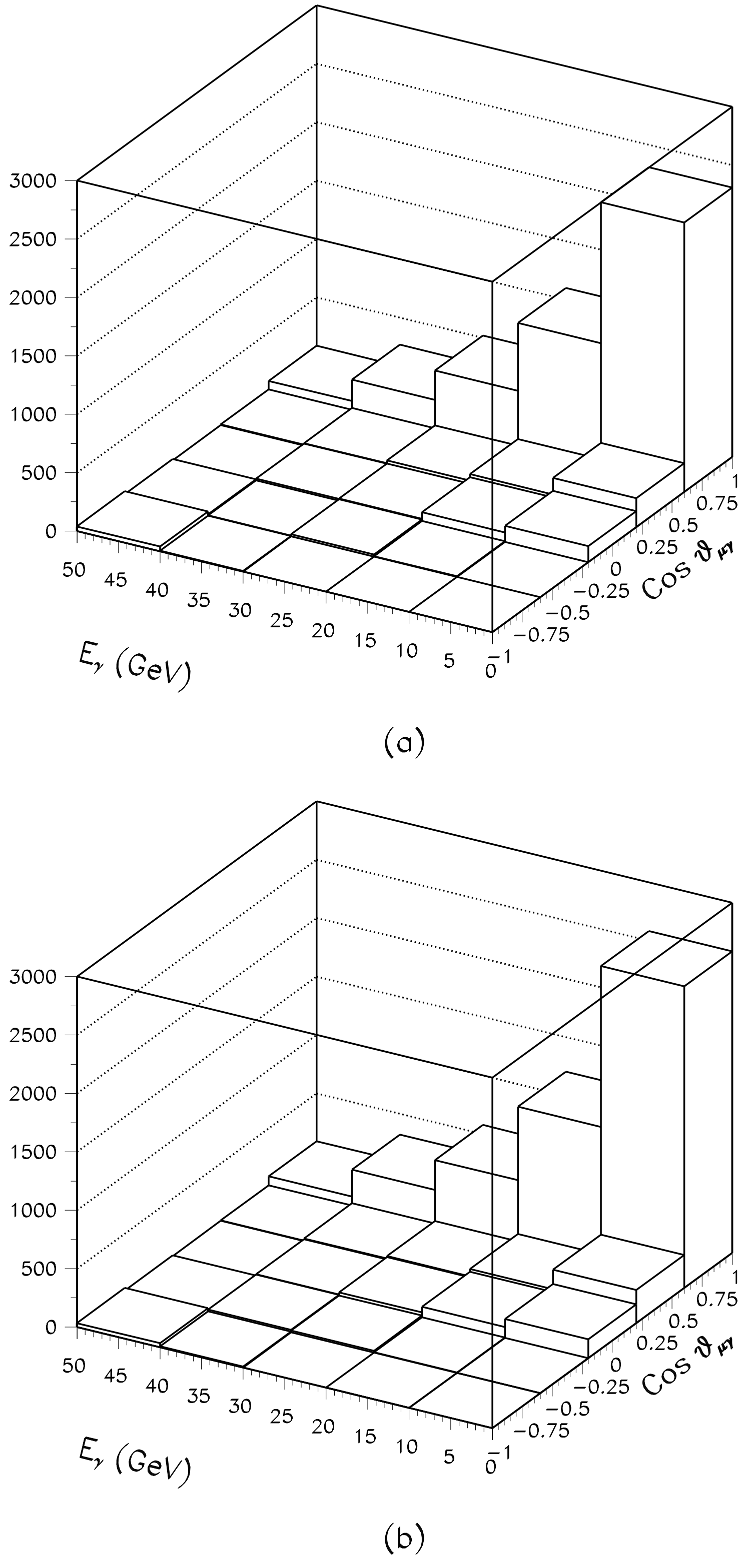

Figure 3.10: Plots showing the photon energy versus the cosine of the photon's isolation angle for $\mu^+\mu^-\gamma$ final states in (a) the data and (b) the Monte Carlo after the topological and background rejection cuts have been applied.

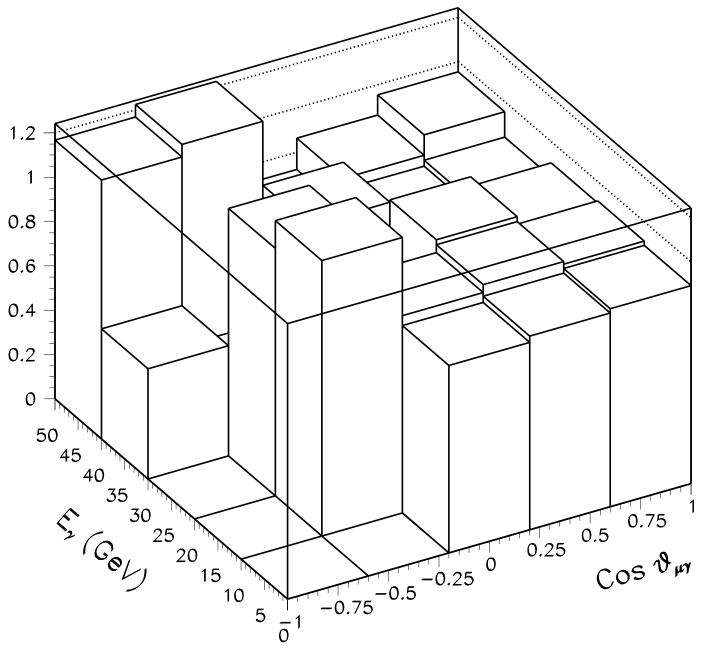

Figure 3.11: The ratio of the data and the Monte Carlo distributions of photon energy versus the cosine of the photon's isolation angle for $\mu^+\mu^-\gamma$ events following topological, muon identification and visible energy cuts.

whether a low energy electromagnetic calorimeter cluster constituted a photon if it was necessary to have only two muons and no photons. In addition, the difference between the numbers of events with final states of $\mu^+\mu^-$ and $\mu^+\mu^- + m\gamma$ $(m \geq 0)$ is of the order of a percent. This is because the effect of radiating an additional photon reduces the probability of the interaction occuring by $\alpha(M_Z) \approx 1/128$.

To obtain the number of $\mu^+\mu^- + m\gamma$ $(m \geq 0)$ events the topological selection and background rejection processes were applied to the data and Monte Carlo with all cuts relating to photons removed. There are 60798 data and 60240 Monte Carlo events surviving these cuts, the difference between these results being 2.1 standard deviations. Combining this result, where there is more data than Monte Carlo, with the result obtained for $\mu^+\mu^- + n\gamma$ $(n \geq 1)$, reinforces the argument that the Monte Carlo predicts too many events containing photons, especially since the method of identifying photons has similar efficiencies in data and Monte Carlo [23].

The first stage of deriving a plot of $R_n(y_{cut})$ for the data is to create a sample of events with two muons and exactly n good photons. This is used to create a plot of the number of $\mu^+\mu^- + n\gamma$ events versus y_{cut}. To achieve this the range of y_{cut} values which satisfy the inequalities 3.1 are determined for each event, and one is added to all of the channels of an appropriately defined histogram which lie within each event's range of valid y_{cut} values. The final plot of $R_n(y_{cut})$ is realised by dividing all of the channels of the histogram with non-zero entries by the total number of $\mu^+\mu^- + m\gamma$ ($m \geq 0$) events. Exactly the same procedure is used to procure the plot for the Monte Carlo sample.

Fig 3.12 contains $R_1(y_{cut})$ for data and Monte Carlo along with the ratio of these distributions. It is possible to observe that the Monte Carlo is systematically higher than the data for low values of y_{cut} whilst the data is higher at large y_{cut}. Given that a low y_{cut} indicates low energy and/or collinear photons whilst a large y_{cut} is only obtained by isolated high energy photons, these plots vindicate the conclusion previously reached concerning the inadequacies of the Monte Carlo.

The three theoretical predictions for $R_1(y_{cut})$ which are compared with the data and Monte Carlo results are from Stirling [29], from a collaboration with Summers [40] and from a set of KORALZ events which have not been subjected to detector simulation.

The method employed by Stirling to obtain $R_1(y_{cut})$ is to use a phase space generator to produce either two or three four-vectors which all have zero mass and whose sum in both cases is $(M_Z, \vec{0})$. By interpretting these as $\mu^+\mu^-$ and $\mu^+\mu^-\gamma$ final states it is possible, using Monte Carlo integration techniques [41], to calculate both $\sigma(e^+e^- \rightarrow Z \rightarrow \mu^+\mu^-)$ and $\sigma(e^+e^- \rightarrow Z \rightarrow \mu^+\mu^-\gamma)$. Equations 3.4 and 3.6 show that $R_1(y_{cut})$ can be obtained by constructing the ratio of these two cross-sections. In order to simplify the cross-section calculations Stirling assumes that initial state radiation and s channel photon exchange are negligible.

Summers calculates $R_1(y_{cut})$ using exactly the same methodology as Stirling but includes the effects of both initial state radiation and s channel photon exchange when calculating the cross-sections.

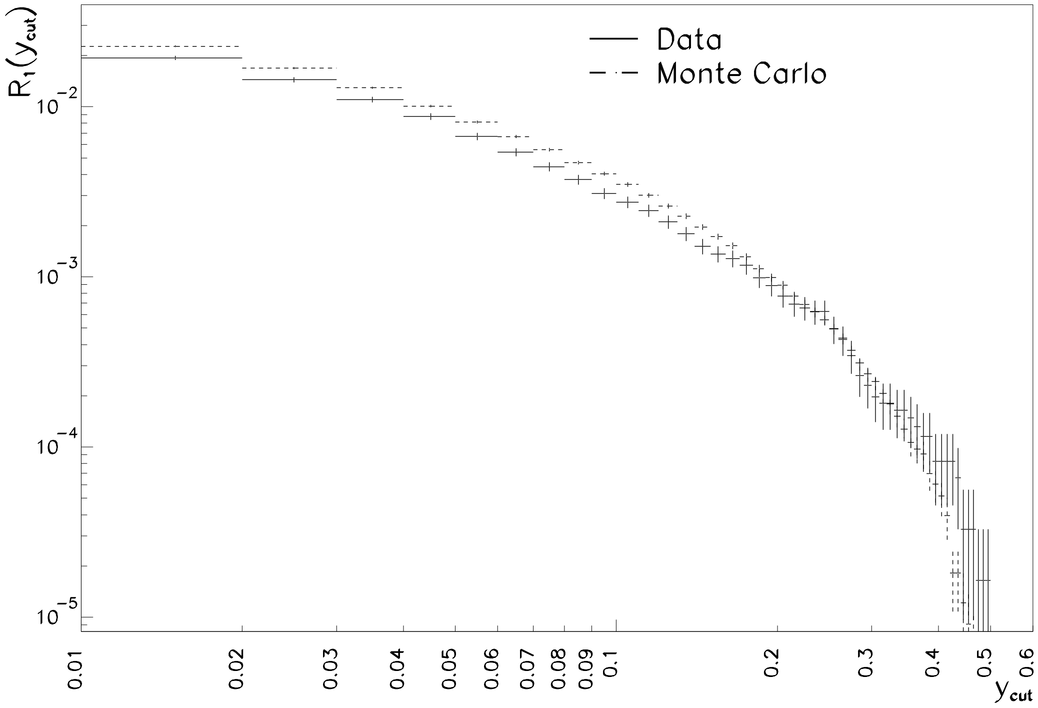

(a)

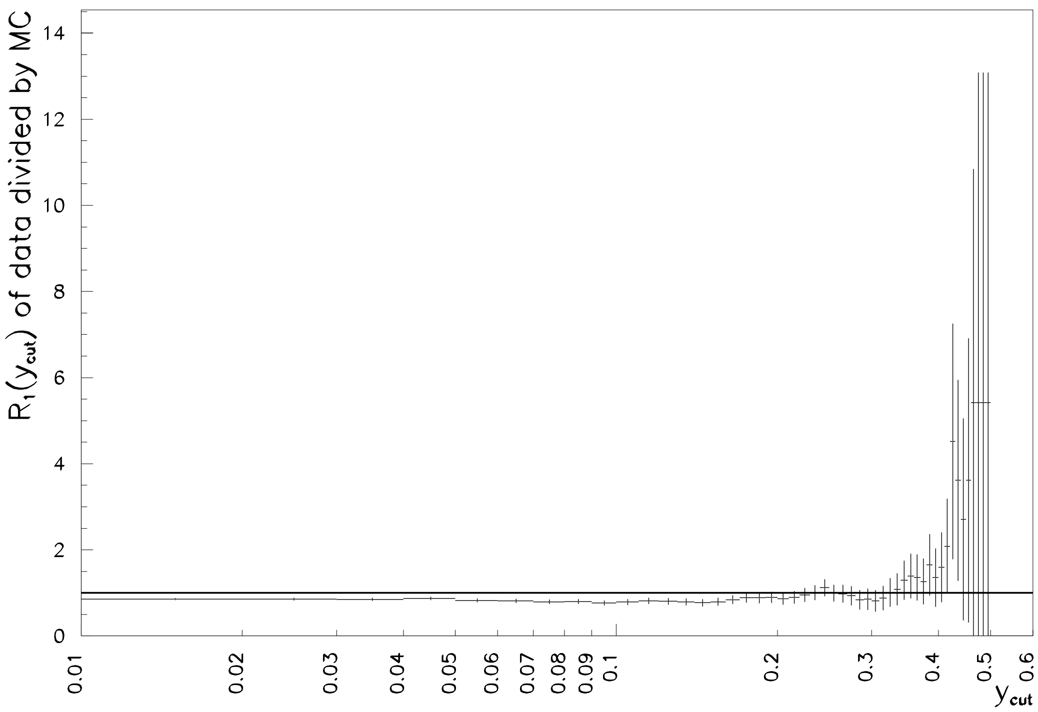

(b)

Figure 3.12: Plots showing (a) the $R_1(y_{cut})$ distributions of data and Monte Carlo and (b) the ratio of the data and Monte Carlo distributions.

Equation 3.7 is used as the basis for obtaining $R_1(y_{cut})$ from KORALZ, where the number $\mu^+\mu^-$ and $\mu^+\mu^-\gamma$ events are obtained using Monte Carlo truth.

The predictions of Stirling, Summers and KORALZ for $R_1(y_{cut})$ are shown in fig. 3.13. The following cuts were implemented in the programs used to obtain the three theoretical results so that the region of phase space considered is the same as that of the data.

- $|\cos\theta| < 0.95$ for all generated four-vectors;
- the energy of the four-vector representing the photon is required to be greater than or equal to 3 GeV;
- the total transverse momentum of the four-vectors representing the muons is required to be greater than 1 GeV/c;
- the modulus of the total momentum of the generated track four-vectors is required to be greater than 0.5 GeV/c.

It is possible to deduce from fig. 3.13 that Stirling's result is lower than both Summers and KORALZ for large y_{cut}. This deficiency is because of the assumptions made by Stirling that initial state radiation and s channel photon exchange are negligible in this instance. If these assumptions are not made then the fact that there is a pole in the cross-section for s channel photon exchange when a large energy initial state photon forces the final state muons to be collinear creates a large proportion of the events at large y_{cut}. This explains why Stirling's prediction is low for large y_{cut}.

The plot of fig. 3.14 enables a comparison to be made between the $R_1(y_{cut})$ distribution of the data and the theoretical predictions. It can be seen that the data is much lower than the theory over most of the range of y_{cut} values. A possible explanation of the poor agreement is that the theoretical results have not been fully corrected for the effects of the data selection process; only simple geometric cuts have been implemented in the programs which produce the theoretical results whilst no allowance has been made for the inefficiencies of muon or photon identification.

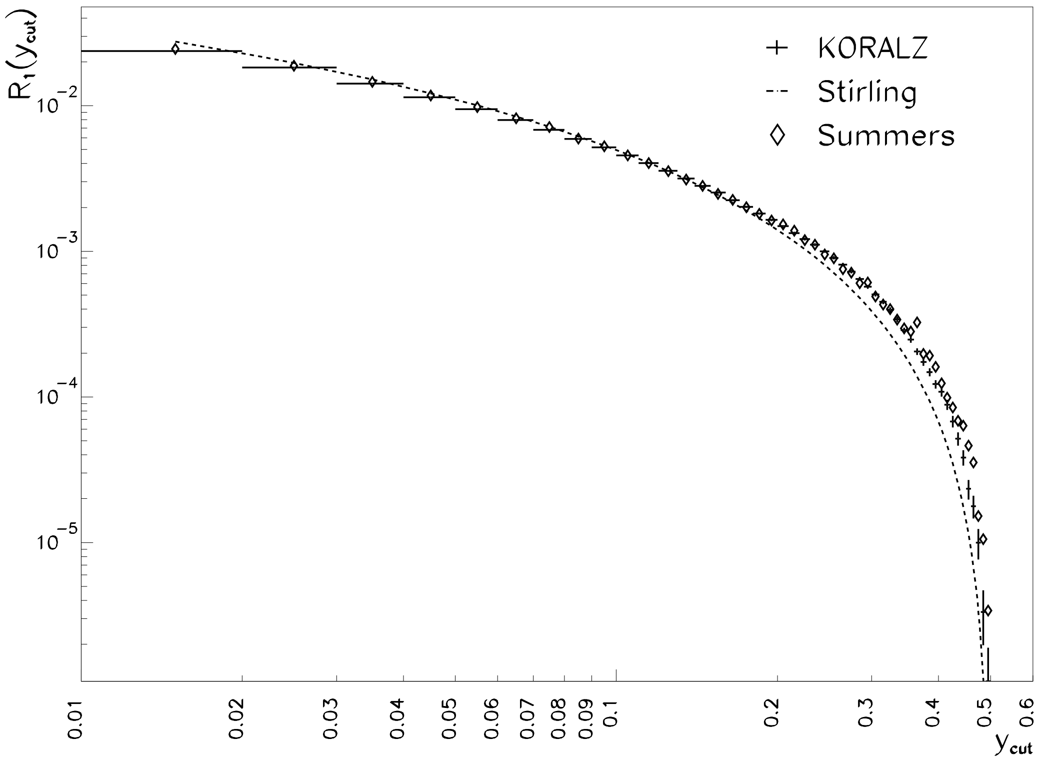

Figure 3.13: A plot showing $R_1(y_{cut})$ for KORALZ, Stirling and Summers.

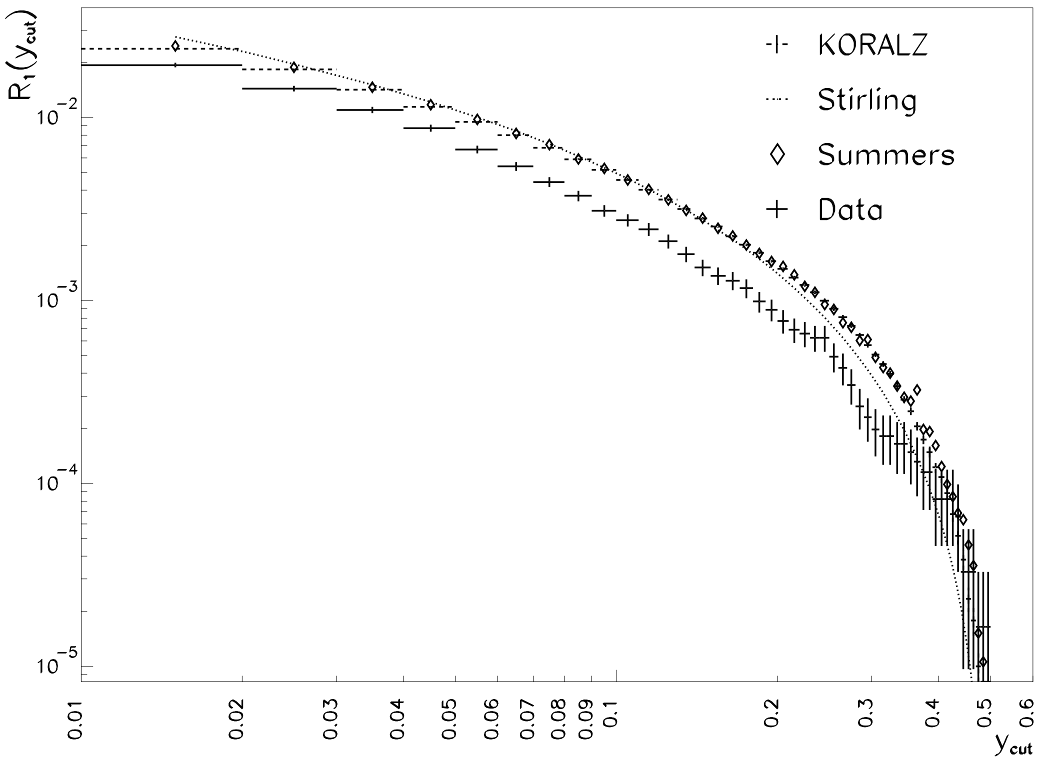

Figure 3.14: A plot showing $R_1(y_{cut})$ for data, KORALZ, Stirling and Summers.

A method of correcting the $R_1(y_{cut})$ distributions of Stirling and Summers so that all of the effects of the data selection process have been taken into account is to use a scaling factor provided by the ratio of the $R_1(y_{cut})$ distributions of the Monte Carlo and KORALZ. This is a valid procedure as both distributions are produced by the same generator, and therefore any systematic effects should cancel in the ratio, leaving a y_{cut} dependent efficiency.

Fig. 3.15 contains the $R_1(y_{cut})$ distributions for the data and corrected theoretical predictions. Figs. 3.16 and 3.17 show the ratio of the data and corrected Summers and Stirling distributions respectively. The agreement between data and the theoretical predictions is improved by the correction for the effects of selection efficiency but the theory is still systematically high for low values of y_{cut}. A possible source of this systematic shift is the contamination of the data by events which are not from $Z \to \mu^+\mu^-\gamma$ decays. This effect is small, but if coupled with other small effects, such as the fact that the theoretical predictions use the uncorrected Born matrix element to determine $\sigma(e^+e^- \to Z \to \mu^+\mu^-)$ whereas the method for the data uses $\mu^+\mu^- + m\gamma$ $(m \geq 0)$ events, a systematic effect could be possible.

The ratio of data and corrected Summers shown in Fig. 3.16 appears to be almost independent of y_{cut}, showing that allowing for a constant systematic effect there is extremely good agreement between these two distributions. The absence of both initial state radiation and s channel photon exchange in Stirlings calculation is the reason for the excess of data at large y_{cut} in fig. 3.17.

The plots of $R_2(y_{cut})$ for the data, Monte Carlo and Stirling can be seen in fig. 3.18. The Monte Carlo is systematically lower than the data because, as stated before, the Monte Carlo used to generate $\mu^+\mu^-\gamma\gamma$ events is not fully second order in α; the possibility of two final state photons being missing. The only theoretical prediction for $R_2(y_{cut})$ available is provided by Stirling. It is possible to conclude from fig. 3.18 that there is good agreement between data and Stirling. However the low number of data events involved means that no subtle differences can be observed.

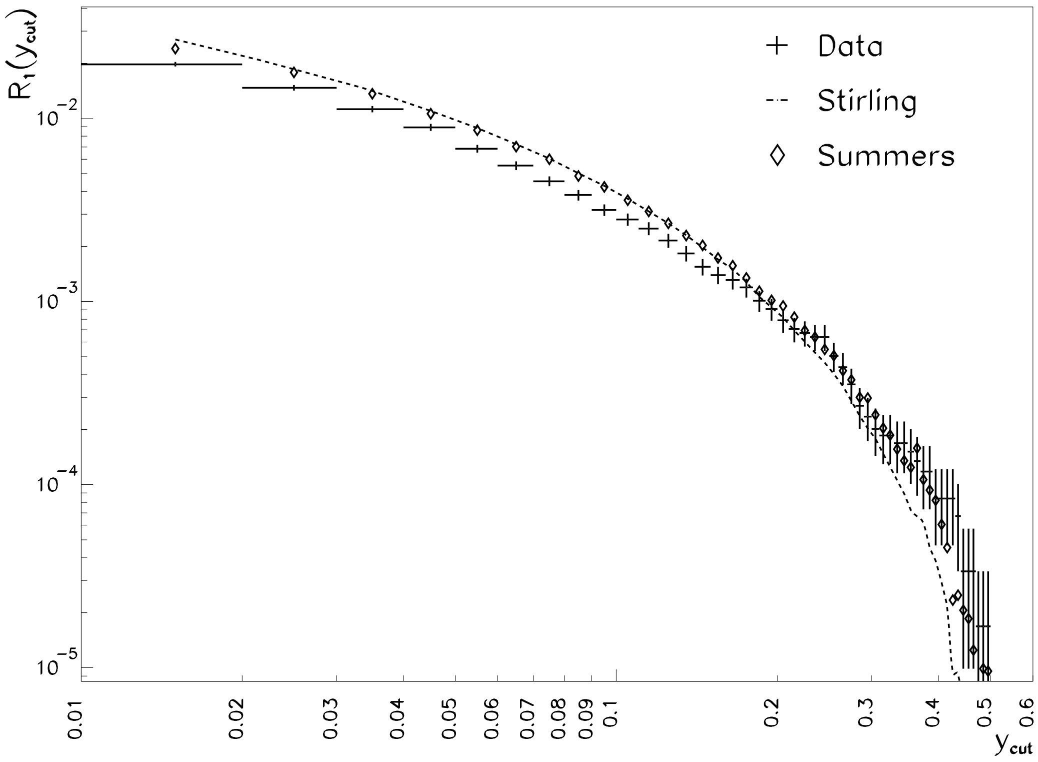

Figure 3.15: A plot of $R_1(y_{cut})$ for data, corrected Stirling and corrected Summers.

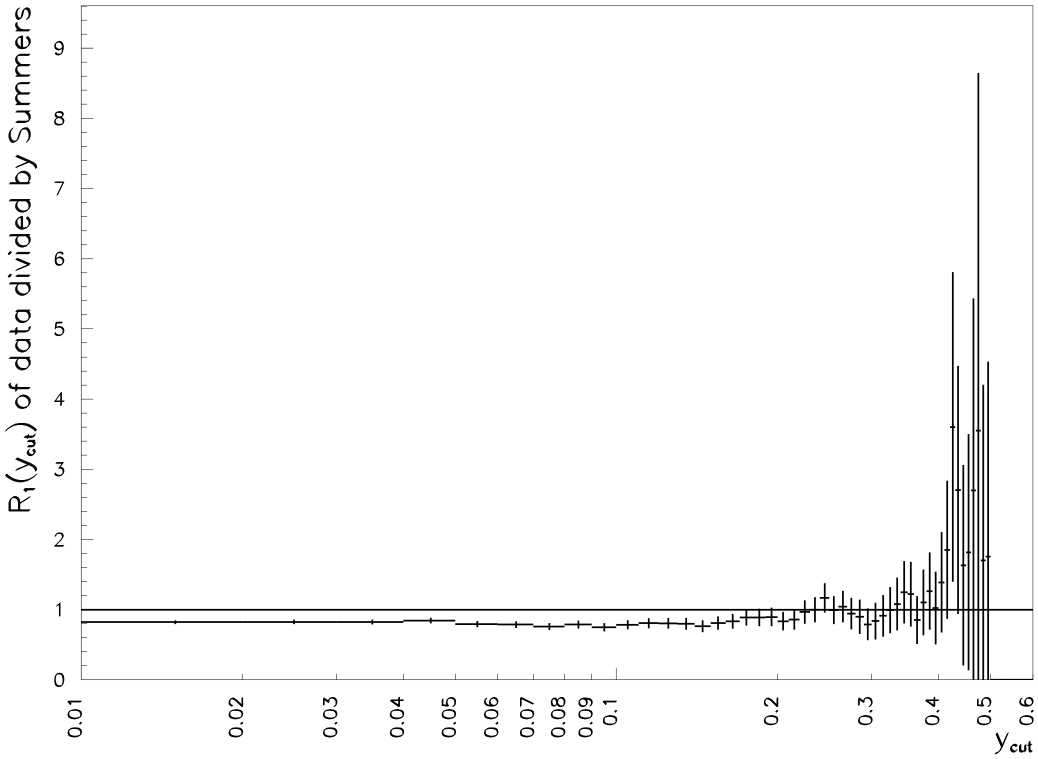

Figure 3.16: A plot of the ratio of $R_1(y_{cut})$ for data and corrected Summers.

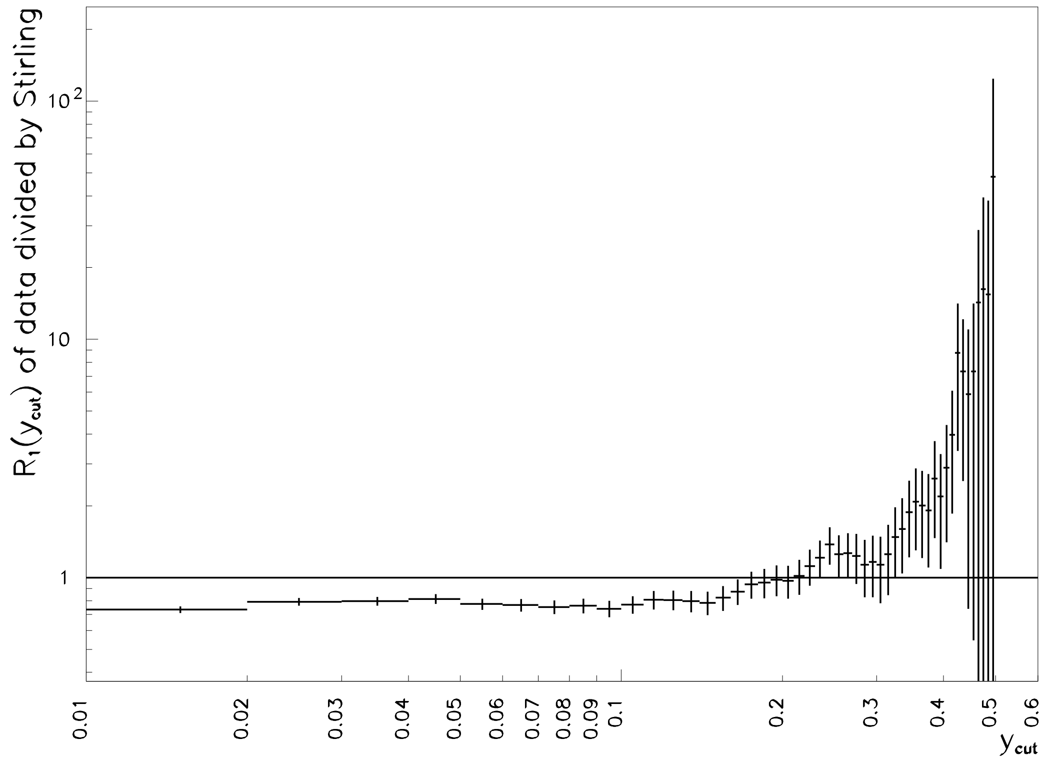

Figure 3.17: A plot of the ratio of $R_1(y_{cut})$ for data and corrected Stirling.

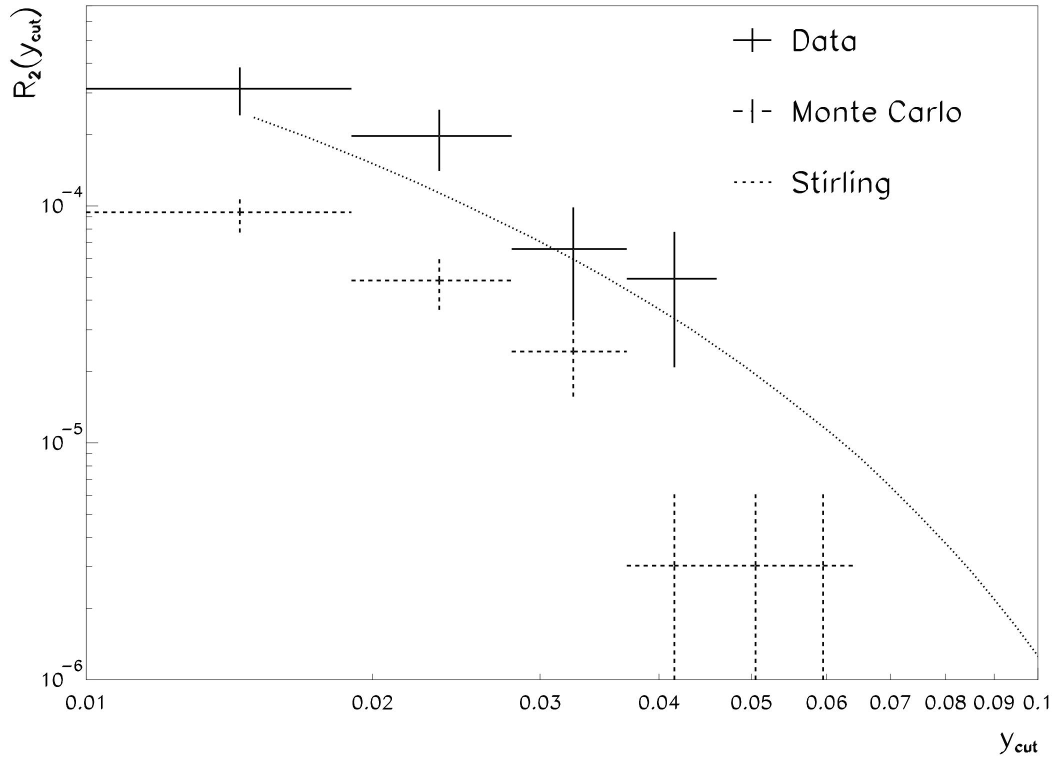

Figure 3.18: A plot of the ratio of $R_2(y_{cut})$ for data, Monte Carlo and Stirling.

3.5 Conclusion

This analysis shows that the number of $\mu^+\mu^- + m\gamma$ $(m \geq 0)$ events in data and Monte Carlo are in good agreement; the data is larger than the Monte Carlo by 2.1 standard deviations. If, however, the number of $\mu^+\mu^- + n\gamma$ $(n \geq 1)$ events in data and Monte Carlo are compared then there is a difference of 5.7 standard deviations. Therefore it is possible to conclude that the Monte Carlo predicts too many events where photons are radiated and too few without photons.

The Monte Carlo used to generate $e^+e^- \to Z \to \mu^+\mu^- + m\gamma$ $(m \geq 0)$ events is not fully second order in α. Thus an excess of $\mu^+\mu^-\gamma$ events in the Monte Carlo is understandable, but if the $\mu^+\mu^-\gamma$ and $\mu^+\mu^-\gamma\gamma$ events are added together the Monte Carlo is still higher than the data. This indicates that the Monte Carlo generates too many $\mu^+\mu^-\gamma$ events even after allowing for the fact that it is not fully second order in α. An analysis of the energy of the photon versus the isolation angle of the photon for such events shows that the Monte Carlo predicts too many events where the photon has a low isolation angle and/or low energy. This effect is not often seen by analyses because it is usually required that for the photons in an event to be considered they must have a reasonably large isolation angle, which removes the problem area of phase space.

The data, however, has more events containing high energy isolated photons. This may be due to the deficiencies of the Monte Carlo, but could also be a sign of new physics. However, given that there is extremely good agreement for the total number of $\mu^+\mu^- + m\gamma$ $(m \geq 0)$ events in data and Monte Carlo, it is unlikely that this data excess is due to new physics, but the possibility can not be ruled out.

The agreement between the theoretical prediction of Summers and data is much better than that between Stirling and data. This suggests that the assumptions made by Stirling, that is that the effects of both initial state radiation and s channel photon exchange can be ignored for centre of mass energies equal to M_Z, are not valid when considering events containing isolated high energy photons. This is because there is a pole in the matrix element for s channel photon exchange when an initial state photon has half the centre of mass energy and the muons are collinear.

Chapter 4

A Monte Carlo for the process $e^+e^- \rightarrow Z \rightarrow \tau^+\tau^-\gamma$

4.1 Introduction

If events originating from a specific interaction are being searched for in data then it is necessary to have Monte Carlo generators for all processes that contribute events to the data sample. Then, after subjecting the events produced by these Monte Carlo generators to detector simulation, it is possible to compare and contrast the distributions of quantities obtained from the detected particles of the different generators and devise a set of cuts which produces a subset of the data sample which contains the relevant events.

The aim of the analysis carried out in Chapter 5 is to constrain the anomalous magnetic moment of the tau. The method employed to achieve this uses the process $e^+e^- \rightarrow Z \rightarrow \tau^+\tau^-\gamma$ where the tau couples to the photon through its magnetic moment. There did not exist a Monte Carlo generator for this process and thus one has been produced. The stages involved in this procedure (i.e. calculation of the matrix element, creating a three body phase space generator and implementing the tau decays) are detailed in this chapter.

4.2 The matrix element

To produce a Monte Carlo generator for a given reaction the appropriate spin averaged matrix element squared, denoted by $\overline{|\mathcal{M}|^2}$, is required. This contains information about both the angular and energy distributions of the final state particles. The calculation of $\overline{|\mathcal{M}|^2}$ for the process $e^+e^- \to Z \to \tau^+\tau^-\gamma$ where the coupling between the tau and the photon is due to the tau's magnetic moment has never been published, and therefore it was necessary to perform this calculation within the framework of the standard model.

There are four Feynman diagrams for the process $e^+e^- \to Z \to \tau^+\tau^-\gamma$, as any of the external charged fermions can radiate the photon. These diagrams are illustrated in fig. 4.1. The couplings between the fields which are required to convert the diagrams into matrix elements are shown in fig. 4.2. The form and origin of the coupling used between the tau and the photon is explained in section 1.5, but it is important to note that $F_2(0)$ is the Pauli form factor that is used to represent the anomalous magnetic moment of the tau when it couples to a zero mass photon.

The matrix elements for diagrams 1, 2, 3 and 4 of fig. 4.1 are

$$\begin{aligned}
\mathcal{M}_1 &= \bar{v}(p_+)\left(\frac{-ig}{\cos\theta_W}\gamma^\nu\frac{1}{2}(c_V^e - c_A^e\gamma^5)\right)\times \\
&\quad i\frac{(\not{p}_- - \not{k})}{(p_- - k)^2}\epsilon_\delta^*(-ie\gamma^\delta)u(p_-)\left(\frac{-ig_{\nu\mu}}{R}\right)\times \\
&\quad \bar{u}(q_-)\left(\frac{-ig}{\cos\theta_W}\gamma^\mu\frac{1}{2}(c_V^\tau - c_A^\tau\gamma^5)\right)v(q_+)
\end{aligned}$$

$$\begin{aligned}
\mathcal{M}_2 &= \bar{v}(p_+)\epsilon_\delta^*(-ie\gamma^\delta)i\frac{(-\not{p}_+ + \not{k})}{(-p_+ + k)^2}\times \\
&\quad \left(\frac{-ig}{\cos\theta_W}\gamma^\nu\frac{1}{2}(c_V^e - c_A^e\gamma^5)\right)u(p_-)\left(\frac{-ig_{\nu\mu}}{R}\right)\times \\
&\quad \bar{u}(q_-)\left(\frac{-ig}{\cos\theta_W}\gamma^\mu\frac{1}{2}(c_V^\tau - c_A^\tau\gamma^5)\right)v(q_+)
\end{aligned}$$

$$\begin{aligned}
\mathcal{M}_3 &= \bar{v}(p_+)\left(\frac{-ig}{\cos\theta_W}\gamma^\nu\frac{1}{2}(c_V^e - c_A^e\gamma^5)\right)u(p_-)\left(\frac{-ig_{\nu\mu}}{R}\right)\times \\
&\quad \bar{u}(q_-)\epsilon_\delta^*\left\{-ie\left(\gamma^\delta + i\frac{F_2(0)}{2M_\tau}\sigma_{\delta\rho}k_\rho\right)\right\} i\frac{(\not{q}_- + \not{k})}{(q_- + k)^2}\times \\
&\quad \left(\frac{-ig}{\cos\theta_W}\gamma^\mu\frac{1}{2}(c_V^\tau - c_A^\tau\gamma^5)\right)v(q_+) \\
\mathcal{M}_4 &= \bar{v}(p_+)\left(\frac{-ig}{\cos\theta_W}\gamma^\nu\frac{1}{2}(c_V^e - c_A^e\gamma^5)\right)u(p_-)\left(\frac{-ig_{\nu\mu}}{R}\right)\times \\
&\quad \bar{u}(q_-)\left(\frac{-ig}{\cos\theta_W}\gamma^\mu\frac{1}{2}(c_V^\tau - c_A^\tau\gamma^5)\right) i\frac{(-\not{q}_+ - \not{k})}{(-q_+ - k)^2}\epsilon_\delta^*\times \\
&\quad \left\{-ie\left(\gamma^\delta + i\frac{F_2(0)}{2M_\tau}\sigma_{\delta\rho}k_\rho\right)\right\} v(q_+)
\end{aligned}$$

where

$$R = \frac{1}{(p_+ + p_-)^2 - M_Z^2 + iM_Z\Gamma_Z}$$

and p_+, p_-, q_+, q_- and k are the four-momenta of the positron, electron, positive tau, negative tau and photon respectively. The masses of the external fermions have been assumed to be zero compared to the centre of mass energy.

The total matrix element, $\mathcal{M}_{\rm TOT}$, is the sum of the matrix elements obtained from the four Feynman diagrams, i.e.

$$\mathcal{M}_{\rm TOT} = \mathcal{M}_1 + \mathcal{M}_2 + \mathcal{M}_3 + \mathcal{M}_4$$

and therefore the spin averaged matrix element squared is

$$\begin{aligned}
\overline{|\mathcal{M}_{\rm TOT}|^2} &= \overline{|\mathcal{M}_1|^2} + \overline{|\mathcal{M}_2|^2} + \overline{|\mathcal{M}_3|^2} + \overline{|\mathcal{M}_4|^2} + \\
&\quad 2{\rm Re}\left(\overline{\mathcal{M}_1\mathcal{M}_2^\dagger} + \overline{\mathcal{M}_1\mathcal{M}_3^\dagger} + \overline{\mathcal{M}_1\mathcal{M}_4^\dagger}\right. \\
&\quad \left. + \overline{\mathcal{M}_2\mathcal{M}_3^\dagger} + \overline{\mathcal{M}_2\mathcal{M}_4^\dagger} + \overline{\mathcal{M}_3\mathcal{M}_4^\dagger}\right). \qquad (4.1)
\end{aligned}$$

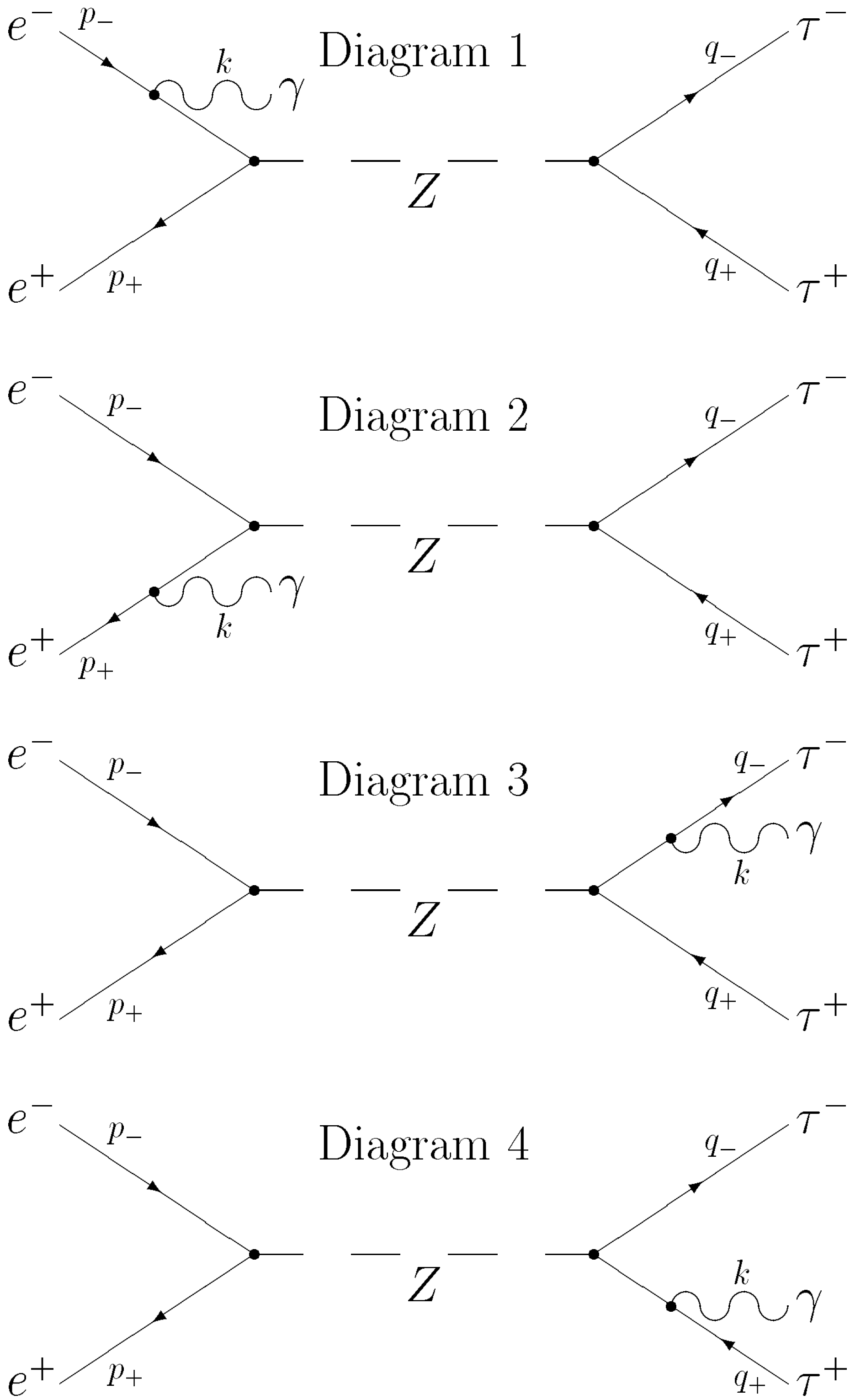

Figure 4.1: The Feynman diagrams used to calculate the matrix element.

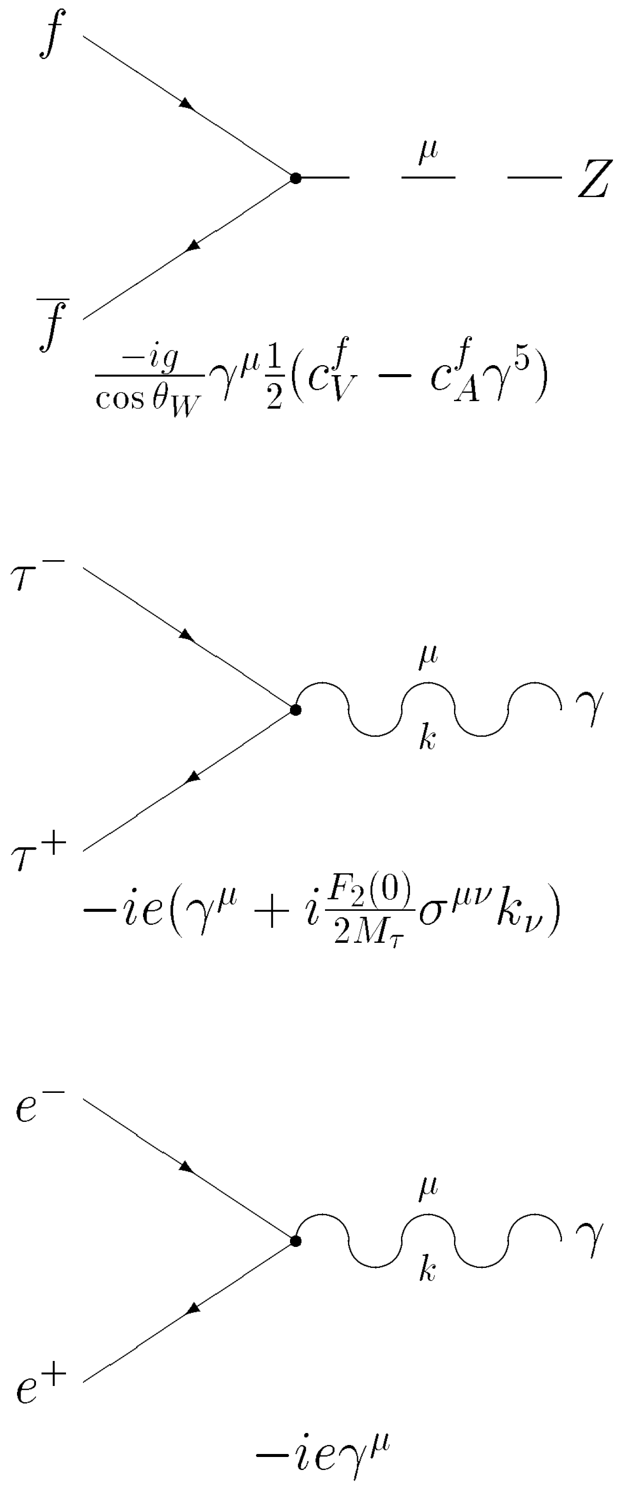

Figure 4.2: The couplings used in the calculation of the matrix element.

The initial stage in calculating an element of equation 4.1 is to derive the hermitian conjugate of the appropriate matrix element, and thus construct the required matrix element squared or interference term. Next the spins of the initial state particles are averaged whilst those of the final state particles are summed. This produces an expression that is a collection of trace operations. The results given in appendix A are used to simplify these traces and provide the final results which are expressed in terms of the four-momenta of the participating particles.

The Pauli form factor $F_2(0)$ is not present in the three terms of equation 4.1 which are constructed from the matrix elements obtained when the photon is radiated from an initial state particle. Therefore these terms ($\overline{|\mathcal{M}_1|^2}$, $\overline{|\mathcal{M}_2|^2}$ and $\overline{\mathcal{M}_1\mathcal{M}_2^\dagger}$) do not have to be explicitly calculated as they will not contribute to the cross-section for the magnetic coupling and a Monte Carlo generator already exists for the case when there is a non-magnetic tau-photon coupling.

Both the magnetic and non-magnetic tau-photon couplings are included in the vertex term which was used to obtain $\mathcal{M}_3$ and $\mathcal{M}_4$. There is no interference between these two couplings when $\overline{|\mathcal{M}_3|^2}$ and $\overline{|\mathcal{M}_4|^2}$ are calculated as the terms which are linear in $F_2(0)$ are all identically zero. This is explicitly shown below for $\overline{|\mathcal{M}_3|^2}$.

The first stage in calculating $\overline{|\mathcal{M}_3|^2}$ is to obtain the matrix element squared, which is

$$\begin{aligned}
\mathcal{M}_3\mathcal{M}_3^\dagger \quad = \quad & \frac{e^2 g^4 \epsilon_\delta^* \epsilon_\sigma}{64(q_- \cdot k)^2 \cos^4\theta_W RR^*}\bar{v}(p_+)\gamma^\nu(c_V^e - c_A^e\gamma^5)u(p_-)\bar{u}(p_-)\times \\
& \gamma^\eta(c_V^e - c_A^e\gamma^5)v(p^+)\bar{u}(q_-)\left\{\gamma^\delta - \frac{F_2(0)}{4M_\tau}(\gamma^\delta \not{k} - \not{k}\gamma^\delta)\right\}\times \\
& (\not{q}_- + \not{k})\gamma_\nu(c_V^\tau - c_A^\tau\gamma^5)v(q_+)\bar{v}(q_+)\gamma_\eta(c_V^\tau - c_A^\tau\gamma^5)\times \\
& (\not{q}_- + \not{k})\left\{\gamma^\sigma - \frac{F_2(0)}{4M_\tau}(\not{k}\gamma^\sigma - \gamma^\sigma \not{k})\right\}u(q_-).
\end{aligned}$$

Averaging the spins of the initial state particles and summing the spins of the final state particles gives

$$\overline{|\mathcal{M}_3|^2} = \frac{-e^2 g^4}{256(q_- \cdot k)^2 \cos^4\theta_W RR^*} \times$$

$$\left\{({c_V^e}^2 + {c_A^e}^2) Tr\left[\not p_+ \gamma^\nu \not p_- \gamma^\eta\right] - 2c_V^e c_A^e Tr\left[\gamma^5 \not p_+ \gamma^\nu \not p_- \gamma^\eta\right]\right\} \times$$

$$\left\{({c_V^\tau}^2 + {c_A^\tau}^2) Tr\left[\not q_- \gamma^\delta (\not q_- + \not k)\gamma_\nu \not q_+ \gamma_\eta (\not q_- + \not k)\gamma_\delta\right] - \tag{4.2}$$

$$2c_V^\tau c_A^\tau Tr\left[\gamma^5 \not q_- \gamma^\delta (\not q_- + \not k)\gamma_\nu \not q_+ \gamma_\eta (\not q_- + \not k)\gamma_\delta\right] - \tag{4.3}$$

$$({c_V^\tau}^2 + {c_A^\tau}^2)\frac{F_2(0)}{4M_\tau} Tr\left[\not q_- (\gamma^\delta \not k - \not k \gamma^\delta)(\not q_- + \not k)\gamma_\nu \not q_+ \gamma_\eta \times (\not q_- + \not k)\gamma_\delta\right] + \tag{4.4}$$

$$2c_V^\tau c_A^\tau \frac{F_2(0)}{4M_\tau} Tr\left[\gamma^5 \not q_- (\gamma^\delta \not k - \not k \gamma^\delta)(\not q_- + \not k)\gamma_\nu \not q_+ \gamma_\eta \times (\not q_- + \not k)\gamma_\delta\right] - \tag{4.5}$$

$$({c_V^\tau}^2 + {c_A^\tau}^2)\frac{F_2(0)}{4M_\tau} Tr\left[\not q_- \gamma^\delta (\not q_- + \not k)\gamma_\nu \not q_+ \gamma_\eta (\not q_- + \not k) \times (\not k \gamma_\delta - \gamma_\delta \not k)\right] - \tag{4.6}$$

$$2c_V^\tau c_A^\tau \frac{F_2(0)}{4M_\tau} Tr\left[\gamma^5 \not q_- \gamma^\delta (\not q_- + \not k)\gamma_\nu \not q_+ \gamma_\eta (\not q_- + \not k) \times (\not k \gamma_\delta - \gamma_\delta \not k)\right] + \tag{4.7}$$

$$({c_V^\tau}^2 + {c_A^\tau}^2)\frac{F_2^2(0)}{16M_\tau^2} Tr\left[\not q_- (\gamma^\delta \not k - \not k \gamma^\delta)(\not q_- + \not k)\gamma_\nu \not q_+ \gamma_\eta \times (\not q_- + \not k)(\not k \gamma_\delta - \gamma_\delta \not k)\right] + \tag{4.8}$$

$$2c_V^\tau c_A^\tau \frac{F_2^2(0)}{16M_\tau^2} Tr\left[\gamma^5 \not q_- (\gamma^\delta \not k - \not k \gamma^\delta)(\not q_- + \not k)\gamma_\nu \not q_+ \gamma_\eta (\not q_- + \not k) \times (\not k \gamma_\delta - \gamma_\delta \not k)\right]\} . \tag{4.9}$$

The terms 4.2 and 4.3 in the above equation are due to the non-magnetic coupling and thus do not include $F_2(0)$. Terms 4.4 to 4.7 are due to the interference between the two types of tau-photon coupling and are all identically zero. This is because they all contain the trace of either an odd number of gamma matrices or γ^5 multiplied by an odd number of gamma matrices (appendix A). The last two terms (4.8 and 4.9) are due to the magnetic coupling and are the only non-zero terms containing $F_2(0)$. Thus there is no interference between the magnetic and non-magnetic tau-photon couplings.

The absence of interference between the different tau-photon couplings is because the magnetic coupling is due to a dipole which therefore flips the helicity of the fermion line. Thus the helicity configuration of the final state particles when there is a dipole coupling is different from the configuration when there is a non-magnetic coupling, making interference impossible [42] [43]. The same is true for $\overline{|\mathcal{M}_4|^2}$, where, again, there are no terms linear in $F_2(0)$.

All of the interference terms which contain $\mathcal{M}_1$ or $\mathcal{M}_2$ and $\mathcal{M}_3$ or $\mathcal{M}_4$ do not have any non-zero contribution with $F_2(0)$ as a factor. All the non-zero elements of these terms are due to the non-magnetic coupling between the tau and the photon. To illustrate this consider the interference between $\mathcal{M}_1$ and $\mathcal{M}_3$, which is given by

$$
\begin{aligned}
\overline{\mathcal{M}_1\mathcal{M}_3^\dagger} \; = \; & \frac{-e^2 g^4}{256(p_- \cdot k)(q_- \cdot k)\cos^4\theta_W R R^*} \times \\
& \left\{({c_V^e}^2 + {c_A^e}^2) Tr\left[\not{p}_+ \gamma^\nu (\not{p}_- - \not{k})\gamma^\delta \not{p}_- \gamma^\eta\right] - \right. \\
& \left. 2 c_V^e c_A^e Tr\left[\gamma^5 \not{p}_+ \gamma^\nu (\not{p}_- - \not{k})\gamma^\delta \not{p}_- \gamma^\eta\right]\right\} \times \\
& \left\{({c_V^\tau}^2 + {c_A^\tau}^2) Tr\left[\not{q}_- \gamma_\nu \not{q}_+ \gamma_\eta (\not{q}_- + \not{k})\gamma_\delta\right] - \right. && (4.10) \\
& 2 c_V^\tau c_A^\tau Tr\left[\gamma^5 \not{q}_- \gamma_\nu \not{q}_+ \gamma_\eta (\not{q}_- + \not{k})\gamma_\delta\right] - && (4.11) \\
& ({c_V^\tau}^2 + {c_A^\tau}^2)\frac{F_2(0)}{4M_\tau} Tr\left[\not{q}_- \gamma_\nu \not{q}_+ \gamma_\eta (\not{q}_- + \not{k})(\not{k}\gamma_\delta - \gamma_\delta \not{k})\right] + && (4.12)
\end{aligned}
$$

$$2c_V^\tau c_A^\tau \frac{F_2(0)}{4M_\tau}\, Tr\left[\gamma^5 \not{q}_- \gamma_\nu \not{q}_+ \gamma_\eta (\not{q}_- + \not{k})(\not{k}\gamma_\delta - \gamma_\delta \not{k})\right]\Big\} \qquad (4.13)$$

In the above equation the terms 4.10 and 4.11 are due to the non-magnetic coupling and therefore do not contain $F_2(0)$. The last two terms (4.12 and 4.13) are where there is interference between the magnetic and non-magnetic tau-photon couplings, and both are identically zero due to the odd number of gamma matrices (appendix A). Therefore the only interference term which contains a non-zero element with the Pauli magnetic coupling factor is $\overline{\mathcal{M}_3\mathcal{M}_4^\dagger}$.

Calculating all of the terms in equation 4.1 leads to

$$\begin{aligned}
\overline{|\mathcal{M}_{\mathrm{TOT}}|^2} \;=\; & \overline{|\mathcal{M}_0|^2} + \frac{2e^2 g^4 F_2(0)^2}{M_\tau^2 \cos^4\theta_W RR^*} \times \\
& \Big\{ (c_V^2 + c_A^2)^2 \left[(p_+ \cdot q_+)(p_- \cdot q_-) + (p_+ \cdot q_-)(p_- \cdot q_+)\right] + \\
& 4c_V^2 c_A^2 \left[(p_+ \cdot q_+)(p_- \cdot q_-) + (p_+ \cdot q_-)(p_- \cdot q_+)\right] - \\
& \frac{(c_V^4 - c_A^4)}{(q_+ \cdot k)(q_- \cdot k)} \Big[(p_+ \cdot q_+)(p_- \cdot q_+)(q_- \cdot k)^2 + \\
& (p_+ \cdot k)(p_- \cdot k)(q_+ \cdot q_-)^2 + (p_+ \cdot q_-)(p_- \cdot q_-)(q_+ \cdot k)^2 - \\
& (p_+ \cdot q_+)(p_- \cdot k)(q_+ \cdot q_-)(q_- \cdot k) - \\
& (p_+ \cdot k)(p_- \cdot q_+)(q_+ \cdot q_-)(q_- \cdot k) - \\
& (p_+ \cdot q_-)(p_- \cdot k)(q_+ \cdot q_-)(q_+ \cdot k) - \\
& (p_+ \cdot k)(p_- \cdot q_-)(q_+ \cdot q_-)(q_+ \cdot k)\Big]\Big\} \qquad (4.14)
\end{aligned}$$

where $\overline{|\mathcal{M}_0|^2}$ is the result obtained for the non-magnetic tau-photon coupling, and the universality of the couplings between the Z and all three generations of leptons has been used to give $c_V^e = c_V^\tau = c_V$ and $c_A^e = c_A^\tau = c_A$. To produce a Monte Carlo generator for the magnetic tau-photon coupling the terms without $F_2(0)$ as a factor, which are all contained in $\overline{|\mathcal{M}_0|^2}$, are not required.

The Feynman diagrams with an exchanged photon, rather than a Z, have not been considered because of the lack of interference between the magnetic and non-magnetic tau-photon couplings. This means that all non-zero terms containing $F_2(0)$ that would be created by including photon exchange are either T or $\sqrt{T}$ smaller than the terms in equation 4.14, where T is given by

$$T = \frac{\left((p_+ + p_-)^2 - M_Z^2\right)^2 + M_Z^2\Gamma_Z^2}{(p_+ + p_-)^4}. \tag{4.15}$$

The data used for the analysis in Chapter 5 has $(p_+ + p_-)^2 = M_Z^2$, which means that $T = \Gamma_Z^2/M_Z^2 \sim 0.003$. Thus it is valid to ignore the contribution from photon exchange.

Once $\overline{|\mathcal{M}|^2}$ has been calculated then the cross-section can be obtained using

$$\sigma = \frac{1}{2s(2\pi)^5}\int \frac{d^3q_+}{2q_{+0}}\frac{d^3q_-}{2q_{-0}}\frac{d^3k}{2k_0}\,\delta^{(4)}\left((p_+ + p_-) - (q_+ + q_- + k)\right)\overline{|\mathcal{M}|^2}. \tag{4.16}$$

Thus by substituting $c_V = -1/2 + 2\sin^2\theta_W$ and $c_A = -1/2$ into equation 4.14 and using the values of constants given by the particle data group [44] it is possible to obtain a cross-section where the only unknown quantity is $F_2(0)$. This result has been compared to the one obtained by Grifols and Méndez [45], where the width $Z \to \tau^+\tau^-\gamma$ for the magnetic tau-photon coupling was calculated and the cross-section obtained using

$$\sigma(e^+e^- \to Z \to X)|_{\sqrt{s}=M_z} = \frac{12\pi}{M_Z^2}\frac{\Gamma_{e^+e^-}\Gamma_X}{\Gamma_Z^2}. \tag{4.17}$$

The two results agree to three significant figures.

4.3 A three body phase space generator

By using Monte Carlo integration to evaluate equation 4.16 it is possible to obtain an event generator for a process where $\overline{|\mathcal{M}|^2}$ is known. A phase space generator is usually employed to carry out the integration. These generators cover all of the phase space available for the process, once four-momentum conservation and the masses of the final state particles have been taken into account, and select a random choice of four-momenta for the final state particles, thus creating an event. A weight is assigned to this event which is a measure of the probability of this geometric configuration of particles occuring for the given process. If the maximum achievable weight is known then it is possible, by using a random number generator, to obtain unweighted events.

For three body phase space it is possible to express all the four-momenta in terms of five independent variables. To illustrate this, and show the variables which are required, consider the decay $X \rightarrow A + B + C$, where the particles have masses M_X, M_A, M_B and M_C respectively. This decay can be viewed as consisting of three consecutive stages - the decay $X \rightarrow A + D$ in the lab frame, the decay $D \rightarrow B + C$ in the rest frame of the D, and the boosting of the decay products of the D into the lab frame. These processes are shown schematically in fig. 4.3.

The first decay, $X \rightarrow A + D$, requires three of the five independent variables. The mass of the D is one of those required, as it can vary between bounds obtained by the following kinematic constraints. The total energy after the decay can not exceed the rest mass energy of the X and therefore the upper limit $M_D \leq M_X - M_A$ is necessary. The lower limit of $M_D \geq M_B + M_C$ is required so that the D decay is energetically allowed. Momentum conservation must be applied for each different M_D to ensure that $\underline{p}_A = -\underline{p}_D$. The other two variables necessary for the decay to cover all of the available phase space are the polar angle θ and the azimuthal angle ϕ, which are used to determine the spatial positions of the A and the D. These have the usual ranges of $0 \leq \theta \leq \pi$ and $0 \leq \phi \leq 2\pi$.

The other two variables are needed for the second decay. Here the masses of the decay products are fixed and thus the only variables are the angles required to calculate the directions of the B and the C in the rest frame of the D. Once again there is a polar angle, θ', and an azimuthal angle, ϕ', which have the ranges $0 \leq \theta' \leq \pi$ and $0 \leq \phi' \leq 2\pi$.

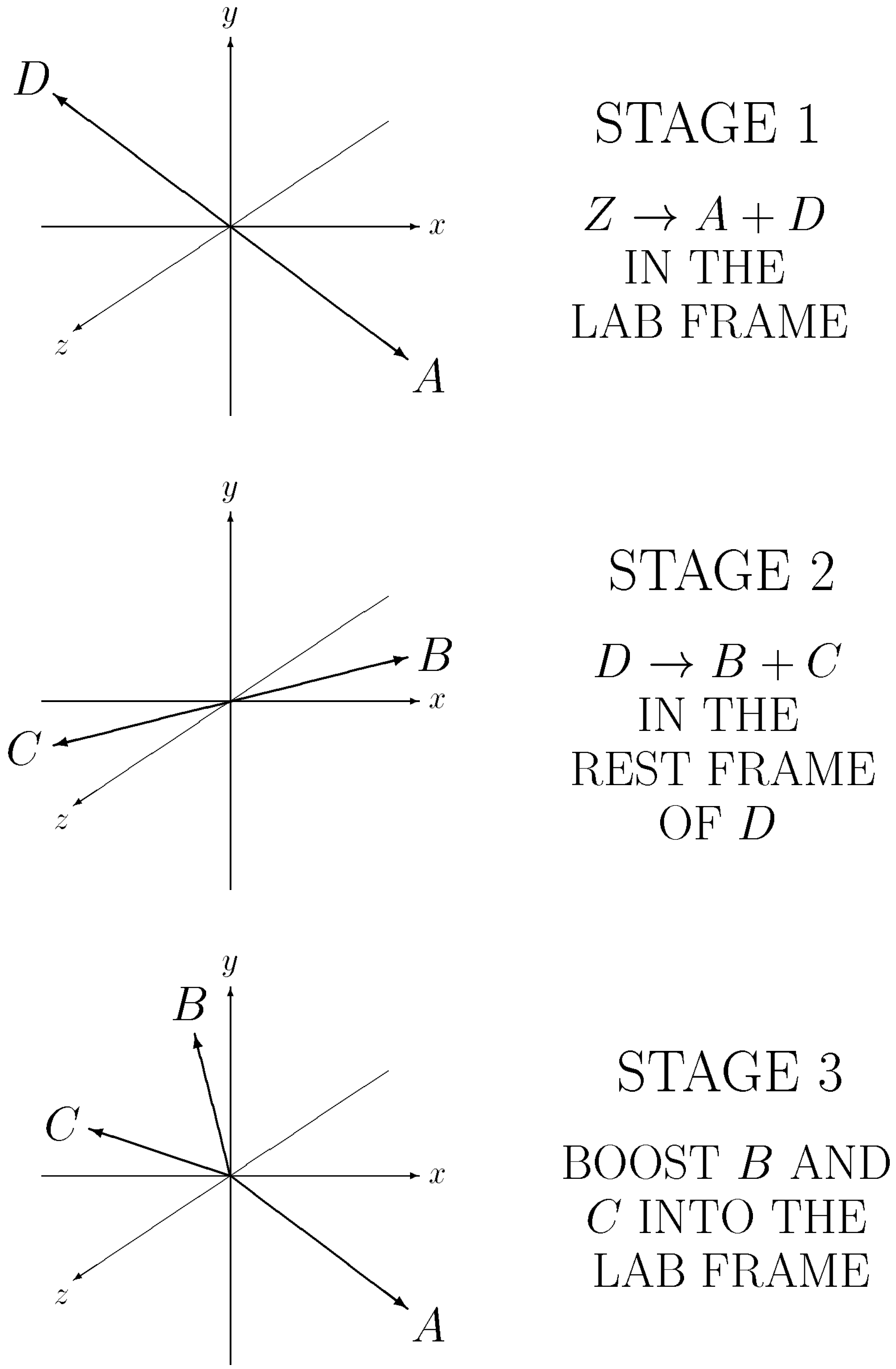

Figure 4.3: A schematic explanation of three body phase space.

Following the boost applied to B and C, the production of three random four-momenta whose sum is $(M_X, \underline{0})$ is complete. Therefore by using $M_X = M_Z$, $M_A = M_B = M_\tau$ and $M_C = 0$ it is possible to obtain randomly varying four-momenta for the particles resulting from the decay $Z \to \tau^+\tau^-\gamma$.

A formula to calculate the event weight is provided by rewriting equation 4.16 in the form [46]

$$\sigma = \frac{1}{2s(2\pi)^5} \int_{M_D=M_\tau}^{M_D=M_Z-M_\tau} \int W \, d\Omega \, d\Omega' dM_D$$

where

$$W = 2M_D \frac{\lambda^{\frac{1}{2}}(M_Z^2, M_\tau^2, M_D^2)}{8M_Z^2} \frac{\lambda^{\frac{1}{2}}(M_D^2, M_\tau^2, 0)}{8M_D^2} \overline{|\mathcal{M}|^2} \tag{4.18}$$

$$d\Omega = d\cos\theta \, d\phi, \quad d\Omega' = d\cos\theta' d\phi'$$

$$\lambda(a,b,c) = a^2 + b^2 + c^2 - 2(ab + ac + bc).$$

Thus the calculation of equation 4.18 for each random selection of four-momenta by the phase space generator provides the required event weight. If the maximum value W can attain is known then the hit and miss method [41] can be employed to produce unweighted events. Using this method an event is only kept if

$$\frac{W}{W_{max}} > R$$

where R is chosen randomly between 0 and 1.

The above procedures have been implemented to create a Monte Carlo generator that produces unweighted events for the reaction $e^+e^- \to Z \to \tau^+\tau^-\gamma$ with a magnetic tau-photon coupling.

There is a dichotomy in the Monte Carlo as the tau mass is assumed to be zero for the matrix element calculation but its correct value is used in the phase space generator. This is resolved by considering the following argument. Reinstating the tau mass in the matrix element calculation gives rise to terms which are typically a factor $M_\tau/M_Z \sim 0.02$ smaller than those already present [47] and therefore it is valid to neglect it, whereas it is essential for correct detector simulation that the tau mass is correct when the four-momenta of the event are generated.

The weighted energies of the particles generated by the phase space generator are shown in fig. 4.4. The weighting that has been used is the phase space part of equation 4.18, i.e. equation 4.18 / $\overline{|\mathcal{M}|^2}$. The distributions of the particles is identical if the tau mass is taken into account.

The plot in fig. 4.5 shows the photon energy spectrum from the Monte Carlo where the form factor $F_2(0)$ has been set to one. The spectrum from the Monte Carlo which is used by ALEPH to produce a $\tau^+\tau^-\gamma$ final state is also included to illustrate the difference which arises when the magnetic coupling is used.

4.4 Implementing the τ decays

The short lifetime of the tau means that their decays must be carried out by the Monte Carlo generator before the event is passed onto detector simulation. The machinery required to implement these decays correctly is large and complicated and therefore an existing program was modified and added to the above Monte Carlo.

The Monte Carlo generator KORALZ [33] [34] [35] is used by all the LEP experiments to simulate the decay $e^+e^- \to Z \to \tau^+\tau^- + n\gamma$, $n = 0, 1, 2, 3$, and implements most tau decay modes with branching ratios which will be acheived by LEP. Therefore the relevant sections of KORALZ were used to decay the taus produced by the Monte Carlo generator with the magnetic coupling. The events which are generated can now be subjected to detector simulation and used in the analysis conducted in Chapter 5.

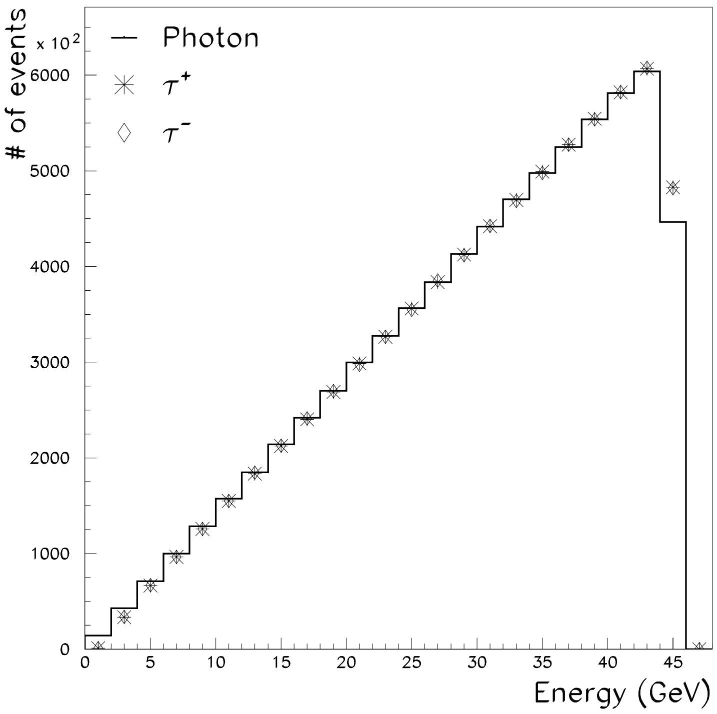

Figure 4.4: The weighted particle energies from the phase space generator.

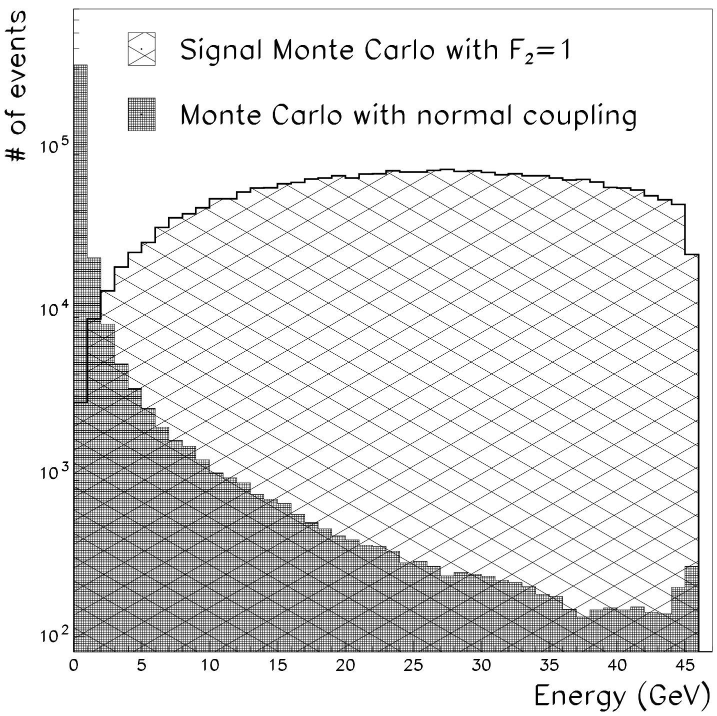

Figure 4.5: The photon energy spectra from Monte Carlo generators with magnetic and non-magnetic tau-photon couplings.

Chapter 5

Constraining the anomalous magnetic moment of the tau

5.1 Introduction

Accurate experimental measurements of the intrinsic parameters of the leptons provide a window to study the subtle effects that higher order corrections have on the physically observable quantities of the standard model (section 1.4). The intrinsic parameters of the quark sector do not generally provide such accurate tests of higher order effects because the asymptotic freedom present in QCD makes obtaining accurate experimental results difficult.

Given that the tau was the last charged lepton to be experimentally discovered [48] along with the fact that of all three charged leptons it has the shortest lifetime, it is possible to understand why most of its intrinsic parameters have not been as accurately measured as those of the electron and muon. An illustrative example is afforded by considering the experimental accuracy obtained in measuring the anomalous magnetic moments of the three charged leptons.

A detailed explanation of the origin of the magnetic moments of the charged fermions, and how they acquire anomalous magnetic moments within the framework of the standard model, can be found in section 1.5. It is shown in this section that the coupling between a fermion of flavour f and a photon caused by the anomalous magnetic moment of the fermion f is proportional to the Pauli form factor $F_2^f(k^2)$, where k^μ is the four-momentum of the photon. The anomalous magnetic moment of the fermion is identified as being equal to $F_2^f(0)$.

If the effects of higher order corrections are excluded then the anomalous magnetic moments of all three charged leptons is equal to zero (section 1.5). This value changes, however, with the inclusion of radiative corrections, and this effect is dependent on the mass of the lepton. This means that all three leptons have different anomalous magnetic moments.

Whilst the anomalous magnetic moment of the electron has been measured to ten significant figures and that of the muon to eight significant figures, the value of the anomalous magnetic moment of the tau is only constrained [49].

It is possible for some compositeness models to greatly enhance the standard model prediction for the anomalous magnetic moment of the tau [50], and as such enhanced values have not yet been excluded by experiment, it is possible that the tau is a composite object. Therefore it is the aim of this chapter to constrain further the range of values available for the anomalous magnetic moment of the tau, with the possibility of observing an indication of compositeness.

This analysis produces a limit for $F_2^\tau(0)$ by comparing the geometric characteristics of events with a $\tau^+\tau^-\gamma$ final state in the ALEPH data with those predicted by a Monte Carlo generator which has a coupling between the taus and the photon that is entirely due to the anomalous magnetic moment of the tau.

5.2 Data selection

The aim of this chapter is to constrain the anomalous magnetic moment of the tau by analysing how it couples to a real photon. Therefore a series of cuts are required which will produce a subset of the ALEPH data that contains events with a $\tau^+\tau^-\gamma$ final state. It is, however, only possible for ALEPH to detect the decay products of the taus. This makes identifying the required final state a complicated process, and a high purity is hard to obtain if the efficiency of the selection process is to be kept at a reasonable level.

The proportion of tau decays producing one and three charged particles, along with n neutral particles ($n \geq 0$), is approximately 85% and 14% respectively [49]. Therefore greater than 99% of $\tau^+\tau^-\gamma$ final states have two, four or six charged tracks detected. For this analysis only events where the taus decay to two or four tracks are searched for. Such configurations constitute over 97% of the total allowed final states. Events where the taus produce six charged tracks are not included in the analysis in order to reduce the background from $Z \to q\bar{q}'$ [23]. Therefore only events with a final state topology of two or four charged tracks and one photon are required for this analysis.

The subset of ALEPH data produced by this topological selection will include events from radiative Bhabha events, $Z \to \mu^+\mu^-\gamma$ decays, gamma-gamma annihilations and $Z \to q\bar{q}'$ in addition to the required $Z \to \tau^+\tau^-\gamma$ events. Therefore the second stage of the data selection process is to remove the majority of these background events so that the final subset of data from which the limit is extracted consists mainly of $Z \to \tau^+\tau^-\gamma$ events.

The data used for this analysis consists of events collected by ALEPH in 1990, 1991, 1992 and 1993. Only events where LEP was running exactly on the peak, that is $\sqrt{s} = M_Z$, are used, leaving a sample of 48.8 pb^{-1}.

Data collected whilst LEP was running below the Z peak are not used because for such centre of mass energies s channel photon exchange is important, and the matrix element of the signal Monte Carlo (see next section) does not include Feynman diagrams where a photon is exchanged in the s channel.

The reason for not using ALEPH data collected whilst LEP was running above the Z peak is because at such energies it is quite likely that a photon will be radiated from one of the initial state particles, leaving a centre of mass energy for the electron-positron annihilation which is equal to the rest mass energy of the Z boson. The increased likelihood of initial state radiation can cause a problem because if a non-tau event contains an initial state photon that is not detected because it has a small polar angle along with two or four tracks and a photon which are detected, the event is likely to be misidentified as a $Z \to \tau^+\tau^-\gamma$ decay. This is because the sum of detected energy for such an event is less than the centre of mass energy due to the undetected photon, and missing energy is the signature of a $Z \to \tau^+\tau^-\gamma$ decay.

5.2.1 The signal Monte Carlo generator

Whilst the data selection process produces a set of events consisting mainly of $Z \to \tau^+\tau^-\gamma$ decays, the average geometry of these events is quite different for the instances where the tau-photon coupling is due to the tau's anomalous magnetic moment rather than its electric charge [45]. Given that it is the analysis of the former type of tau-photon coupling which will constrain the Pauli form factor $F_2^\tau(0)$, it is necessary to develop geometric cuts which will enhance the number of events in the final data sample with an anomalous tau-photon coupling. This process requires having Monte Carlo generators for both types of tau-photon coupling. Events from both generators are also required to obtain a limit for $F_2^\tau(0)$ by ascertaining how many of the events in the final data sample have been caused by the anomalous magnetic moment of the tau.

None of the Monte Carlo generators which are used to simulate the decay $Z \to \tau^+\tau^-\gamma$ include the possibility of having the tau-photon coupling being due to the anomalous magnetic moment of the tau. For this reason the writing of a generator to simulate the reaction $e^+e^- \to Z \to \tau^+\tau^-\gamma$, where the tau-photon coupling is entirely due to the anomalous magnetic moment of the tau, was undertaken. An explanation of the stages involved in this process is given in chapter 4.

Therefore there are two separate Monte Carlo generators used in this analysis to simulate the decay $Z \to \tau^+\tau^-\gamma$. In one the tau-photon coupling only occurs because of the electric charge of the tau (the tau background Monte Carlo), whilst in the other the tau-photon coupling is entirely due to the anomalous magnetic moment of the tau (the signal Monte Carlo).

To extract a limit for $F_2^\tau(0)$ it is necessary to normalise the integrated luminosity of the set of events generated using the signal Monte Carlo to that of the data sample. The method employed to obtain a normalisation factor for a set of Monte Carlo events is explained in section 3.3.1.

The set of signal events used in this analysis has a normalisation factor of 6.53 ${F_2^\tau}^2(0)$. Whilst it may appear that not enough signal events have been generated, i.e. the normalisation factor should be less than one so that the statistical fluctuations of the Monte Carlo tend to be smaller than those of the data, if the standard model prediction for $F_2^\tau(0)$ [18] is used then the normalisation factor is equal to 0.00769. Thus the number of signal events generated is sufficient unless a large enhancement of the standard model value of $F_2^\tau(0)$ is found.

5.2.2 The background Monte Carlo generators

To isolate a sample of data which contains a high purity of signal events it is necessary to have Monte Carlo generators that simulate most of the non-signal (or background) processes that contribute events to the data sample. Then the distributions produced by the signal Monte Carlo can be compared to those of the background Monte Carlo generators so that cuts can be developed to produce the required sample.

The background Monte Carlo generators which are required for this analysis are shown below along with the processes they simulate.

- BABAMC [30] [31] [32] generates $e^+e^- \to e^+e^-(\gamma)$ events. It includes full $\mathcal{O}(\alpha)$ electroweak corrections, but does not include full exponentiation, higher order corrections to the Z width and the energy dependence of the Z width;

- KORALZ [33] [34] [35] generates $e^+e^- \to \mu^+\mu^-$ and $e^+e^- \to \tau^+\tau^-$ events. It contains second order initial state radiation with full exponentiation, but there is only first order final state radiation;

- HVFL generates $e^+e^- \to q\overline{q'}$ events within the JETSET73 [36] framework;

- PHOPHO [37] generates $e^+e^- \to e^+e^-X$ events, where X is created by gamma-gamma annihilation and can be either a multihadronic state via the VDM process, a pair of leptons produced through QED or a single resonance;

- GGMJET [38] is an implementation of the multijet QCD processes in gamma-gamma collisions, where two primary high p_T jets are produced along with one or two beam pipe jets from the photon;

- GGG [51] is a one loop QED Monte Carlo for the production of two photons including the radiation of a third photon (soft or hard).

The GGG Monte Carlo generator has been included as there is a possibility that one of the photons will interact with the material of the detector and convert to two electrons. Therefore this Monte Carlo can produce events which will survive the topological selection.

The method used to normalise the results of the Monte Carlo generated event samples to those of the data is to scale the former by the ratio of the integrated luminosities of the data and Monte Carlo samples (section 3.3.1). The normalisaton factors for the Monte Carlo generated events used in this analysis are shown in table 5.1. It should be noted that the process with a normalisation factor larger than one makes an insignificant contribution to the final result.

5.2.3 Topological selection

This procedure selects events with two or four good tracks and one good photon, all other final state configurations are discarded. For this analysis a good track is defined to be a charged track identified during event reconstruction (section 2.13) where

- the number of TPC hits associated with the track is ≥ 4 (if the track has momentum ≥ 15 GeV/c then there must be at least 8 TPC hits and 1 ITC hit);

Process	Normalisation factor
$e^+e^- \to e^+e^-$	0.652
$e^+e^- \to \mu^+\mu^-$	0.233
$e^+e^- \to \tau^+\tau^-$	0.0706
$e^+e^- \to q\bar{q}'$	0.25
$\gamma\gamma \to e^+e^-$	0.488
$\gamma\gamma \to \mu^+\mu^-$	0.462
$\gamma\gamma \to \tau^+\tau^-$	0.243
$\gamma\gamma \to q\bar{q}'$	1.72
$e^+e^- \to \gamma\gamma(\gamma)$	0.272

Table 5.1: The normalisation factors for the sets of events produced by the background Monte Carlo generators which are used in this analysis.

- the radial distance of closest approach to the beam axis < 2 cm;
- the z coordinate of the closest approach to the beam axis < 7.5 cm;
- the angle between the charged track and the beam axis $> 18.2°$.

These ensure that only tracks originating from the region where there are beam crossings and that have accurately measured four-momentum are used in the analysis.

If an event is found to have two or four good tracks then it is also required that

- the sum of the charges of the good tracks must be zero;
- the total transverse momentum of the good tracks must be greater than 1 GeV/c;
- if there are four good tracks then one combination of three of these tracks must have an invariant mass less than or equal to the tau mass.

The first of these cuts enforces the requirement that electric charge must be conserved whilst the second rejects events where the four-momenta of the good tracks are not likely to have been well measured by the apparatus. The third cut is included to make sure that three of the tracks in a four track event are from a tau decay. Events where two or more combinations of three tracks have an invariant mass less than or equal to the tau mass are discarded as in the later stages of this analysis it is necessary to combine the three tracks which are thought to originate from a tau into one track.

The set of photons identified by the algorithm explained in section 2.14.2 are used as the initial candidates in the search for a good photon. The algorithm of section 2.14.2 attempts to find photons in the energy depositions of the electromagnetic calorimeter which are not associated to a charged track. For this analysis a good photon is defined to be a photon from the set of initial candidates which

- is the only identified photon from its parent electromagnetic calorimeter deposition;
- is not in a crack or dead storey of the electromagnetic calorimeter;
- has a polar angle greater than $18.2°$.

The first of these requirements reduces the contamination of π^0s. These nearly always decay to two photons almost immediately after they are produced, and the photons, due to relativistic collimation, generally produce only one cluster in the electromagnetic calorimeter. Given that π^0s are routinely produced by tau decays, this cut is necessary so that the decay photons are not used as good photon candidates. The last two criteria ensure that the four-momentum of the photon is well measured.

There are two additional constraints that must be satisfied by good photons, and are introduced so that signal events are preferentially selected over background tau events. To motivate these constraints consider the plots in fig. 5.1 which show the photon energy versus the smaller of the two angles between the photon and the taus (called the isolation angle and denoted by $\theta_{\tau\gamma}$) for $e^+e^- \to Z \to \tau^+\tau^-\gamma$ events from the signal and tau background Monte Carlo

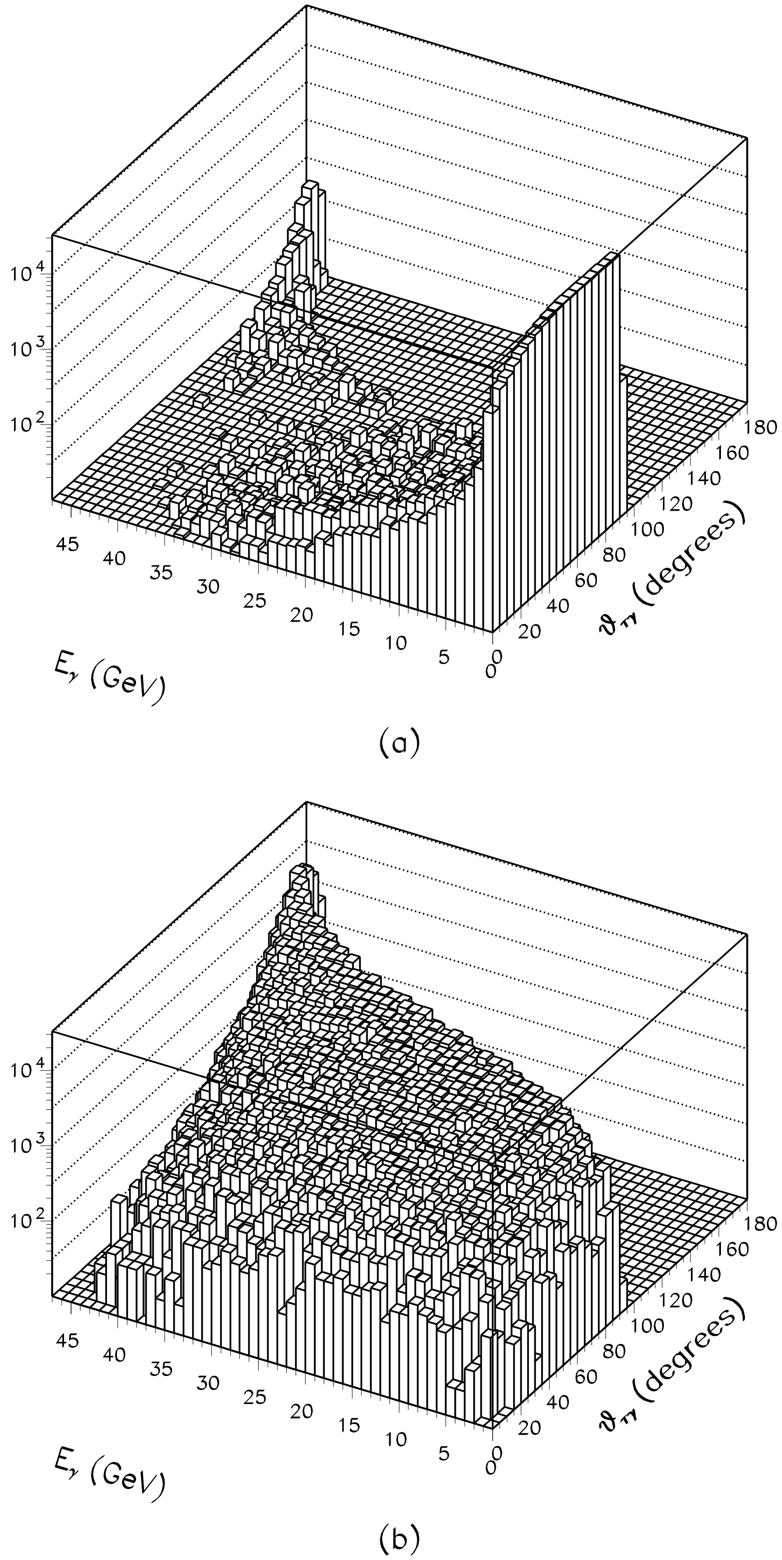

Figure 5.1: Plots showing the photon energy versus the isolation angle of the photon for $e^+e^- \to Z \to \tau^+\tau^-\gamma$ events in (a) tau background Monte Carlo and (b) the signal Monte Carlo.

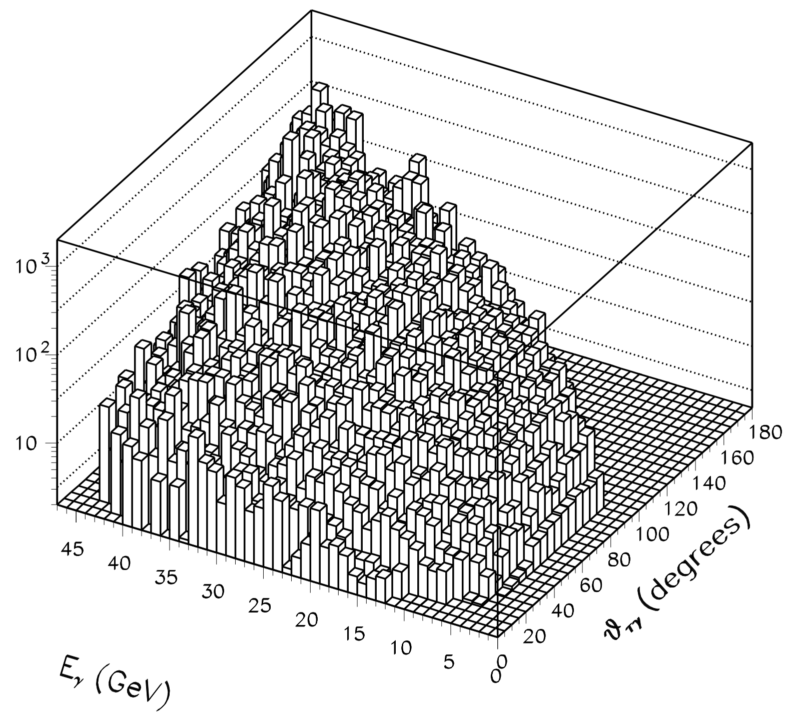

Figure 5.2: The ratio of the signal and tau background Monte Carlo plots for the photon energy versus the isolation angle of the photon for $e^+e^- \to Z \to \tau^+\tau^-\gamma$ events.

generators before the taus have decayed. The distribution for the signal has been normalised to that of the tau background with the value of $F_2^\tau(0)$ set to one. The plot of fig. 5.2 shows the ratio of these two distributions. It is possible to observe that the photon in a signal event is more likely to have a large energy and isolation angle than those in the events of the background Monte Carlo. Due to the fact that the decay products of the tau are normally subjected to severe relativistic collimation [52], meaning that the decay products travel in the same direction as the parent tau, the definition of a good photon also requires that

- the isolation angle between the photon and the good tracks is greater than $30°$;
- the energy of the photon is greater than 3 GeV.

These cuts increase the ratio of signal to tau background. By imposing harsher cuts the signal to background ratio would be further increased, but the aim of the data selection is not to reject all of the tau background events as one of the methods for extracting a limit involves fitting the data to the signal and background. This is impossible if there are no data or background Monte Carlo events.

If the number of photons satisfying all the above constraints is greater than one then the good photon is taken to be the photon with the largest energy.

The results of the topological selection are displayed in tables 5.2, 5.3 and 5.4. These show that 4845 data and 4751 background Monte Carlo events survive the cuts. Taking into account the errors on the data and the background Monte Carlo, this is a difference of 1.2 standard deviations. A breakdown of the contributions of each of the background Monte Carlo generators to the total of 4751 events can be found in tables 5.3 and 5.4.

Table 5.2 also shows that $16190 {F_2^\tau}^2(0)$ signal events survive the selection. This is a combined acceptance and efficiency of 49.6%. The cut which causes the main loss of signal events is the requirement that all charged tracks and the photon have a polar angle greater than 18.2°. This is because, as fig. 5.1 (b) indicates, it is quite likely for the final state particles of signal events to be well separated from each other, and therefore there is an increased probability that some of the final state particles will not pass the polar angle cut.

5.2.4 Rejection of non-tau events

The process of extracting a limit for $F_2^\tau(0)$ requires a data sample that consists mainly of $Z \to \tau^+\tau^-\gamma$ decays. Tables 5.2 and 5.3 show that the tau background Monte Carlo events constitute only 22.6% of the background Monte Carlo total. Therefore it is necessary to implement further cuts to enhance the contribution of the tau Monte Carlo to the total number of Monte Carlo events.

The reduction of non-tau backgrounds is done in two stages. In the first stage a cut is introduced which eliminates the majority of $\gamma\gamma \to X$ events, whilst the

Cut	Data	Background MC sum	$\frac{\text{MC} - \text{data}}{\sqrt{\sigma_{\text{data}}^2 + \sigma_{\text{MC}}^2}}$	Signal MC
None	ALL	2261106		$32629 F_2^{\tau\,2}(0)$
Topological selection	4845	4751	-1.2	$16190 F_2^{\tau\,2}(0)$
$\gamma\gamma \to X$ rejection	1183	1173	-0.3	$13710 F_2^{\tau\,2}(0)$
Missing mass cut	691	656	-1.4	$12679 F_2^{\tau\,2}(0)$

Table 5.2: Effect of the cuts on data, summed background Monte Carlo and signal Monte Carlo.

	$e^+e^- \to e^+e^-$	$e^+e^- \to \mu^+\mu^-$	$e^+e^- \to \tau^+\tau^-$
Number of events generated	166600	312394	1024567
Normalised number of events generated	108690	72788	72334
Topological selection	1864	1326	1075
$\gamma\gamma \to X$ rejection	239	96	769
Missing mass cut	7	3	634

Table 5.3: Breakdown of numbers for the background Monte Carlo generators which produce charged leptons.

	$e^+e^- \to q\overline{q'}$	$\gamma\gamma \to X$	$e^+e^- \to \gamma\gamma(\gamma)$
Number of events generated	5854976	546619	80000
Normalised number of events generated	1465500	520010	21784
Topological selection	213	121	152
$\gamma\gamma \to X$ rejection	40	1	28
Missing mass cut	8	1	3

Table 5.4: Breakdown of numbers for the other background Monte Carlo generators.

second stage utilises the fact that, because of undetected neutrinos, $Z \to \tau^+\tau^-\gamma$ events always have missing mass. The combined effect of these two cuts is to increase the purity of the data sample whilst decreasing the efficiency of the signal. Hence the exact positioning of the cuts was optimised so that the lowest limit for $F_2^\tau(0)$ was obtained.

The method used to reduce the $\gamma\gamma \to X$ contribution is identical to that employed in the search for the Higgs boson peformed by ALEPH where events containing a pair of acoplanar charged particles were analysed [53]. This method makes use of the fact that the beam particles which radiate the photons are usually not detected because of their low polar angle, meaning that the total transverse momentum of the detected particles produced by gamma fusion is small. Therefore to remove such events it is required that the magnitude of the transverse component of both the momentum of the combined good tracks and the total visible momentum is greater than 3.75% of the centre of mass energy.

It is possible that one of the beam particles radiating a photon is in the acceptance of LCAL (section 2.11) but that its azimuthal angle is such that it passes through an LCAL crack and is not detected. Thus the detected particles of such an event will tend to have a total transverse momentum which is larger than the average. Hence if the missing momentum vector of the event is both in the acceptance of LCAL and within $\pm 10°$ of an LCAL crack then it is required that both transverse momentum components are greater than 5% of the centre of mass energy.

The plots in fig. 5.3 show the distributions of the tranverse momentum of the good tracks divided by M_Z (which is equal to the centre of mass energy for all of the events in this analysis) in data and Monte Carlo. Similar plots are obtained for the distributions of the tranverse component of the total visible momentum divided by M_Z. The vertical lines on the plots indicate the exact positioning of the cut. It is possible to observe that virtually all $\gamma\gamma \to X$ events are rejected (fig. 5.3 (a)) whilst only a small fraction of the signal and tau background events are discarded (fig. 5.3 (d) and (e) respectively).

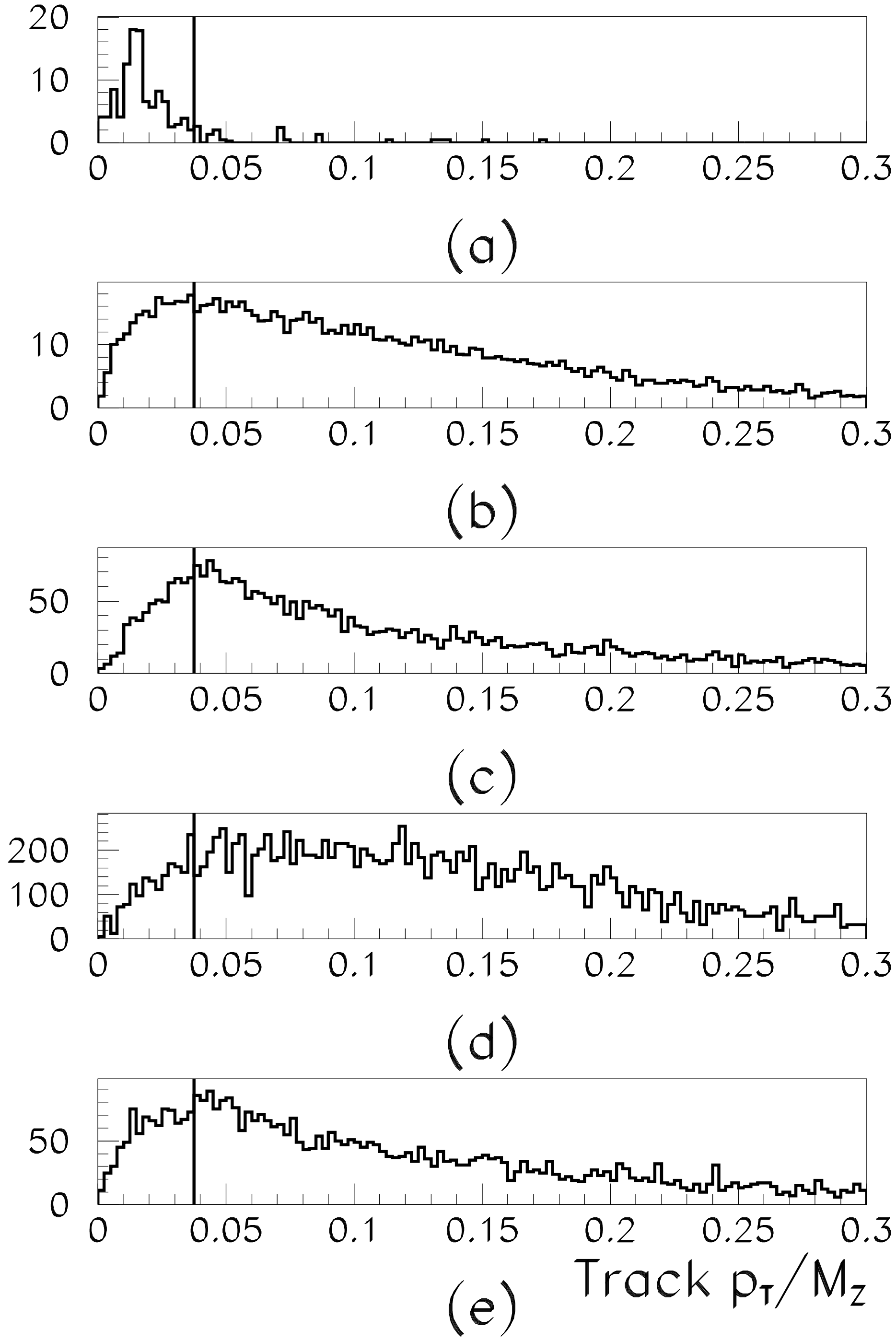

Figure 5.3: Plots showing the total tranverse momentum of the good tracks divided by M_Z for (a) $\gamma\gamma \to X$ Monte Carlo, (b) tau background Monte Carlo, (c) the remaining background Monte Carlo, (d) signal Monte Carlo and (e) the data. The line in each plot shows where the cut to reject $\gamma\gamma \to X$ events was placed.

The number of data and Monte Carlo events surviving this cut are 1183 and 1173 respectively (table 5.2). This is a difference of 0.3 standard deviations.

This cut reduces the number of signal events to $13710 F_2^{\tau\,2}(0)$, a combined acceptance and efficiency of 42.0%.

Following the rejection of the $\gamma\gamma \to X$ events the purity of the Monte Carlo sample is too low for a good limit for $F_2^\tau(0)$ to be extracted; only 65.6% of the Monte Carlo total is due to the tau background contribution. The most significant contamination comes from Bhabha and dimuon events (20.4% and 8.2% respectively). An effective way of reducing the contribution of these two channels to the Monte Carlo total, whilst increasing that of both the signal and the tau background, is to demand that all events have missing mass. This achieves the required aim as there is always at least one neutrino created when a tau decays, meaning that $Z \to \tau^+\tau^-\gamma$ events always have energy, or mass, which is undetected, whilst events from Bhabha and muon generators do not contain neutrinos and therefore, allowing for the resolution and acceptance of the detector, have a total detected energy which is equal to the centre of mass energy.

The missing mass squared of an event is usually defined as p^2_{miss}, with

$$p_{\text{miss}} = (E_{\text{cms}} - E_{\text{vis}}, -\vec{p}_{\text{vis}})$$

where E_{cms} is the centre of mass energy and p^μ_{vis} $(= (E_{\text{vis}}, \vec{p}_{\text{vis}}))$ is the total detected four-momentum. The latter quantity is obtained by summing the four-momenta of all energy flow objects.

For this analysis, however, the missing mass squared is defined as p'^2_{miss}, with

$$p'_{\text{miss}} = (E_{\text{cms}} - E_{\text{vis}} + E_\gamma, -\vec{p}_{\text{vis}} + \vec{p}_\gamma)$$

where p^μ_γ $(= (E_\gamma, \vec{p}_\gamma))$ is the four-momentum of the good photon.

To illustrate why this definition of missing mass squared is adopted consider the values of p^2_{miss} and p'^2_{miss} for those events that contain final state neutrinos, e.g. $Z \to \tau^+\tau^-\gamma$, and those without final state neutrinos, e.g. radiative Bhabha and $Z \to \mu^+\mu^-\gamma$ events. In the latter case, allowing for the effects of acceptance and resolution of the apparatus, all the particles are detected which means that

$p_{\text{miss}} \approx (0, \vec{0})$ and $p'^{\mu}_{\text{miss}} \approx p^{\mu}_{\gamma}$. Therefore both p^2_{miss} and p'^2_{miss} are generally approximately zero. However, for the $Z \to \tau^+\tau^-\gamma$ events $p^{\mu}_{\text{miss}} \approx p^{\mu}_{\nu}$, where p^{μ}_{ν} is the total four-momentum of the neutrinos in the event, and thus $p'^{\mu}_{\text{miss}} \approx p^{\mu}_{\nu} + p^{\mu}_{\gamma}$. Therefore $p'^2_{\text{miss}} > p^2_{\text{miss}}$.

Hence p'^2_{miss} is defined as the missing mass squared, rather than adopting the conventional definition of p^2_{miss}, because it enhances the ability to differentiate $Z \to \tau^+\tau^-\gamma$ events from radiative Bhabha and $Z \to \mu^+\mu^-\gamma$ events, enabling a cut to be made which will increase the purity of the data sample without dramatically reducing the efficiency of the signal.

The plots of fig. 5.4 show the distributions of missing mass squared for data and Monte Carlo. It was found that the optimum final result is obtained if a cut is made requiring events to have a missing mass squared greater than 500 $(\text{GeV}/\text{c}^2)^2$. The vertical lines on the plots are positioned at this value. It is possible to observe from fig. 5.4 (a), (b) and (c) that the majority of non-tau background is rejected without a significant loss from either the signal or the tau background.

It appears from the plots of fig. 5.4 that the cut on missing mass squared could be lowered, so that more signal is preserved, without incurring a dramatic increase of the non-tau background. The reason for placing the cut at a higher value is to increase the ratio of signal to tau background so that a better final result is extracted, and the optimum placement of the cut was found to be 500 $(\text{GeV}/\text{c}^2)^2$.

There are 691 data and 656 background Monte Carlo events remaining after the missing mass squared cut has been imposed (table 5.2). This is a difference of 1.4 standard deviations. The proportion of the Monte Carlo total which comes from the tau background is now 96.6% (tables 5.2 and 5.3). There are $12679 F_2^{\tau\,2}(0)$ signal events surviving the cut, giving a combined acceptance and efficiency of 38.9%.

Further cuts to reduce the non-tau backgrounds were investigated (such as the rejection of events with only two good tracks if both are electrons or muons)

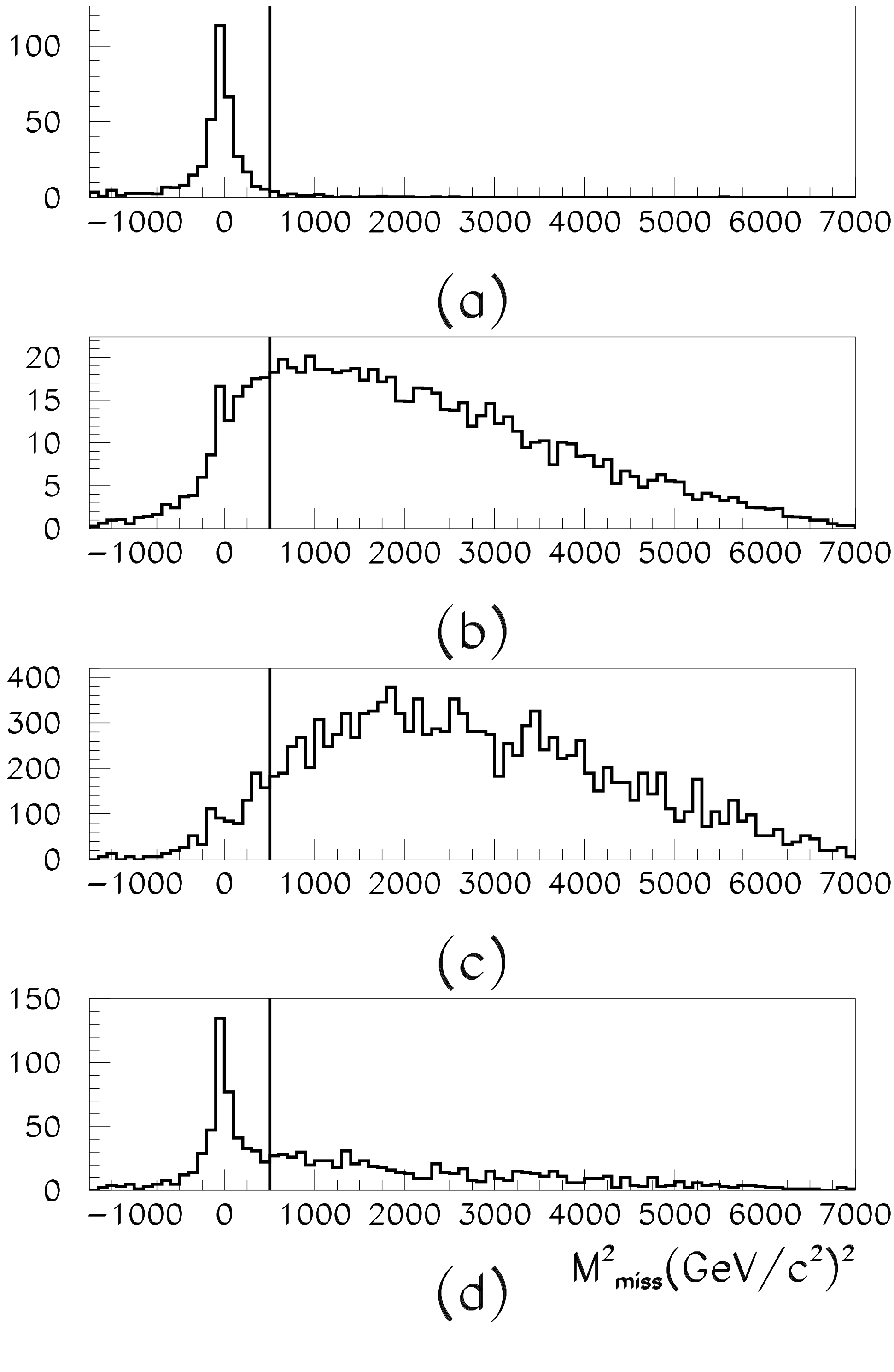

Figure 5.4: Plots showing the missing mass squared for (a) non-tau background Monte Carlo, (b) tau background Monte Carlo, (c) signal Monte Carlo and (d) the data. The line in each plot shows where the cut was placed.

but none were found which improved the final result.

5.3 Extracting a limit for the anomalous magnetic moment of the tau

The implementation of the cuts detailed above produces the data and Monte Carlo samples required to obtain a limit for $F_2^\tau(0)$. The underlying principle of any method which can be used to extract the limit is to determine the number of events in the data which are caused by the signal process ($n_{\rm signal}$). This is achieved by comparing the data sample with that constructed by adding the signal and background Monte Carlo events. Then, given that the integrated luminosity of the data, $\mathcal{L}_{\rm data}$, is known, and that the cross-section for the signal, $\sigma_{\rm signal}$, is proportional to ${F_2^\tau}^2(0)$, it is possible to obtain the limit using

$$n_{\rm signal} = \mathcal{L}_{\rm data}\, \sigma_{\rm signal}. \qquad (5.1)$$

The two methods invoked by this analysis to obtain a limit for $F_2^\tau(0)$ are - to apply the results of the theory of Poisson processes to the number of events in the data, background and signal samples; and to use the method of least squares on the distributions of quantities related to the geometry of the final state particles of the three samples. The outline of these two methods is given below.

5.3.1 Obtaining a limit using the theory of Poisson processes

If the theoretical prediction for the number of events present in a data sample obtained from a Poisson process can be split into signal and background contributions then, for a given confidence level, it is possible to set an upper limit on the number of data events which are caused by the signal process. An illustration of how this is achieved is given below.

Let n_0 be the number of events in the data sample, and μ_s and μ_b the predicted mean of the signal and background respectively. Whilst the actual number of background in the data is not known, it is assumed that the error on μ_b is small. If the upper limit for μ_s, denoted by N, is defined such that the probability of $\mu_s \leq N$ is greater than or equal to $1 - \epsilon$, where ϵ is the confidence coefficent, then [54]

$$1 - \epsilon = 1 - \frac{e^{-(\mu_b+N)} \sum_{n=0}^{n_0} \frac{(\mu_b+N)^n}{n!}}{e^{-\mu_b} \sum_{n=0}^{n_0} \frac{\mu_b^n}{n!}} \tag{5.2}$$

Hence it is possible to know with confidence level $1 - \epsilon$ that there are at most N signal events in the data, and thus equation 5.1 can be used to obtain the limit on $F_2^\tau(0)$ at $1 - \epsilon$ confidence level.

Throughout this analysis all limits for $F_2^\tau(0)$ obtained using equation 5.2 have $1 - \epsilon$ equal to 0.95, i.e. are at the 95% confidence level.

5.3.2 Obtaining a limit using the method of least squares

The method of least squares [55] with no free parameters is normally used to measure the level of correlation between two sets of data, here labelled x_i and y_i. This is achieved by using the χ^2 / degree of freedom to obtain a confidence level that the two sets of data were produced by the same process. In this instance,

$$\chi^2 = \sum_i \frac{(x_i - y_i)^2}{\sigma_{x_i}^2 + \sigma_{y_i}^2}.$$

Free parameters can be introduced into the method of least squares to increase the level of correlation between the data sets by allowing χ^2 access to values lower than that obtained with no free parameters. The effect of the decrease in χ^2 may, however, be counteracted by the fact that each free parameter decreases the number of degrees of freedom by one. The minimum value of χ^2 gives the best fit of x_i to y_i (or y_i to x_i depending on how the free parameters are deployed) for the given parameters and their allowed ranges. The values of the parameters which give the minimum are known as the fitted values.

It is possible to obtain a limit for the anomalous magnetic moment of the tau by subjecting the data and combined Monte Carlo samples to the method of least squares with $F_2^\tau(0)$ as one of the free parameters. The fitted value of the Pauli form factor, $F_{2\ \mathrm{fitted}}^\tau(0)$, along with its associated Gaussian error, σ_{F_2}, can be used to produce the upper limit $F_{2\ \mathrm{limit}}^\tau(0)$ at 95% confidence level by requiring

$$\frac{\int_0^{F_{2\ \mathrm{limit}}^\tau(0)} G(F_{2\ \mathrm{fitted}}^\tau(0), \sigma_{F_2})}{\int_0^\infty G(F_{2\ \mathrm{fitted}}^\tau(0), \sigma_{F_2})} = 0.95$$

where $G(\mu, \sigma)$ is a Gaussian of mean μ and width σ.

The χ^2 function required for this analysis is

$$\chi^2 = \frac{(1 - x_{\mathrm{norm}})^2}{\sigma_{\mathrm{norm}}^2} - \sum_i \frac{\{\mathrm{data}_i - (x_{\mathrm{norm}}\mathrm{total\_bmc}_i + F_2^{\tau\,2}(0)\mathrm{signal}_i)\}^2}{\sigma_i^2} \qquad (5.3)$$

where

- $\mathrm{total\_bmc}_i$ is the sum of all background Monte Carlo channels after they have been normalised;
- signal_i is the predicted number of signal events when $F_2^\tau(0)$ is set to one;
- x_{norm} is the normalisation factor for the total Monte Carlo background;
- σ_{norm} is the error on x_{norm};
- σ_i is the total error on $\{\mathrm{data}_i - (x_{\mathrm{norm}}\mathrm{total\_bmc}_i + F_2^{\tau\,2}(0)\mathrm{signal}_i)\}$.

The only free parameters in equation 5.3 are $F_2^\tau(0)$ and x_{norm}. The latter parameter is introduced so that any systematic effects in the method used to normalise the background Monte Carlo would not affect the limit obtained for $F_2^\tau(0)$.

The error on the total Monte Carlo normalisation factor is conservatively taken to be 1%. This value, which is larger than necessary, is adopted to avoid having to consider the complex systematic errors which would arise if a lower value were used. All of the limits obtained using equation 5.3 were found to be stable if σ_{norm} was varied between 0.1% and 10%, showing that the error on the normalisation is not a significant factor.

A problem arises because the method of least squares requires the samples being used to have Gaussian errors whereas the data and Monte Carlo samples have Poisson errors. This is overcome by requiring that the data_i used in equation 5.3 are always greater than five, leading to the errors on the data_i being approximately Gaussian. The assumption that there are more unnormalised Monte Carlo events than data means that if the data_i have approximately Gaussian errors then so will $\mathrm{total\_bmc}_i$ and signal_i.

The maximum likelihood method is not considered because a large amount of theoretical effort is required to obtain the necessary probability density function.

5.4 Results

The two distributions which are used to obtain the data_i, $\mathrm{total\_bmc}_i$ and signal_i required by equation 5.3 are the energy of the good photon and the acollinearity of the tracks. The acollinearity in an event with two good tracks is defined as the angle between the tracks. For an event with four good tracks, however, it is defined as the angle between the track created by the recombination of three tracks which has an invariant mass less than or equal to the tau mass and the remaining track. Why these distributions have been chosen is illustrated by the plots of figs. 5.5 and 5.6, which show the good photon energy versus acollinearity for the data, background Monte Carlo and signal Monte Carlo samples which survive the topological selection and rejection of non-tau background. It is possible to observe that the distribution of the signal is significantly different from those of either the data or the background, and that regions of both the good photon energy and acollinearity distributions are sensitive to the presence of a signal.

The results obtained by using the method of least squares to minimise equation 5.3, where data_i, $\mathrm{total\_bmc}_i$ and signal_i are obtained from the acollinearity and good photon energy distributions, can be seen in table 5.5. The resolution used for the acollinearity distribution is 0.05 radians and that of the good photon energy distribution is 0.5 GeV. Both of these are lower than the highest

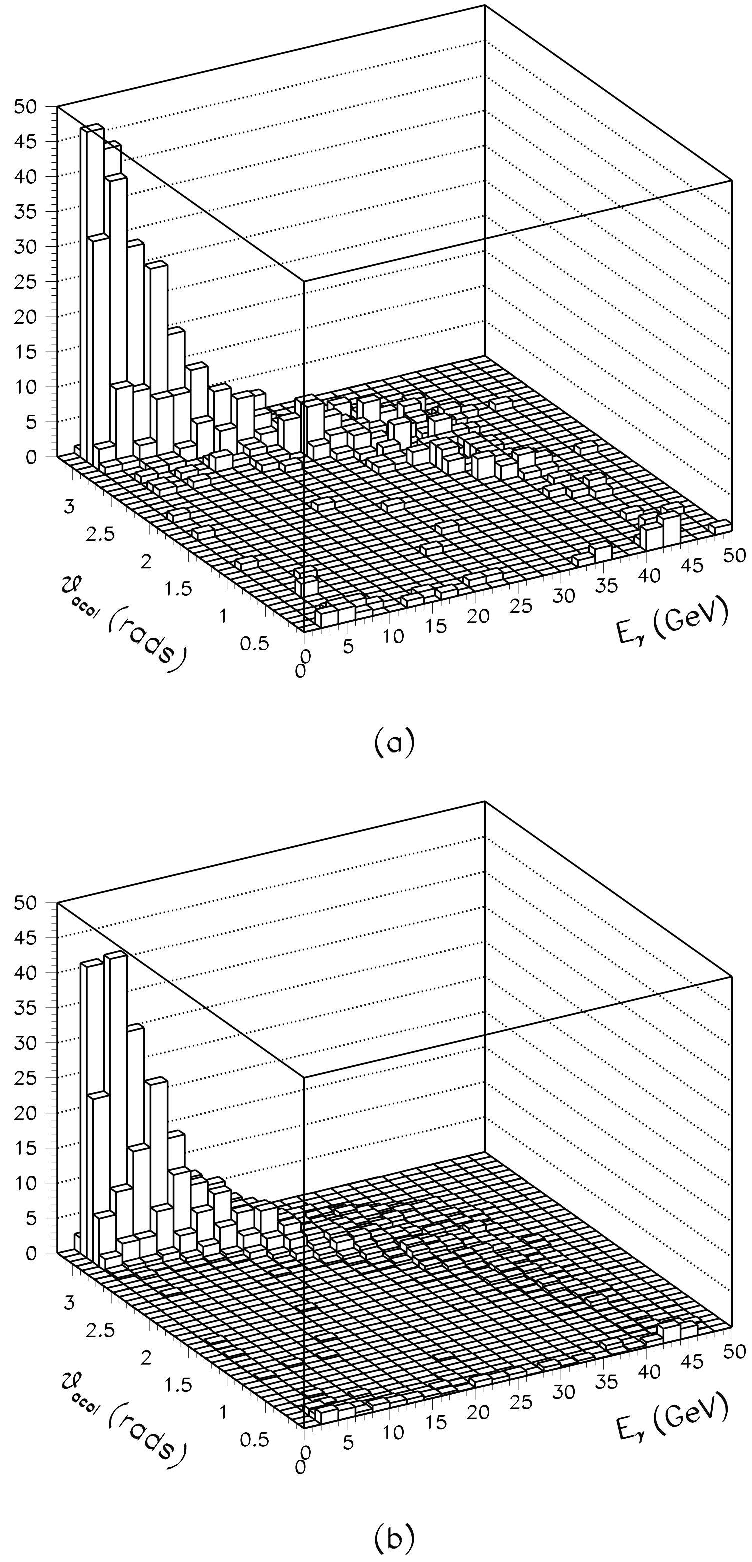

Figure 5.5: A plot of the energy of the good photon versus the acollinearity of the tracks for (a) the data and (b) the background Monte Carlo after topological selection and rejection of non-tau backgrounds.

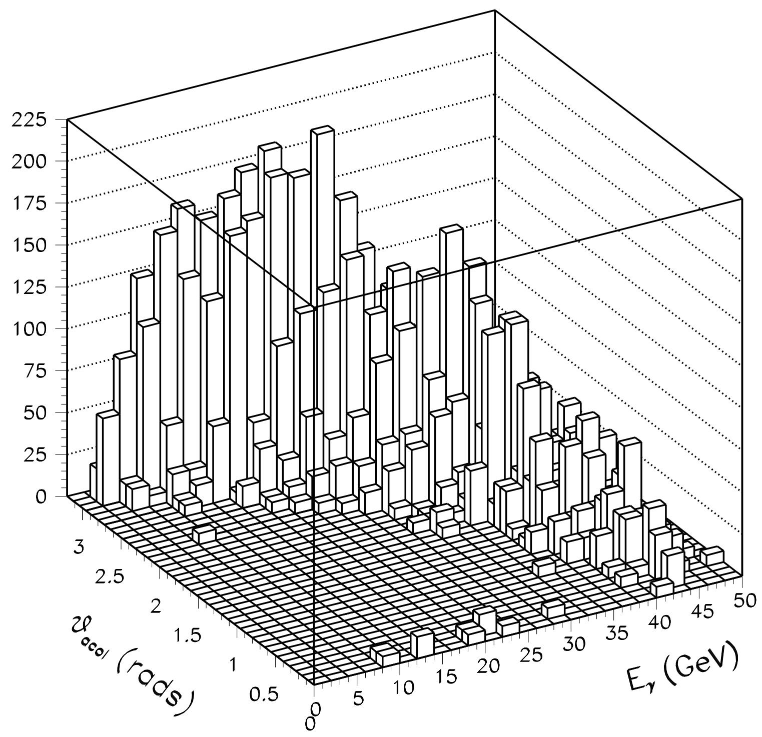

Figure 5.6: A plot of the energy of the good photon versus the acollinearity of the tracks for the signal Monte Carlo after topological selection and rejection of non-tau backgrounds.

detector resolution [23]. The 95% c.l. limit obtained by fitting acollinearity is $F_2^\tau(0) < 0.060$ and that from the good photon energy is $F_2^\tau(0) < 0.051$. The fitted values of the parameters have been used to obtain the plots in figs. 5.7 and 5.8, which show respectively the acollinearity and photon energy distributions of the data, fitted background and fitted signal.

The limit obtained by applying the theory of Poisson processes to the samples surviving topological selection and the rejection of non-tau backgrounds is $F_2^\tau(0) < 0.079$ at 95% c.l.

The results contained in table 5.5 show that there is very high correlation between data and background Monte Carlo for both distributions.

Having obtained the limits by applying the method of least squares to the whole of the allowable ranges of acollinearity ($0 \leq \theta_{\text{acol}} \leq \pi$) and good photon

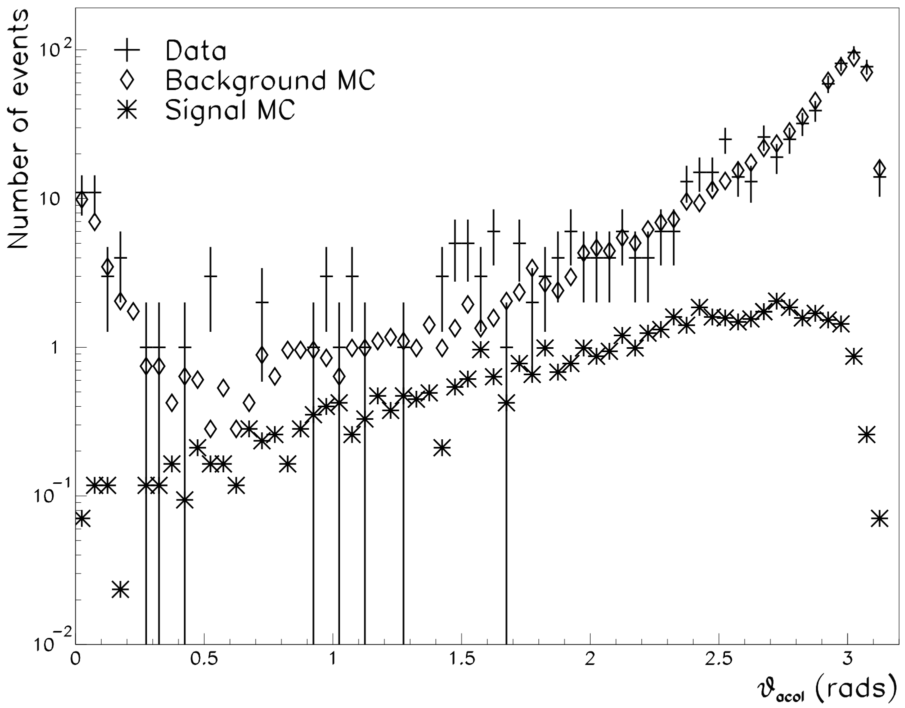

Figure 5.7: The result of fitting the acollinearity after topological selection and rejection of non-tau backgrounds.

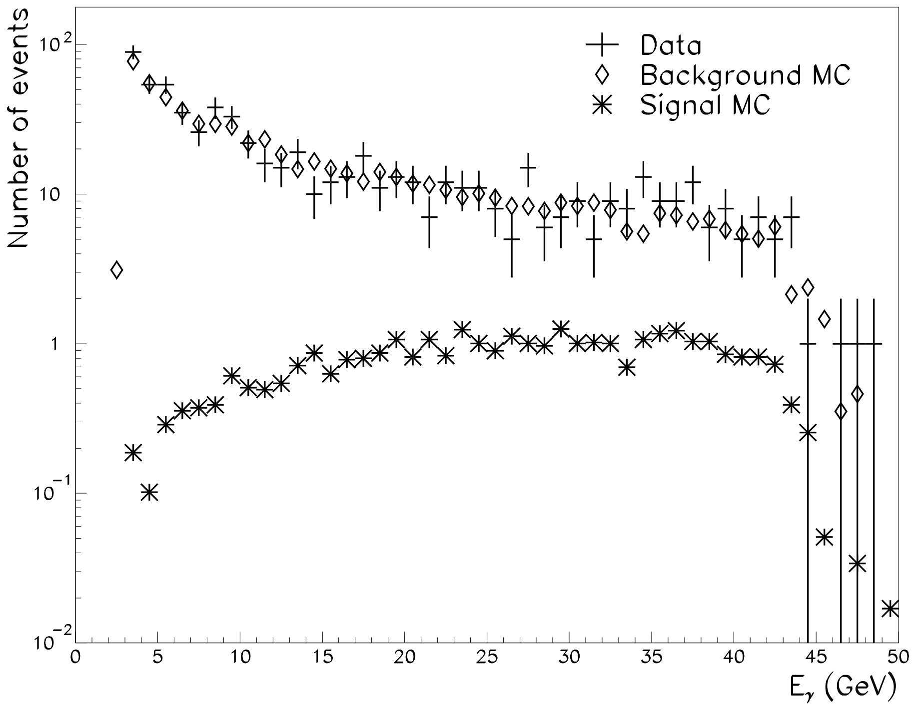

Figure 5.8: The result of fitting the good photon energy after topological selection and rejection of non-tau backgrounds.

	Distribution used in the fit	
	Acollinearity	Good photon energy
$F_{2\ \text{fitted}}^{\tau}(0)$	0.0012 ± 0.0014	-0.0006 ± 0.0015
x_{norm}	0.999 ± 0.010	0.999 ± 0.010
χ^2 / dof	28.2 / 31	51.2 / 60
$F_{2\ \text{limit}}^{\tau}(0)$	0.060	0.051

Table 5.5: The results obtained by fitting the acollinearity and good photon energy of the Monte Carlo to the data after topological selection and rejection of non-tau backgrounds.

energy ($0 < E_\gamma < 50$), the next stage is to determine whether a better limit can be achieved if only certain regions of these ranges are used. Fig. 5.9, which contains the ratio of the acollinearity versus good photon energy distributions of signal and data, indicates that implementing cuts on good photon energy and acollinearity should produce lower limits, as certain regions of the distributions of these quantities are more sensitive to the presence of a signal than others.

It is not good practice to use the data to obtain the optimum limits of the distributions because of its inherent statistical fluctuations. If the data was used to obtain the optimum limits then the reason why it is the best result may be based on statistical, rather than physical, effects. Therefore, to avoid the problems created by statistical effects, it is necessary to construct a substitute data sample using a set of Monte Carlo events with a normalisation factor much less than one. The substitute data, however, is given the same Poisson errors as the data; the only reason for introducing the fake data is to smooth the distributions.

Replacing the data with a set of events produced by the background Monte Carlo generators used in this analysis appears justifiable as table 5.5 shows the high correlation between data and background. The fake data sample used to optimise the limits consists of a set of events produced by the background Monte Carlo generators which has a normalisation factor of 0.0733.

The process of achieving the optimum limits of the distributions involves using

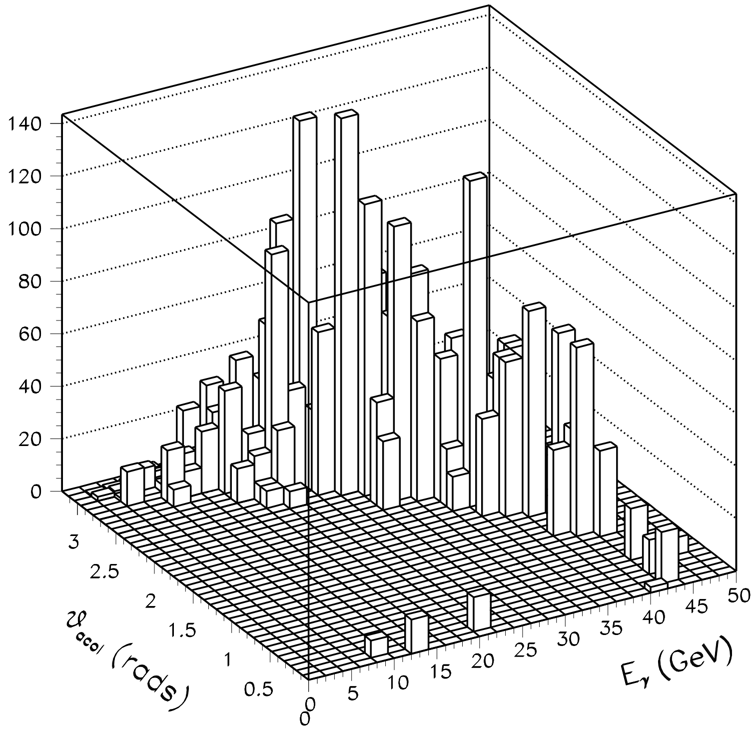

Figure 5.9: A plot of the energy of the good photon versus the acollinearity of the tracks for the ratio of the signal and data after topological selection and rejection of non-tau backgrounds.

the method of least squares to compare the samples of fake data, background and signal produced by applying cuts to either the good photon energy or acollinearity, depending on which distribution is being considered. The cuts giving the lowest limit for a distribution are imposed on the data, background and signal to produce the samples which give the optimum limit of that distribution.

If the fake data is used and only topological and background rejection cuts are implemented, that is no cuts are made on either good photon energy or acollinearity, then the limits $F_2^\tau(0) < 0.046$ and $F_2^\tau(0) < 0.048$, both at 95% c.l., are obtained by fitting acollinearity and good photon energy respectively. The limit predicted by Poisson theory is $F_2^\tau(0) < 0.067$ at 95% c.l.

For the fake data the lowest limit of the good photon energy distribution is obtained when its resolution is decreased to one GeV and 21 GeV$< E_\gamma <$46 GeV. Then the method of least squares gives $F_2^\tau(0) < 0.046$ and Poisson theory

$F_2^\tau(0) < 0.050$, both at 95% c.l.

With fake data the acollinearity distribution has lowest limits of $F_2^\tau(0) < 0.043$ by the method of least squares and $F_2^\tau(0) < 0.044$ from Poisson theory, both at 95% c.l. These are obtained by imposing the constraint $\theta_{\mathrm{acol}} < 2.6$ radians.

Table 5.6 shows the results of the fits and the optimum limits obtained when the data is reinstated. The optimisation procedure has made all of the limits higher rather than lower; for example, before optimisation the limit obtained from fitting acollinearity was 0.060, whereas after optimisation this limit is 0.067.

One of the possible explanations as to why they have all increased is that the optimisation did not significantly improve the limits of the fake data, e.g. for the photon energy and acollinearity distributions the limits went from 0.048 to 0.046 and 0.046 to 0.043 respectively, and it could be that the statistical fluctuations of the data partially cancel the improvement.

Another problem is if there are any very significant systematic differences between the distributions of data and Monte Carlo then the optimisation process is invalid. There do not appear to be major differences between the data and Monte Carlo distributions, but if there are subtle systematic effects then the result of the optimisation process could be arbitrary.

A further problem is that the optimisation cuts reduce the total number of events in the samples which leads to the error on $F^\tau_{2\,\mathrm{fitted}}(0)$ being larger, and hence a higher limit is obtained.

Therefore the best result obtained by this analysis is when the method of least squares is applied to the photon energy distribution following topological selection and rejection of non-tau backgrounds, where a limit of $F_2^\tau(0) < 0.051$ is achieved.

A two dimensional fit was not considered because of the low statistics and the requirement that data_i is greater than or equal to five.

	Distribution used in the fit	
	Acollinearity	Good photon energy
$F^{\tau}_{2\ \mathrm{fitted}}(0)$	0.0020 ± 0.0015	0.0005 ± 0.0016
x_{norm}	1.000 ± 0.010	0.999 ± 0.010
χ^2 / dof	21.3 / 20	24.0 / 21
$F^{\tau}_{2\ \mathrm{limit}}(0)$	0.067	0.059
$F^{\tau}_{2\ \mathrm{Poisson}}(0)$	0.089	0.072

Table 5.6: The results obtained by fitting the acollinearity and good photon energy of the Monte Carlo to the data after topological selection, rejection of non-tau backgrounds and optimisation.

5.5 Conclusion

The limit for the anomalous magnetic moment of the tau achieved by this analysis is an order of magnitude larger than the value predicted by the standard model, that is from this analysis $F^{\tau}_2(0) < 0.051$ whilst the standard model predicts $F^{\tau}_2(0) = 11\,773(3) \times 10^{-7}$ [18]. Therefore this analysis does not rule out the possibility of physics beyond the standard model which enhances the anomalous magnetic moment of the tau. However, no indications of such physics have been observed, and the reason for the high limit is a lack of data.

To understand the significance of this result the existing experimental limits are listed below, along with a brief explanation of how they were obtained.

- $F^{\tau}_2(0) < 0.02$ [50] was obtained by using data from PETRA to analyse the process $e^+e^- \to \gamma \to \tau^+\tau^-$;

- $F^{\tau}_2(0) < 0.11$ [45] was achieved when L3 data was used to analyse the decay $Z \to \tau^+\tau^-\gamma$;

- $F^{\tau}_2(0) < 0.39$ [56] results from a 'crude' analysis of the angular distributions of the final state particles in $e^+e^- \to Z/\gamma \to \tau^+\tau^-$ events present in SLAC and DESY data;

- $F^{\tau}_2(0) < 0.0062$ [57] was achieved by using all LEP data and considering the increase in Z width that results from the anomalous magnetic moment of the tau.

The result obtained using PETRA data does not actually measure $F_2^\tau(0)$ as here the tau is coupling to an s channel photon which has a non-zero mass. Given that $F_2^\tau(k^2)$, where k^2 is the mass of the photon, has a logarithmic k^2 dependence, some complicated manipulations were required to obtain the limit for $F_2^\tau(0)$.

The limit $F_2^\tau(0) < 0.0062$ is obtained by making the assumption that the anomalous magnetic moment of the tau creates a coupling to the weak bosons in an analogous manner as it does with photons. Then, by studying the decay $Z \to \tau^+\tau^-$, it is possible to put a limit on the additional Z width created by the anomalous magnetic moment of the tau, and hence constrain $F_2^\tau(0)$. This assumption greatly increases the statistics as there is no need for a photon to be present in the final state, explaining the extremely low limit achieved. This analysis also assumes that the logarithmic k^2 dependence of F_2^τ can be ignored.

Therefore the result obtained by this analysis is the lowest limit for $F_2^\tau(0)$ obtained by studying the coupling between taus and real photons.

Appendix A

Trace results required for matrix element calculation

The calculation of the spin averaged matrix element squared in Chapter 4 results in traces of complex expressions. The following results are used to simplify these traces.

$$Tr\ [\not{a}\ \not{b}] = a \cdot b$$

$$Tr\ [\not{a}\ \not{b}\ \not{c}\ \not{d}] = 4\left\{(a \cdot b)(c \cdot d) - (a \cdot c)(b \cdot d) + (a \cdot d)(b \cdot c)\right\}$$

$$Tr\ [\not{a}\ \not{b}\ \not{c}\gamma^{\mu}] = 4\left\{(a \cdot b)c^{\mu} - (a \cdot c)b^{\mu} + (b \cdot c)a^{\mu}\right\}$$

$$Tr\ [\not{a}_1\ \not{a}_2 \ldots \not{a}_{2n+1}] = 0 \qquad \forall\, n \geq 0$$

$$Tr\left[\gamma^5\right] = 0$$

$$Tr\left[\gamma^5 \not{a}\ \not{b}\right] = 0$$

$$Tr\left[\gamma^5 \not{a}\ \not{b}\ \not{c}\ \not{d}\right] = 4i\epsilon_{\mu\nu\rho\delta}a^{\mu}b^{\nu}c^{\rho}d^{\delta}$$

$$Tr\left[\gamma^5 \not{a}\,\not{b}\,\not{c}\,\gamma^\mu\right] = 4i\epsilon_{\nu\rho\delta\mu}a^\nu b^\rho c^\delta$$

$$Tr\left[\gamma^5 \not{a}_1\,\not{a}_2 \ldots \not{a}_{2n+1}\right] = 0 \qquad \forall\, n \geq 0$$

where ϵ is the totally anti-symmetric tensor with $\epsilon_{0123} = 1$.

The complex expressions inside the trace can often be simplified before the trace is taken. The identities below are used to fulfil this purpose.

$$\gamma_\mu \not{a} = -\not{a}\,\gamma_\mu + 2a_\mu$$

$$\gamma^\mu \gamma_\mu = 4$$

$$\gamma^\mu \not{a}\,\gamma_\mu = -2\not{a}$$

$$\gamma^\mu \not{a}\,\not{b}\,\gamma_\mu = 4a \cdot b$$

$$\gamma^\mu \not{a}\,\not{b}\,\not{c}\,\gamma_\mu = -2\not{c}\,\not{b}\,\not{a}$$

$$\gamma^\mu \not{a}\,\not{b}\,\not{c}\,\not{d}\,\gamma_\mu = -2(\not{d}\,\not{a}\,\not{b}\,\not{c} + \not{c}\,\not{b}\,\not{a}\,\not{d})$$

$$\sigma^{\mu\nu} = \frac{i}{2}\left(\gamma^\mu\gamma^\nu - \gamma^\nu\gamma^\mu\right)$$

The proof of some of the above results can be found in [58].

Bibliography

[1] L.E. Ibáñez, "The Standard Model and Beyond", CERN 94-04 (1994) 165.

[2] M. Aguilar-Benitaz et al., Physical Review D 50 (1992) section 26.4.

[3] F. Halzen and A.D. Martin, "Quarks and Leptons: An Introductory Course in Modern Particle Physics", Wiley (1984) section 15.6.

[4] The ALEPH Collaboration, "Improved Mass Limit for the Standard Model Higgs Boson", to be published in The Proceedings of the International Europhyscs Conference on High Energy Physics, Brussels, 1995.

[5] S. Weinberg, Physical Review Letters 19 (1967) 1264.

[6] S. Weinberg, Physics Review D 5 (1972) 1412.

[7] S. Glashow, Nuclear Physics B 8 (1961) 579.

[8] The LEP Collaborations, "Combined Preliminary Data on Z Parameters from the LEP Experiments and Constraints on the Standard Model", CERN-PPE/94-187 (1994).

[9] D.H. Perkins, "Introduction to High Energy Physics", Addison-Wesley (1986) section 8.3.

[10] M. Kobayashi and K. Maskawa, Progresses in Theoretical Physics 49 (1973) 652.

[11] R.N. Cahn and G. Goldhaber, "The Experimental Foundations of Particle Physics", Cambridge University Press (1989) chapter 8.

[12] G. Altarelli et al., "Z physics at LEP I, Volume 2: Higgs search and new physics", CERN 89-08 185.

[13] C. Itzykson and J-B. Zuber, "Quantum field Theory", McGraw-Hill (1985) section 4.1.4.

[14] J. Collins "Renormalization", Cambridge University Press (1984) section 2.2.

[15] Z. Wąs, "Radiative Corrections", CERN 94-04 (1994) 307.

[16] B.H. Bransden and C.J. Joachain, "Introduction to Quantum Mechanics", Longman (1989) section 12.2.

[17] F. Halzen and A.D. Martin, "Quarks and Leptons: An Introductory Course in Modern Particle Physics", Wiley (1984) section 6.1.

[18] M.A. Samuel et al., Physical Review Letters 67 (1991) 668.

[19] M. Banner et al., Physics Letters B 126 (1983) 398.

[20] P. Bagnaia et al., Physics Letters B 129 (1983) 130.

[21] The ALEPH Collaboration, "The ALEPH Handbook", ALEPH 89-77.

[22] D. Decamp et al., Nucl. Instr. and Meth. A 294 (1990) 121.

[23] D. Buskulic et al., Nucl. Instr. and Meth. A 360 (1995) 481.

[24] G. Batignani et al., IEEE Trans. Nucl. Sci. NS-39(4/5) (1992) Vol. 1, p. 438.

[25] G.J. Barber et al., Nucl. Instr. and Meth. A 279 (1989) 212.

[26] W.B. Atwood et al., Nucl. Instr. and Meth. A 306 (1991) 446.

[27] D. Bédérède et al., SICAL: a high precision silicon-tungsten luminosity calorimeter for ALEPH, to be published in Nucl. Instr. and Meth. A.

[28] R. Brun et al., CERN-DD/EE/84-1 (1987).

[29] W.J. Stirling, Physics Letters B 271 (1991) 261.

[30] M. Bohm, A. Denner and W. Hollik, Nuclear Physics B 304 (1988) 687.

[31] F.A. Berends, R. Kleiss and W. Hollik, Nuclear Physics B 304 (1988) 712.

[32] G. Altarelli et al., "Z physics at LEP I, Volume 3: Event generators and software", CERN 89-08 section 3.3.2.

[33] S. Jadach, B.F.L. Ward and Z. Was, Computer Physics Communications 79 (1994) 503.

[34] G. Altarelli et al., "Z physics at LEP I, Volume 3: Event generators and software", CERN 89-08, section 3.2.3.

[35] S. Jadach et al., Computer Physics Communications 70 (1992) 69.

[36] T. Sjostrand, "The LUND Monte Carlo for jet fragmentation and e^+e^- physics", LU-TP-85-10 (1985).

[37] D. Buskulic et al., Physics Letters B 313 (1993) 509.

[38] M. Drees and R. Godbole, Nuclear Physics B 339 (1990) 355.

[39] D. Buskulic et al., Zeitschrift für Physik C 62 (1994) 539.

[40] D.J. Summers and A.P. Betteridge, unpublished work (1992).

[41] L. Lyons, "Statistics for nuclear and particle physicists", Cambridge University Press (1986) section 6.2.

[42] P. De Causmaecker et al., Nuclear Physics B 206 (1982) 53.

[43] P. De Causmaecker et al., Nuclear Physics B 206 (1982) 61.

[44] M. Aguilar-Benitaz et al., Physical Review D 50 (1992) 1173.

[45] J.A. Grifols and A. Méndez, Physics Letters B 255 (1991) 611.

[46] L. West, "Search for non-minimal standard model decays of the Z boson", Ph.D. thesis (1991) Appendix A.

[47] F. Halzen and A.D. Martin, "Quarks and Leptons: An Introductory Course in Modern Particle Physics", Wiley (1984) section 6.5.

[48] M.L. Perl et al., Physical Review Letters 35 (1975) 1489.

[49] M. Aguilar-Benitaz et al., Physical Review D 50 (1992) 1396-1403.

[50] D.J. Silverman and G.L. Shaw, Physics Review D 27(1983) 1196.

[51] F.A. Berends and R. Kleiss, Nuclear Physics B 186 (1981) 22.

[52] D. Buskulic et al., Zeitschrift für Physik C 59 (1993) 369.

[53] D. Decamp et al., Physics Reports 216 (1992) 253.

[54] O. Helene, Nucl. Instr. and Meth. 212 (1983) 319.

[55] L. Lyons, "Statistics for nuclear and particle physicists", Cambridge University Press (1986) section 6.5.

[56] G. Domokos et al. Physics Review D 32 (1985) 247.

[57] R. Escribano and E. Massó, UAB-FT-317 (1993).

[58] J.D. Bjorken and S.D. Drell, "Relativistic Quantum Mechanics", McGraw-Hill Book Company (1964) section 7.2.